A masters dissertation submitted in partial fulfilment of the degree of
Master of Science in Engineering

The Effects of Chemical Composition, Solidification Rate, and Homogenization on the Intermetallic Particle Microstructure of AA8XXX Aluminum Alloys for Battery Foil Applications

---

Prepared by:

Maluleka P. Tshepo

Supervisor: Dr. Sarah L. George

Centre for Materials Engineering

Department of Mechanical Engineering

February 2025

Acknowledgements

I am deeply grateful to the individuals and organizations listed below for their invaluable contributions throughout my pursuit of a master's degree. Their diverse roles have significantly enriched my academic journey:

- My supervisor, Dr. Sarah L. George, for her guidance, encouragement, and dedication to this work.
- Dr. Gerard Leteba for his contribution and guidance in my experimental setup in the Lab.
- James Dicks for further guidance on how to approach some parts of the lab work.
- Penny Louw and Soraya Von Willingh for the lab induction and assistance with operating the lab equipment.
- Rachel Cupido from the Chemical Engineering Department for performing the powder XRD on my specimen..
- Miranda Waldron and Nasheeta Hanief from the Electron Microscope Unit (EMU) at UCT, for the help and training they offered me on how to use the SEM.
- Maxwell Vos for assistance with SEM-EDX analysis of partially dissolved sample.
- The support from fellow CME students.
- The staff at the Department of Mechanical Engineering workshop for sample sectioning.
- Hulamin Rolled Products Pietermaritzburg, for supplying the samples and providing financial support.
- UCT financial aid for further financial support.

Abstract

The growing demand for high-performance lithium-ion batteries, driven by the electric vehicle (EV) market, necessitates the development of current collectors that offer both superior electrical conductivity and enhanced mechanical properties. AA1XXX series aluminum alloys, commonly used in battery applications, are limited by their strength and ductility. As an alternative, AA8XXX aluminum alloys, particularly those based on the Al-Fe-Si system, show promise due to their improved strength. However, their intermetallic particle (IMP) microstructure needs to be understood for optimal performance.

This research investigates the impact of chemical composition, cooling rate, and homogenization processes on the IMP microstructure of AA8021 and AA8079 alloys, which are potential candidate alloys for this application. Using 2D and 3D analytical approaches supported by analytical tools including light microscopy (LM), scanning electron microscopy (SEM), scanning transmission electron microscopy (STEM) and X-ray diffraction (XRD).

The study identified three primary morphologies: plate-shaped, feathery/skeletal, and needle-shaped, corresponding to Al_3Fe, Al_mFe, and Al_6Fe phases. The results reveal that higher Fe content in AA8021 leads to a higher volume fraction of finer IMPs, while higher Si content in AA8079 enhances the stability of Al_3Fe and reduces the presence of Al_mFe. Furthermore, cooling rate significantly influences IMP morphology and phase stability, with higher cooling rates favoring the formation of finer, metastable phases at the surface. Homogenization treatments induce phase transformations from metastable Al_6Fe and Al_mFe to the stable Al_3Fe phase, improving the uniformity and distribution of IMPs.

Plagiarism Declaration

I know the meaning of plagiarism and declare that all the work in the document, save for that which is properly acknowledged, is my own. This thesis/dissertation has been submitted to the Turnitin module (or equivalent similarity and originality checking software) and I confirm that my supervisor has seen my report and any concerns revealed by such have been resolved with my supervisor.

Signed by candidate

Signature

Date

List of Abbreviations

- AA8XXX - 8 thousand series Aluminium Alloy
- Al - Alumminium
- AC - As Cast
- C - Carbon
- Cu - Copper
- EDS - Energy Dispersive X-ray Spectroscopy
- EM - Electron Microscope
- EV - Electric Vehicle
- Fe - Iron
- FFP - Fast Fourier Processing
- HAADF - High-Angle Annular Dark-Field
- HRTEM - High-Resolution Transmission Electron Microscopy
- HT1 - Homogenization Treatment at 500°C for 2 hours
- HT2 - Homogenization Treatment at 500°C for 20 hours
- HT3 - Homogenization Treatment at 550°C
- HT4 - Homogenization Treatment at 560°C
- HT5 - Homogenization Treatment at 580°C
- IMP - Intermetallic Particle
- Mn - Manganesse
- Mg - Magnesium
- LM - Light Microscope
- SEM - Scanning Electron Microscope
- Si - Silicon
- STEM - Scanning Transmission Electron Microscope
- Ti - Titanium
- wt% - Weight percent
- XRD - X-Ray Diffraction

List of Figures

List of Tables

Contents

1.Introduction

1.1 Background to and motivation for investigation.

The demand for high-performance lithium-ion (Li-ion) batteries has surged with the increasing popularity of electric vehicles (EVs), which require lighter batteries capable of delivering higher energy and power densities. Current collectors, a critical component of Li-ion batteries, play a vital role in ensuring efficient charge and discharge cycles . Traditionally, AA1XXX series aluminum alloys have been used as current collectors in these batteries due to their superior electrical conductivity, stemming from their high purity. However, these alloys do not possess enough strength and ductility, which are essential properties for improving battery performance and ensuring structural integrity during operation [1], [2].

As electric vehicle technology evolves, there is a growing need for materials that not only maintain excellent electrical conductivity but also offer enhanced mechanical properties, including strength and ductility. In this context, AA8XXX aluminum alloys, which are based on the Al-Fe-Si system and characterized by higher levels of iron (Fe) and silicon (Si), are being considered as a promising alternative [3]. These alloys are known for their improved strength compared to AA1XXX alloys, but their microstructural characteristics, particularly the intermetallic particles (IMPs), must be carefully understood to ensure their suitability as current collectors in high-density battery applications.

The microstructure of AA8XXX alloys is significantly influenced by several factors, including the chemical composition, solidification rate, and homogenization process. Specifically, the volume fraction, size, distribution, and morphology of the intermetallic particles present in the alloy directly affect its mechanical and electrical properties [4]. Therefore, the aim of this work is to use DC-cast ingot slices of AA8021 and AA8079, two alloys with varying Fe and Si contents as a vehicle to interrogate the effects of composition and cooling rate on the intermetallic particle (IMP) structures. Beyond this a number of homogenisation practices will be imposed on the alloys and on samples extracted from different locations of the ingot, representing cooling rates at the surface and at the centre of the ingot. The evolution of the IMPS during these homogenisation heat treatments will allow for understanding the complex phase changes and morphological evolutions that occur, and their link to composition and initial solidification rates.

Understanding the significant interactions is crucial for optimizing the material's performance in battery applications. By studying these factors in detail, the ultimate goal is to gather knowledge so that these insights can then drive proposals for implementation for further strength testing to fine-tune the AA8XXX foil protocols to achieve a balance between high strength and electrical conductivity, making them suitable as current collectors for next-generation high-energy and high-power density batteries.

1.2 Objectives of Report

The objectives of this study are therefore to:

- Use 2D and 3D analytical approaches to interrogate IMP microstructures in the As-Cast (AC) samples of AA8021 and AA8079 extracted from two key locations of DC-cast ingot slices, namely, the surface (representing fast cooling) and the centre (representing slower cooling). This will facilitate investigations into:
  - the role of varying chemical composition in the form or Fe and Si concentrations and ratios.
  - the role of solidification rate on phase formation.
- Impose a series of homogenisation protocols on the alloys and locations to mimic industry-scale homogenisation protocols within a target parameter range and interrogate the evolution of the IMP microstructures. This will facilitate investigations into:
  - the effect of temperature and time variability in homogenisation protocols.
  - the role of composition on IMP evolution during homogenisation.
  - the role of solidification rate on IMP evolution during homogenisation.
- Identify composition and homogenisation combinations that allow for the most suitable IMP development to suit the requirements for current collectors in the EV batteries.

1.3 Limitations and Scope of Investigation

The aim of this study is to investigate the influence/effect of elemental composition, cooling rate (DC casting) and homogenisation on the IMP microstructure in AA8021 and AA8079 aluminium alloys. The aforementioned factors determine the IMP microstructure, that is the size, type, morphology, volume fraction and distribution of the IMPs. This microchemistry, in turn affects the strength, electrical conductivity and formability of these alloys, of which are of paramount importance for current collectors in the EV batteries.

While the IMP microstructure clearly influences key physical and mechanical properties, this study focuses on the qualitative and quantitative analysis of the IMP microstructure using various analytical techniques, such as microscopy, X-ray diffraction (XRD), and image analysis tools like ImageJ.

Furthermore, research suggests that Al-Fe-based IMPs often share similar chemical compositions, and crystallographic data is rarely available when needed. Many of these IMPs have not been extensively studied, making it difficult to distinguish them accurately based on their chemical or crystallographic information. This lack of distinction can lead to errors in analysis. For instance, some peaks in the XRD spectra may not correspond to any documented phases in the free crystallography open database, and peak broadening may occur, complicating phase identification and preventing the use of the Rietveld method for phase quantification.

1.4 Plan of Development

This report begins with a literature review, which summarizes past research findings related to the Al-Fe-Si alloy system and the AA8XXX aluminum alloys. It then outlines the experimental procedures conducted to achieve the objectives of the study. The observations and results obtained from these experiments are presented in the results section, followed by a comprehensive discussion of these results. The report concludes with conclusions based on the findings. Finally, the recommendations for future research are made based on the conclusions, challenges and limitations encountered during the research.

2.Literature Review

2.1 Aluminium

Aluminium is the most abundant metallic element in the Earth's crust, constituting approximately 8.00-8.30wt.% [5],[6]. It is primarily found in bauxite ore, a product of millions of years of limestone and silica weathering. Due to its high affinity for oxygen, aluminium naturally occurs in various forms of hydrated aluminium oxide (Al_2O_3) or alumina compounds, with compositions determined by geological and locational factors [5]. This variation in composition is represented by Formula (2.1):

$$Al_2O_3 \cdot xH_2O \tag{2.1}$$

Main impurities commonly found in bauxite ore alongside alumina minerals include iron oxides and silica [5]. Aluminium extraction from bauxite ore occurs in two main phases: (i) the Bayer process for alumina extraction and (ii) the Hall-Héroult process for reducing alumina to pure aluminium [5]-[7]. The production steps of pure aluminium from bauxite ore are illustrated in Figure 2.2. The Bayer process comprises two primary steps, depicted in Figure 2.1. In the first step of the Bayer process, bauxite is dissolved in concentrated sodium hydroxide NaOH under pressure (1-6 atm) and at temperatures ranging from $150 - 240°C$, yielding sodium aluminate ($NaAlO_2$) and water (H_2O) according to Equation (2.2): [5],[6]:

$$Al_2O_3 \cdot xH_2O + 2\,NaOH \rightarrow 2\,NaAlO_2 + (x + 1)\,H_2O \tag{2.2}$$

The subsequent and final step of the Bayer process involves the breakdown of sodium aluminate into hydrated alumina by manipulating the reaction conditions to induce the reverse reaction, as depicted in the following Equation (2.3):

$$2\,NaAlO_2 + H_2O \rightarrow 2\,NaOH + Al_2O_3 \cdot 3\,H_2O \tag{2.3}$$

The trihydrate compound ($Al_2O_3 \cdot 3\,H_2O$) undergoes calcination in rotary kilns or fluidized beds. This process, carried out within a temperature range of 400°C and 600°C, serves to eliminate a significant portion of the water content, resulting in the formation of the chemically reactive γ of alumina. Further heating to 1200°C produces the chemically stable α-form of alumina. The alumina produced through this method typically exhibits a purity ranging from 99.3% to 99.7%[5].

Following the Bayer process, the subsequent stage, known as the Hall-Héroult process, utilizes electrolytic reduction to convert aluminum oxide to aluminum, as described by Equation (2.4). This energy-intensive process occurs in smelting plants and is the most energy-intensive step in aluminum production, requiring substantial quantities of electricity [5],[6]. However, the purity of the resulting aluminium is never 100%, therefore, some impurities such as iron(Fe) and silicon(Si) are commonly found in commercially pure aluminium.

$$Al_2O_3 + 3\,C \rightarrow 4\,Al + 3\,CO_2 \tag{2.4}$$

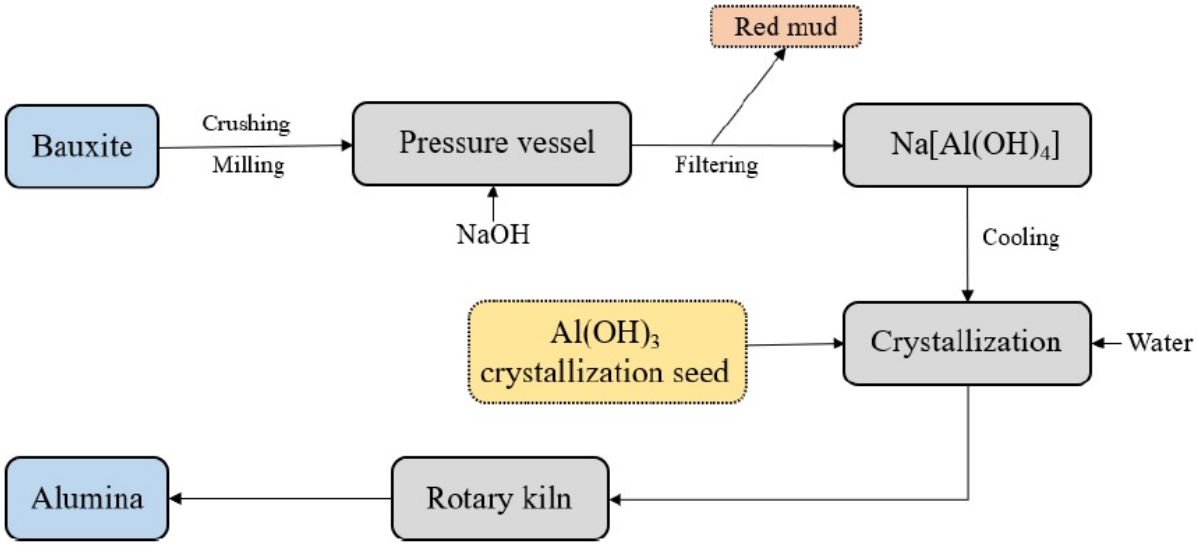

Figure 2.1: The Bayer process for alumina extraction [8].

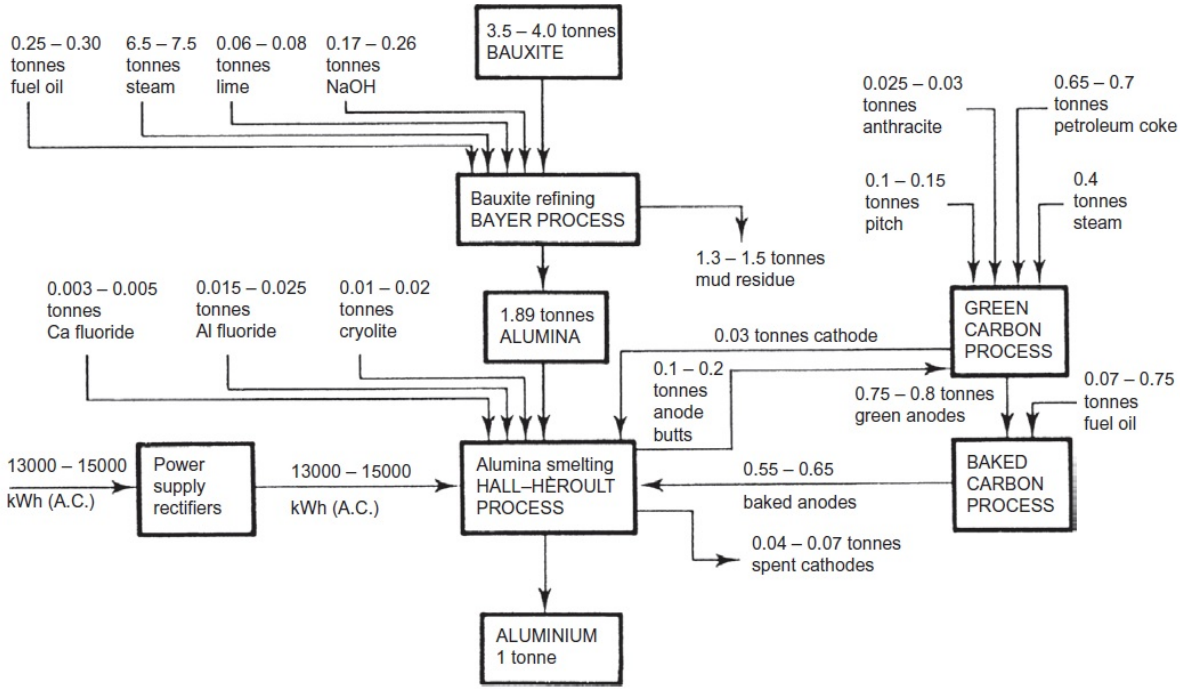

Figure 2.2: Alumina extraction and smelting through Bayer and Hall-Héroult processes [5].

Despite the lengthy and energy-intensive process involved in extracting aluminum from its ore, it remains the second most widely used structural metal after iron [5]. This is attributed to its favorable combination of mechanical and physical properties, as outlined in Table 2.1. Aluminum's competitiveness as a structural metal stems from its low relative density of 2.7 g/cm^3, which results in high specific modulus and specific tensile strength values comparable to those of magnesium (Mg), Fe and titanium (Ti). Consequently, for an equivalent mass of metal, aluminum is likely to perform equally well or even better than the metals listed.

Table 2.1: Physical and mechanical properties of pure common metals [9],[10].

Property	Unit	Al	Mg	Ti	Fe	Cu
Crystal structure	-	fcc	fcc	cph	bcc	cph
Density (d)	g/cm^3	2.70	1.74	4.51	7.87	8.96
Tensile strength (σ)	MPa	90	175	520	262	200
Specific strength (σ/d)	-	33.33	100.57	115.30	33.29	22.32
Elastic modulus (E)	GPa	70	45	120	211	130
Specific modulus (E/d)	-	26	26	26	27	14
Electrical resistivity @20°C	$\mu\Omega$cm	2.67	4.2	54	10.1	1.69

Another notable characteristic of pure aluminum from Table 2.1 is its low specific electrical resistivity compared to copper, a widely used metal for electrical applications. Similarly, for an equivalent mass, pure aluminum exhibits superior electrical conductivity compared to copper.

2.2 Aluminium alloys.

Table 2.1, clearly illustrates that pure aluminum exhibits relatively weak mechanical properties, with approximate values for tensile strength and elastic modulus at 90 megapascals (MPa) and 70 gigapascals (GPa), respectively. Consequently, aluminum is frequently alloyed to enhance its properties for applications where the inherent properties of pure aluminum are inadequate [11],[12].This necessity has led to the development of a diverse range of aluminum alloys.

2.2.1 Classification of aluminium alloys.

Aluminum alloys are classified and distinguished in various ways. One fundamental classification is based on primary production methods, namely cast and wrought alloys. Cast aluminum alloys are produced by melting and pouring molten metal into a mold to achieve a near-net shape. On the other hand, wrought alloys are initially cast into an ingot or billet and subsequently deformed into the desired final product forms such as foils, sheets, wires, rods, etc [13].

The Aluminium Association uses a four-digit designation system (AAXXXX) known as the International Alloy Designation System (IADS) to categorize various wrought aluminum alloys into different series or groups based on their principal alloying elements [11]-[14]. This classification is summarized in Table 2.2, where 'AA' in AAXXX stands for 'Aluminum Alloys' and the first digit Xxxx specifies the primary alloying element. The second digit xXxx indicates any modifications made to the parent alloy. Finally, the last two digits in the designation xxXX are numbers assigned to differentiate between alloys within the same series or group [13].

Table 2.2: Classification of wrought aluminium alloys based on principal alloying elements [14].

Alloy group	Principal alloying element
AA1xxx	Unalloyed
AA2xxx	Copper (Cu)
AA3xxx	Manganese (Mn)
AA4xxx	Silicon (Si)
AA5xxx	Magnesium (Mg)
AA6xxx	Magnesium (Mg) and Silicon (Si)
AA7xxx	Zinc (Zn)
AA8xxx	Other elements

A further distinction is made on the basis of the primary strengthening method. Alloys that respond to thermal treatments such as solution treatment, quenching, and precipitation/age hardening, are categorized as heat treatable aluminum alloys. Conversely, those that do not respond to thermal treatment are classified as non-heat treatable aluminum alloys. The latter group achieves strengthening through work hardening [12].

Table 2.3: Classification of wrought aluminium alloys based on primary strengthening mechanism [12].

Aluminium series	Alloy system
Non heat-treatable (work-hardenable)	
AA1xxx	Pure Aluminium
AA3xxx	Al-Mn
AA4xxx	Al-Si
AA5xxx	Al-Mg
AA8xxx	Al-Fe
AA8xxx	Al-Fe-Ni
Heat-treatable (precipitation-hardenable)	
AA2xxx	Al-Cu
AA2xxx	Al-Cu-Mg
AA2xxx	Al-Cu-Li
AA6xxx	Al-Mg-Si
AA7xxx	Al-Zn
AA7xxx	Al-Zn-Mg
AA7xxx	Al-Zn-Mg-Cu
AA8xxx	Al-Li-Cu-Mg

2.2.2 AA8021 and AA8079

Unlike other series of aluminum alloys, the 8xxx series comprises a wide range of chemical composition systems with different primary alloying elements. Each system is specifically designed to achieve an optimal combination of properties for particular applications. For instance, alloys based on the Al−Fe−Ce and Al−Fe−V−Si systems are preferred for application(s) that require elevated temperature performance [12]. Alloys within the Al−Li−Cu−Mg system are desirable in aerospace applications due to their exceptional strength-to-weight ratio, often replacing some medium- to high-strength AA2xxx and AA7xxx alloys [12],[15]. Furthermore, alloys based on Al−Fe−Si exhibit microstructural stability and possess mechanical properties suitable for use as electrical conductors.

The alloys in the AA8xxx series, based on the Al-Fe-Si system, incorporate higher levels of Fe and Si compared to the permissible range in Al-Fe-Si based AA1xxx series alloys. Additionally, AA8xxx alloys are typically non-heat-treatable, thus relying on the work-hardening mechanism for primary strengthening. Common alloys within this system include AA8021 and AA8079, with Fe and Si as the main/principal alloying elements in their matrices [16],[17]. Manganese (Mn) is sometimes also considered a primary alloying element in this system; however, its significance hinges on the quantity present in the alloy. Delijic et al. [18] reported a typical range of 0.25-1.75 wt% for Fe, 0.05-0.65 wt% for Si and 0.01-0.5 wt% for Mn. These reported ranges for Fe, Si, and Mn in Al-Fe-Si alloys are consistent with the values outlined in the European Standard EN 573-3 [19], providing additional validation for their composition

specifications.

These ranges of permissible amounts of Fe and Si in both alloys indicate potential variability in the Fe and Si content within these alloys. Consequently, various elemental compositions have been reported for these alloys in different studies. Tables 2.4 and 2.5 illustrate the elemental composition of AA8021 [20] and AA8079 [21]. It is clear from the tables that the two alloys exhibit distinctions in their Fe and Si quantities. AA8079 demonstrates a significantly higher Si content than AA8021, whereas AA8021 exhibits a relatively higher Fe content than AA8079. The Fe:Si ratio has been adopted to investigate and explain the impact of Fe and Si levels on the microstructure and mechanical properties of aluminium alloys.

Table 2.4: Chemical composition of AA8021 aluminum alloy [20].

Alloy	Fe	Si	Cu	Mn	Ti	Al
AA8021	1.40	0.15	0.02	0.01	0.02	Bal

Table 2.5: Chemical composition of AA8079 aluminum alloy.[21].

Alloy	Fe	Si	Cu	Zn	Other
AA8079	1.3	0.3	0.005	0.1	0.15

2.3 Formation and effects of intermetallic particles (IMPs) in Al–Fe–Si system

While Fe and Si are deliberately added as significant alloying elements in 8xxx aluminum alloys, they exhibit limited solubility in aluminium, estimated at about ∼0.05% at 650°C for Fe and ∼1.65% at 577°C for Si. Consequently, excess Fe and Si, unable to dissolve fully in the aluminum matrix upon solidification, combine with other alloying elements to form binary Al-Fe and ternary Al-Fe-Si IMP phases [22],[23]. This indicates that most of Fe and Si in solidified aluminium alloys exist in the form of IMPs. These IMPs exhibit varying features such as morphology, size, aspect ratio, chemical composition, and hardness/brittleness, collectively constituting the microstructure and significantly influencing the mechanical properties of the alloys [24]. Therefore, it is essential to thoroughly understand the formation and evolution of these phases to potentially prevent the formation or mitigate the effects of harmful IMPs on mechanical properties.

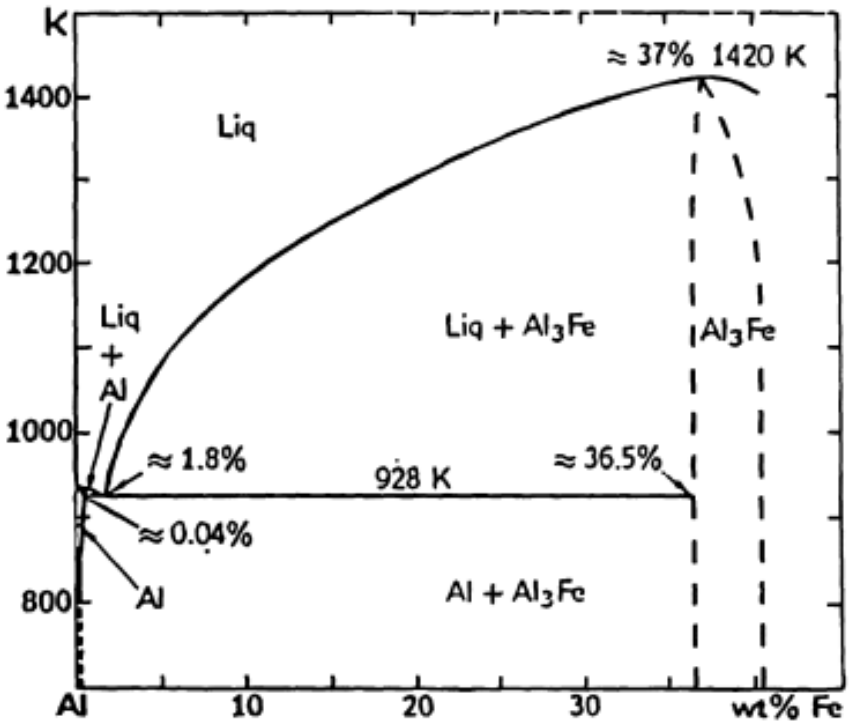

Figure 2.3: Al-rich corner of the binary Al-Fe phase diagram.[23].

Figure 2.3 shows the Al-rich corner of the binary Al-Fe diagram and illustrates the equilibrium IMPs that are stable at different temperatures for varying Fe compositions (wt%). In the absence of Si, the primary $Al_{13}Fe_4$, sometimes denoted as Al_3Fe, forms as the temperature of the molten metal decreases, as described by Equation (2.6) [23]. It has been reported that the primary $Al_{13}Fe_4$ particles that form prior to the eutectic temperature tend to grow larger compared to those that form at the eutectic temperature [25],[26]. Additionally, metastable

phases such as Al_6Fe may also form, typically under non-equilibrium conditions discussed in sub-subsection 2.5.1.1 [25].

In studies focused on the aluminium-rich corner of the Al-Fe-Si ternary system, researchers have identified more than 10 different types of IMPs when significant Si content is present [27],[26],[28]. Some of these IMPs have been argued to be difficult to identify and characterize using conventional techniques due to their closely similar chemical compositions. Figure 2.4a illustrates the Al-rich corner of the system with 0.8 wt% Fe and depicts the stable equilibrium phases at various temperatures and Si wt% contents. It shows the expected equilibrium IMPs for 0.8 wt% Fe content [29], corresponding to the Fe content typical of 8xxx aluminum alloys. The chemical compositions of these IMPs exhibit significant variability, as summarized in Figure 2.4b.The most common stable phases are identified as cubic Al_8Fe_2Si (denoted as $\alpha-$AlFeSi), monoclinic Al_5FeSi ($\beta-$AlFeSi), and monoclinic $Al_{13}Fe_4$ ($\theta-$AlFe), each with widely accepted chemical compositions [23].

The formation of Al-Fe-Si IMP phases during solidification is significantly influenced by the alloy composition (Fe:Si ratio) and solidification conditions. The reactions responsible for the formation of these IMP phases, as depicted in the Al-Fe-Si phase diagram shown in 2.4a, are described by Equations(2.5)-(2.11) [27]:

$$\mathrm{L} \rightarrow \mathrm{Al}-\text{dendrite} \tag{2.5}$$

$$\mathrm{L} \rightarrow \mathrm{Al} + \mathrm{Al_3Fe} \tag{2.6}$$

$$\mathrm{A} + \mathrm{Al_3Fe} \rightarrow \mathrm{Al_3Fe} + \alpha-\mathrm{AlFeSi} \tag{2.7}$$

$$\mathrm{L} \rightarrow \mathrm{Al} + \alpha-\mathrm{AlFeSi} \tag{2.8}$$

$$\mathrm{L} + \alpha-\mathrm{AlFeSi} \rightarrow \mathrm{Al} + \mathrm{Al} + \beta-\mathrm{AlFeSi} \tag{2.9}$$

$$\mathrm{L} \rightarrow \mathrm{Al} + \beta-\mathrm{AlFeSi} \tag{2.10}$$

$$\mathrm{L} \rightarrow \mathrm{Al} + \beta-\mathrm{AlFeSi} + \mathrm{Si} \tag{2.11}$$

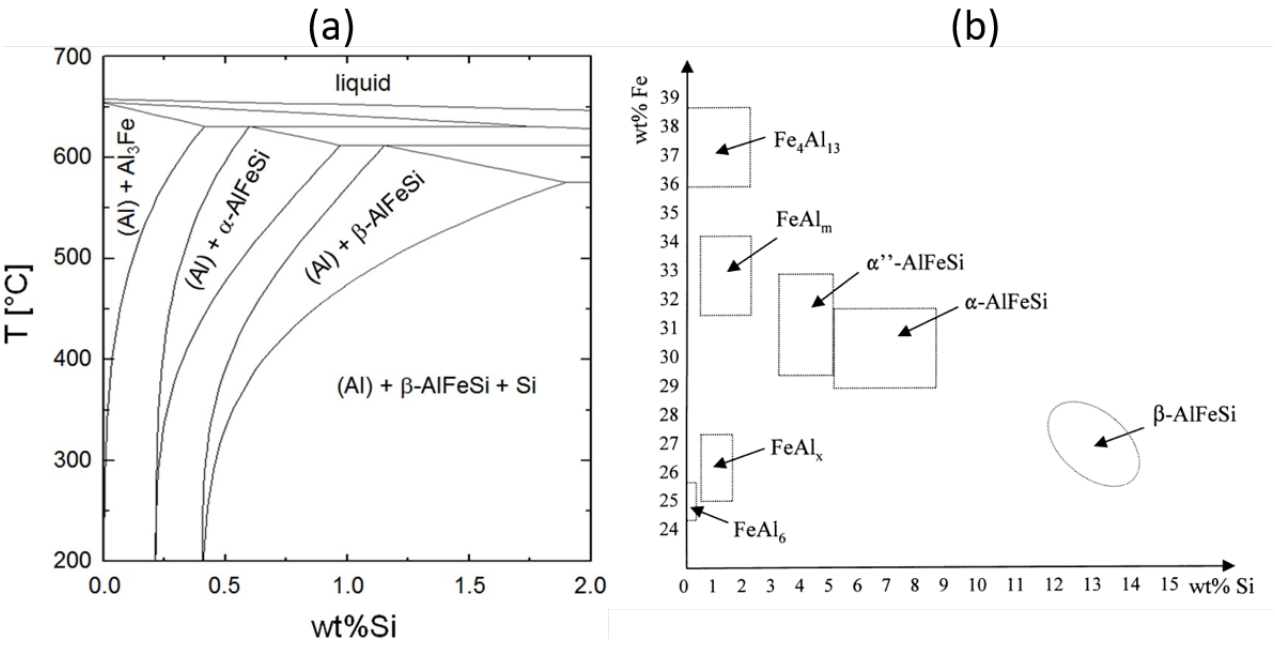

Figure 2.4: (a)Al-rich corner of the ternary Al-Fe-Si phase diagram with 0.5 wt% Fe [29] and (b) IMP phases and their corresponding Fe and Si compositions[23].

When the Si content in the alloy exceeds 0.5% and the Fe-to-Si ratio is 3:1, hexagonal α–AlFeSi is produced. Conversely, with a 2:1 ratio of Fe:Si, monoclinic β–AlFeSi is formed. When Si is less than 0.5%, θ-AlFe is formed [28]. Among these phases, β–AlFeSi and θ-AlFe are considered the most detrimental in the Al-Fe-Si system due to their platelet and needle-like morphologies, which serve as initiation sites for cracking in the alloy. This leads to reduced formability, ductility, and strength[30],[31]. On the other hand, α–AlFeSi is considered the hardest of these phases, making it more brittle during the aluminum foil deformation process [17]. However, its script-like and sometimes circular morphology minimizes its deleterious effects on mechanical properties, making it the preferred phase between the two. It is important to note that under varying conditions, these phases may adopt different crystal structures and morphologies [23]. Thus, the aforementioned argument addresses the most common scenarios under equilibrium conditions.

2.4 Effects of Alloying elements on the IMP microstructure and properties

The versatility of aluminum in numerous applications stems from its ability to be alloyed with various elements, resulting in a wide range of desirable property combinations. This versatility is primarily attributed to the diverse influences these alloying elements have on the microstructure of the resulting aluminum alloys. In particular, 8xxx aluminum alloys exhibit enhanced properties such as corrosion resistance, formability, ductility, tensile strength, and electrical conductivity. The following discussion will elucidate the purpose and influence of alloying elements on the microstructure of 8xxx aluminum alloys.

2.4.1 Iron (Fe)

Fe is the prediminant impurity found in aluminum. Its high solubility in molten aluminium allows easy dissolution at every molten stage throughout the production process [7]. Consequently, aluminum alloys, including pure aluminum metals, inherently contain a certain percentage of Fe. When intentionally added to the alloy, Fe serves to refine the grains and stabilize strength at elevated temperatures, particularly in aluminum alloys used for electrical conductors [7]. However, an increase in the amount of Fe in aluminium alloys results in an increase in the average size, thickness, and volume fraction of Fe-containing IMPs [32]. This effect is illustrated in Figure 2.5 which clearly demonstrates the increase in density (area/volume fraction) and size of shiny Fe-containing IMPs as the Fe content increases from (a) to (c).

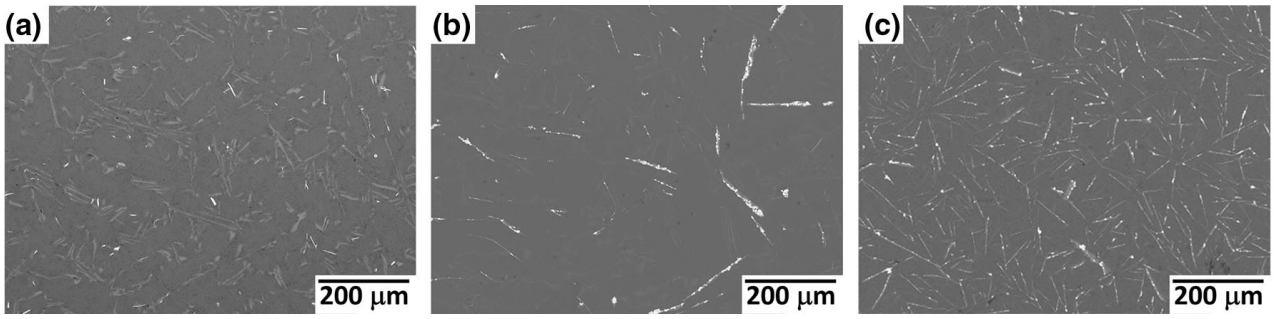

Figure 2.5: SEM micrographs of (a)Al-7wt%Si (b)Al-7wt%Si-0.6wt%Fe (c)Al-7wt%Si-1wt%Fe alloys [32].

2.4.2 Silicon (Si)

Si is another common impurity in commercial aluminum alloys after Fe. Like Fe, Si is often intentionally added to achieve the formation of Mg_2Si and to mitigate the adverse effects of Al-Fe IMPs by promoting the formation of α-AlFeSi ternary phases [7]. Shakiba et al. [22] reported an observed increase in the proportion of α-AlFeSi with higher silicon content in the alloy. Moreover, the transition from both β-AlFeSi and θ-AlFe (Al_3Fe) to α-AlFeSi is promoted when there is a substantial amount of silicon present[22].

2.4.3 Magnesium (Mg)

Mg reacts with Si to create the hardening Mg_2Si dispersoid phase that contributes to the strengthening of aluminum alloys [33]. Typically, this phase forms during the homogenization heat treatment process. At elevated homogenization temperatures, nucleation of α-Al(Fe,Mn)Si particles occurs on pre-precipitated Mg_2Si, leading to the dissolution of the Mg_2Si phase [34]. This indicates that α-Al(Fe,Mn)Si typically forms at the expense of Mg_2Si.

2.4.4 Manganese (Mn)

Mn exhibits a relatively high solid solubility of approximately 1.25 wt% in aluminum, which is higher compared to Fe and Si [35]. As a result, upon solidification, most of the Mn remains in solid solution, while some combines with other alloying elements to form IMPs. The Mn retained in solution is directly associated with the decrease in the electrical conductivity of aluminum alloys [36]. In the Al-Fe-Si system, metastable IMPs such as Al_6Mn have been reported to form at the expense of Al_3Fe during non-equilibrium solidification. Additionally, Mn is used to modify the shape of acicular or plate-shaped Fe constituents and to reduce their embrittling effect[37].

2.4.5 Copper (Cu)

Cu can chemically react with Al and Fe, forming either tetragonal Al_7Cu_2Fe or orthorhombic *alpha*-(Al,Cu,Fe) particles during the solidification process. These particles remain insoluble in subsequent heat treatments but can undergo transformation from one form to another during ingot thermal treatments [7].

2.4.6 Titanium (Ti)

Commercially pure aluminum usually contains titanium in the range of 10 to 100 ppm. Ti has a detrimental effect on the electrical conductivity of aluminum. However, the addition of boron to the melt can help reduce its concentration by forming insoluble TiB_2. Titanium is primarily used as a grain refiner in the production of aluminum alloy castings and ingots [7]

2.5 Aluminium alloy foil

In electric vehicles (EVs), batteries function as the primary power source for vehicle propulsion. These batteries rely on various electrochemical reactions, such as those in Li-ion and lead-acid batteries, to convert stored chemical energy into electrical energy [1]. What distinguishes EV batteries apart from each other is their superior attributes, which include power density, energy density, safety, and cost [2]. Aluminum foil is recognized for its chemical stability, formability, strength and energy density, making it a suitable choice for applications in EV batteries.

2.5.1 Processing steps for manufacturing industrial aluminium foil

Commercial purity aluminum and several alloys from the ternary Al-Fe-Si system, such as AA8021 and AA8079, have long been used as foil stock [38],[39]. The growing popularity and demand for foils based on the AA8xxx series can be attributed to their exceptional combination of mechanical strength, formability, electrical conductivity, and thermal conductivity [40]. Figure 2.6 shows the steps involved in the fabrication process of aluminum alloy foils. This production cycle typically begins with either direct chill (DC) or twin-roll casting (TRC), followed by meticulously controlled thermomechanical processing of the ingot leading to the final foil product. These processes have a significant impact on the IMP microstructure and alloy properties. Therefore, precise control over processing parameters and methods is essential to ensure that the desired IMP microstructure and properties are achieved.

Before the homogenization process, the ingot is scalped to remove any surface defects and impurities leftover from the casting process. Next, the ingot is homogenized and hot-rolled into a strip with a thickness of about 2 to 5 mm thick. This strip then goes through cold rolling to achieve an intermediate gauge (known as foilstock) ranging from 0.4 to 1 mm. Afterward, it undergoes annealing typically at temperatures between 350°C and 400°C. Following annealing, the material is cold rolled again to reach the final desired foil thickness. For producing thinner foil gauges below approximately 100 μm, closed-gap rolling is utilized, typically performed in a specialized foil mill. Most aluminum foil products are used in the O-temper, requiring a soft annealing process. Furthermore, the final gauge annealing process is crucial not only to facilitate recrystallization but also to remove any residues of rolling lubricants from the foil [29].

The type, size, shape, distribution and volume fraction of IMP microstructures found in aluminum alloys are affected by the alloy's chemical composition and the cooling/solidification rate during casting [42]. The influence of the latter is elaborated in Subsubsection 2.5.1.1. Homogenization, as detailed in subsubsection 2.5.1.2, is a process applied to aluminum alloys to eliminate chemical segregation and improve the uniformity of the alloy's microstructure.

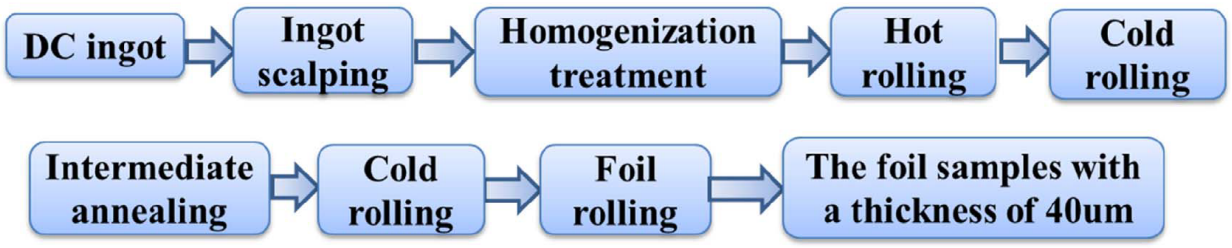

Figure 2.6: Manufacturing process of aluminium foil [41].

2.5.1.1 Direct-Chill (DC) Casting and its influence on the as-cast intermetallic microstructure

Direct-chill (DC) casting technology was introduced for commercial use in the 1930s. It is a conventional semi-continuous casting technology adopted for the production of non-ferrous ingots and billets, which serve as feedstock for secondary production processes such as rolling, extrusion, and drawing [11],[43]. Its operational principle is presented by Figure 2.5.1.1, which shows the molten metal fed into a bottomless water-cooled casting mold. Initially, with the starter block raised, the mold is closed, and molten metal is poured to the desired level. The cooling effect of the water-cooled mold walls causes the outer surface to solidify, forming a shell. This cooling process is termed primary cooling.
After this is achieved, the starter block is gradually lowered at a desired rate to a desired length while the molten metal is fed into the solidified shell, which now acts as a mold. As the starter block is lowered, cooling water impinges on the solidified aluminum shell, allowing the ingot to cool further. This process, known as secondary cooling, is responsible for major heat extraction in DC casting [43].

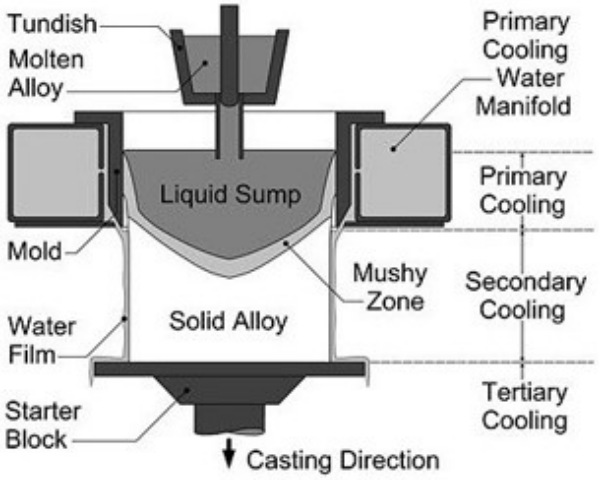

Figure 2.7: Vertical DC casting components and cooling regions [43].

Because of the longer thermal diffusion paths from the outer surface to the center, the solidification rate in the DC cast ingot varies across the width and thickness. This variation is reported to be between <0.1-20 Ks^{-1} [4]. Figure 2.8 illustrates that the cooling rate is higher at the surface where the undercooling is greater due to colder mold walls and lower at the center of the ingot. This variation influences the resulting IMP microstructure, including phase/type, size, morphology, distribution, and volume fraction, and consequently affects the mechanical properties [4],[44].

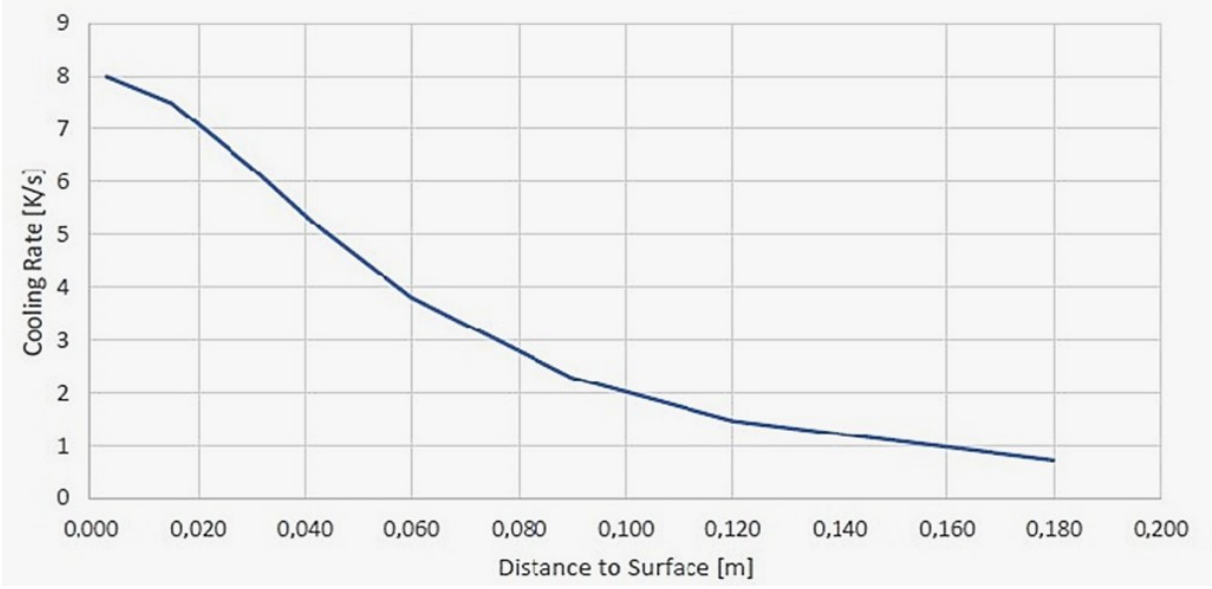

Figure 2.8: Cooling rate as a function of distance to surface[45].

The first notable effect of non-equilibrium solidification rate in DC casting, is the observed deviation from the expected equilibrium IMPs which would typically form upon equilibrium solidification. Higher cooling rates promote the formation of Fe-depleted metastable phases such as Al_6Fe, Al_mFe, alongside stable Si-rich α-AlFeSi and α''-AlFeSi thereby displacing the dominance of $Al_{13}Fe_4$, which prevails under slower cooling conditions[4]. This phenomenon has been clarified by Miki et al. who thoroughly documented the correlation between cooling rates and the resulting phases within the AA1xxx aluminum alloy [46]. This relationship is depicted in Equations (2.12)-(2.14).

$$< 1\,\mathrm{K/sec} : \mathrm{Al_3Fe} \tag{2.12}$$

$$1 - /10\,\mathrm{K/sec} : \mathrm{Al_6Fe} \tag{2.13}$$

$$> 10\,\mathrm{K/sec} : \mathrm{Al_mFe} \tag{2.14}$$

Dutta and Rettenmayr reported that this observation is partly attributed to the decline of the Fe:Si ratio in the liquid as the cooling rate rises, caused by a reduction in Fe concentration and a simultaneous increase in Si concentration with higher cooling rates, as illustrated by the plot in Figure 2.9[4].

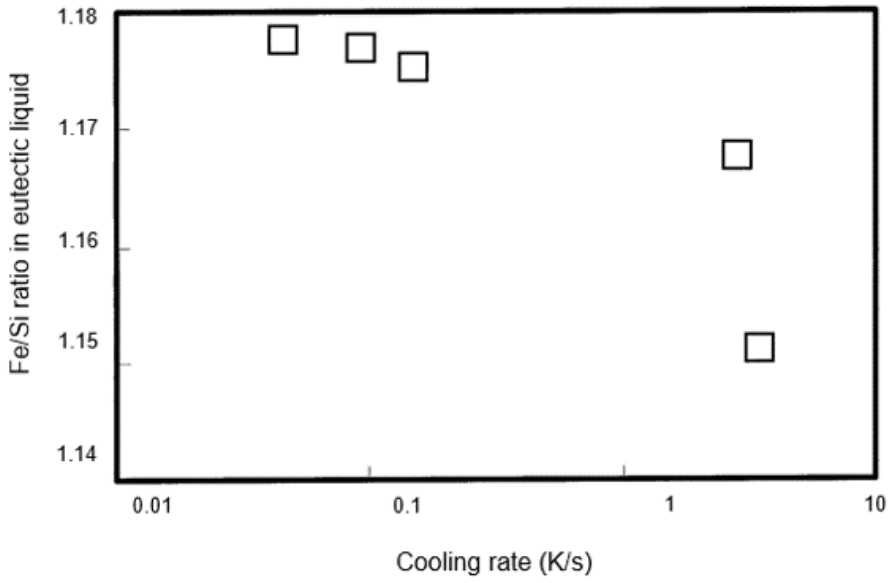

Figure 2.9: Fe:Si ratio as function of cooling rate during solidification of Al-0.8Fe-0.8Si [4]

Further investigation has been conducted to examine the influence of cooling rate on the volume fraction of IMPs in Al-Fe-Si alloys. Kraft et al. [47] developed a numerical model to forecast both the intermetallic particle fraction and the dendrite arm spacing (DAS) in such alloys. Their model predicts that higher cooling rates result in a higher proportion of IMPs and a decrease in DAS. A recent review by Dutta and Rettenmayr [4] also corroborated these findings, with experimental data closely aligned with the predictions of the aforementioned model as shown in Figures 2.10a and b. The variability observed in the volume fraction can be attributed to the limited time available for the homogenizing effects of coarsening and back diffusion at elevated cooling rates [4],[48].

In addition, studies have revealed a negative correlation between intermetallic particle size and cooling rate. Enhanced cooling rates have been observed to facilitate the refinement of IMP size, concurrently altering their morphology towards a more equiaxed or regular shape by reducing the aspect ratio[4],[47],[48]. This relationship is visually shown in Figure 2.10c and through high-magnification micrographs in Figure 2.11. The observed refinement of IMPs is attributed to the process of repeated nucleation, suggesting that in these alloys, the evolution of second phases is predominantly nucleation-dependent rather than growth-dependent.

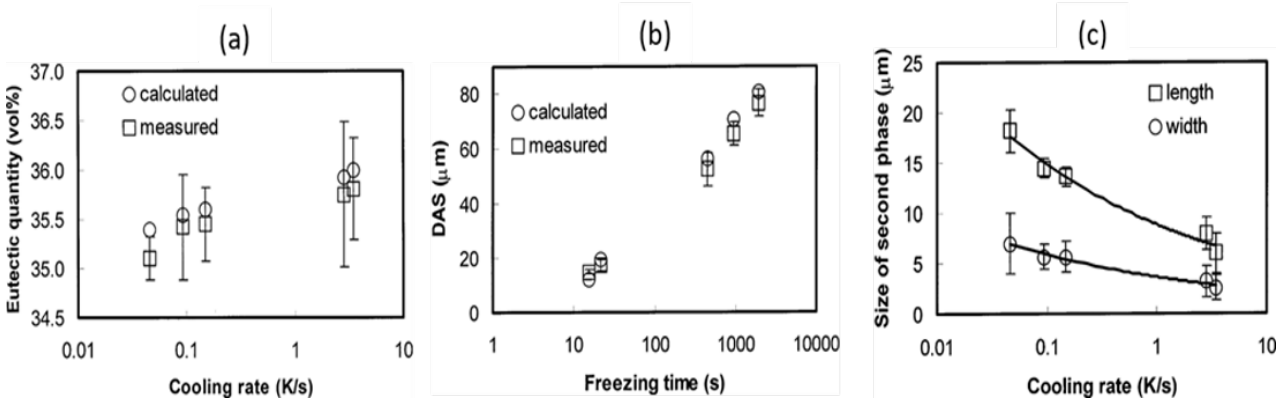

Figure 2.10: (a)Variation in the volume fraction of intermetallic particles as a function of cooling rate(b) Variation in the secondary DAS as a function as a function of cooling rate (c) Variation in the size of the intermetallic particles as function of cooling rate [4].

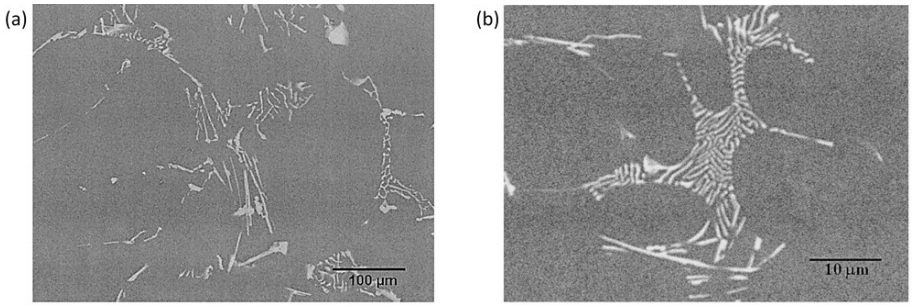

Figure 2.11: micrographs showing intermetallic particles in samples with different cooing rates (a) 0.09 Ks^{-1} and (b) 3.43 Ks^{-1} [4].

The examination of various regions within the DC cast ingot reveals distinct IMP microstructures, and is summarized as follows:

- The edge of the DC cast ingot experiences rapid cooling, resulting in a higher volume fraction of IMP particles that are finer, faceted and depleted in Fe such as metastable Al_6Fe, Al_mFe and stable Si-rich α-AlFeSi.
- In contrast, the center of the ingot undergoes slower cooling, leading to the formation of a lower volume fraction and coarser, Fe-rich IMPs such as $Al_{13}Fe_4$ and β-AlFeSi. These IMPs tend to have more faceted morphology.These IMPs often exhibit a more faceted morphology.

2.5.1.2 The influence of homogenization on the intermetallic microstructure AA8xxx

Homogenization is a crucial heat treatment process that is traditionally performed on wrought aluminum alloys prior to the fabrication of semi-finished products like foils, sheets, and plates. This essential high-temperature treatment serves multiple objectives, including[5]:

- reduce the effects of microsegreagtion.
- remove non-equilibrium or unwanted IMPs particles with low melting points which are typically responsible for crack initiation in the downstream fabrication.
- facilitate controlled precipitation of surplus alloying elements dissolved in the matrix.

After solidification, the matrix is usually supersaturated as a result of rapid cooling during the casting process. Elevated temperatures during homogenization induce the diffusion of alloying elements from regions such as grain boundaries and solute-rich areas towards the center of the grains [5],[49].The diffusion time is impacted by factors such as diffusion distances, grain size or dendrite arm spacing (DAS), and individual diffusion rates of alloying elements. In this context, the average distance x that a specific atom can cover in time (t) is determined by the formula $x=(Dt)^{(1/2)}$, where D represents the diffusion coefficient and it is highly sensitive to temperature. These coefficients vary significantly for different elements, often by several orders of magnitude [5]. Consequently, the efficacy of homogenization treatment is influenced by temperature, duration, and specific alloying element(s) involved in the diffusion process.

In AA8XXX aluminum alloys, characterized by fine and elongated Al_xFe and $Al_xFe_ySi_z$ IMPs, homogenization is conducted to redistribute and spheroidize the IMPs through particle transformation, typically performed at temperatures above 500°C [49]. This procedure is essential to improve the downstream fabrication processes and mechanical properties of aluminum alloys [50]. Furthermore, diffusion of alloying elements during homogenization changes the solute solution content, directly influencing the electrical resistivity/conductivity of the alloys.

Numerous studies have investigated the impact of homogenization practices on the microstructure of IMPs within the Al-Fe-Si system. Patel and Mukhopadhay [51] reviewed the homogenization effect on AA8011 and noted that the alloy containing β-AlFeSi phase in

the as-cast condition undergoes transformation to α-AlFeSi phase from approximately 570°C. Consequently, the morphology changes from needle-like to circular. This latter observation is in agreement with the results of a similar study on AA8079 by Králík et al. [49] which shows the spheroidization, coarsening and change in distribution of IMPs during homogenization (Figure 2.12). In as-cast state, the elongated IMPs begin to spheroidize at 450°C. Continued spheroidization and nucleation of new particles is observed at 475°C. This is followed by the dissolution and coarsening of selected IMPs at 550°C and below 575°C. Above 575°C, the final microstructure is coarser.

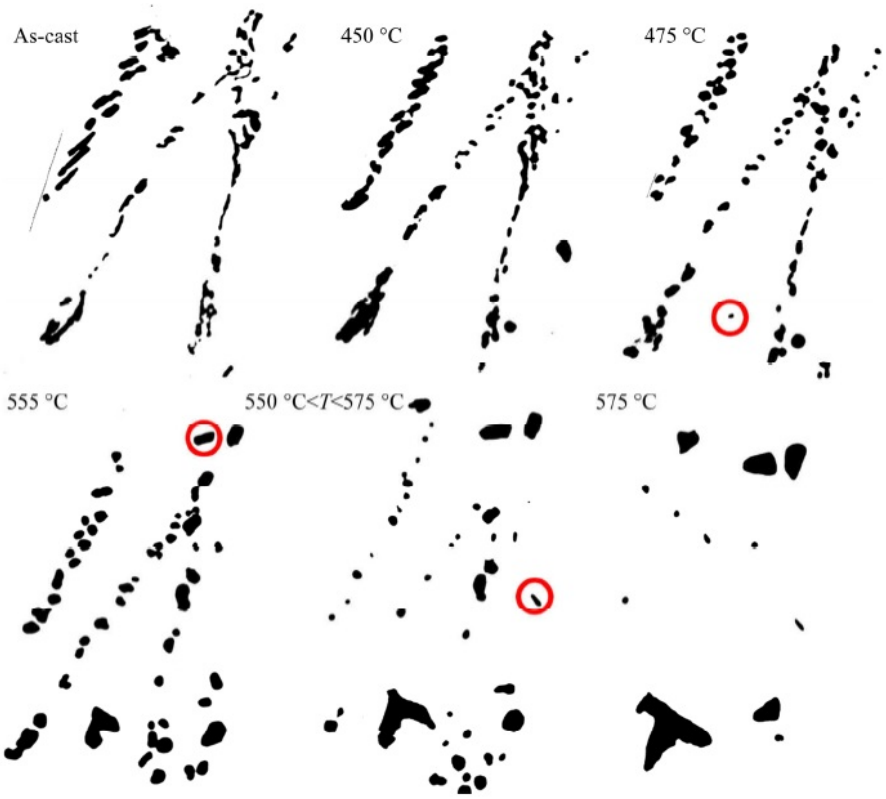

Figure 2.12: Schematic representation of the IMP shape and size evolution during homogenization [49].

The graph in Figure 2.13 shows that the variation in homogenization soak time and temperature also affects the IMP volume fraction. The proportion of IMP decreases as time and/or temperature increases [51].

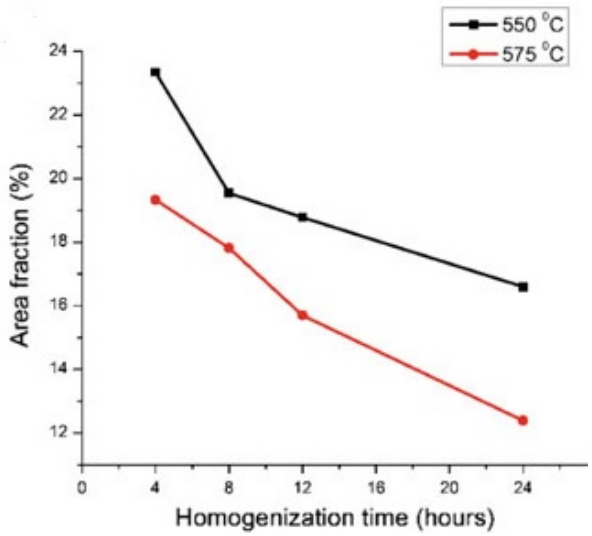

Figure 2.13: The effect of homogenization time on IMP volume fraction conducted at two different temperatures [51].

In the case of alloys initially containing metastable Al_6Fe, Al_mFe and stable α-AlFeSi, homogenization at approximately 550°C, initiates distinct phase transformations. The metastable Fe-depleted Al_6Fe and Al_mFe phases undergo transformation into stable Al_3Fe or Al_13Fe_4 through the dissolution–reprecipitation mechanism where Fe is required to diffuse from the dissolving Al_mFe to the precipitating Al_3Fe particles [22]. Consequently, Fe is identified as the primary alloying element driving this transformation. The same mechanism is responsible for the transformation of α-AlFeSi to Al_3Fe or Al_13Fe_4 at temperatures approximately 590°C and/or above [22].

2.5.2 Aluminium alloy based current collectors in EV batteries

In electric vehicles, lithium-ion (Li-ion) batteries serve as the primary power source for propulsion, owing to their high energy and power densities [1] which affects the performance of the battery. The internal structure of a typical Li-ion battery comprises a cathode, an anode, a separator, an electrolyte, and two current collectors as shown in Figure 2.14a. Current collectors serve as connecting components that collect electrical current produced at the electrodes and establish connections with external circuits. In commercial applications, Al and Cu foils are commonly used as current collectors for cathodes and anodes, respectively. Together, Al and Cu current collectors contribute a total of 15% which breaks down to 6.9wt% and 8.1wt% respectively towards the battery's total weight (Figure 2.14b).

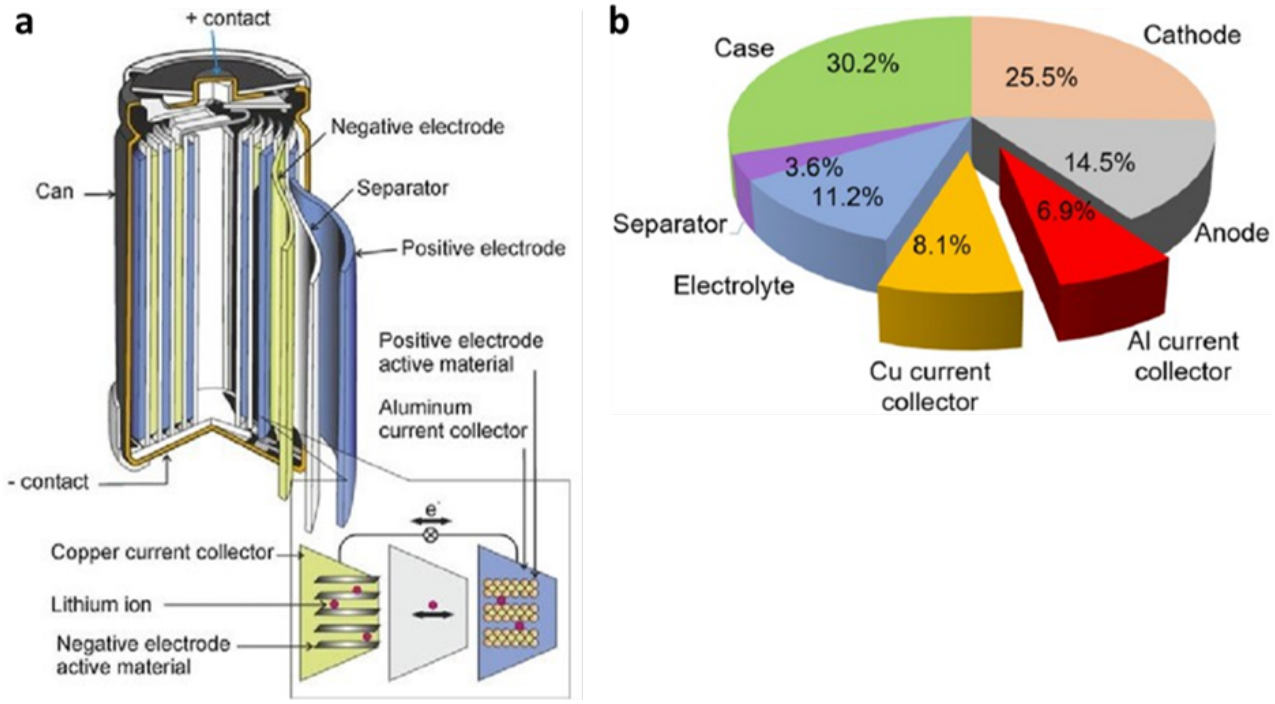

Figure 2.14: (a) The internal structure of a Lithium-ion (Li-ion) battery [52] and (b) The weight percentage (wt%) contribution of each component in the Li-ion battery [1].

The performance of Li-ion batteries is significantly influenced by a combination of current collector properties such as electrochemical stability, electrical conductivity, mechanical strength, and density. Enhancement of these properties improves the capacity, rate capability, and long-term stability or service life of Li-ion batteries. Furthermore, the reduction in thickness (wt% contribution) of the aluminium foil has been reported to drastically improve the energy density of the Li-ion battery. All of these factors work together towards enhanced Li-ion battery performance. In essence, these properties constitute the requirements for materials that can be used in Li-ion batteries as current collectors.
Therefore, since the introduction of aluminium foil in commercial Li-ion batteries in 1991, significant research has been aimed toward the development of the structure of the current collectors.

However, aluminiun foil offers an excellent combination of these properties. Its exceptional electrochemical stability is attributed to the formation of the passivation films (i.e Al_2O_3 and AlF_3) on its surface. This surface layer is responsible for the protection from undesired reactions with the electrolytes and only allows Al to serve as current collectors at the cathode of Li-ion batteries, because an attempt to use aluminium at the anode results with the alloying reaction between aluminium and lithium.

In addition to the remarkable electrochemical stability, aluminum foil current collectors offer the advantage of high electrical conductivity. Aluminum ranks as the fourth most conductive metal, exhibiting an electrical resistivity of $2.65 \times_{108}^{-} \mu\Omega$ at 20°C. This position it just after silver, copper, and gold in terms of conductivity.

The good mechanical strength combined with the low density recorded in Table 2.1 also makes aluminium foils stand out from other candidate materials because common electrodes are created through the process of casting slurry onto metal foil current collectors [26]. As a result, current collectors play a crucial role as a support mechanism for the electrodes. Some electrodes undergo substantial volume changes during cycling (charging and discharging), such as thick electrodes like the Si anode experiencing up to 400% volume expansion due to formation of LiSi alloy [27], the risk of electrode pulverization or delamination is significant. Thus, using current collectors with sufficient mechanical strength becomes imperative to maintain the cohesion of electrode active materials to the current collector and maintain overall electrode integrity during cycling.

2.6 Microstructural characterization

Microstructure characterization is a traditional approach to gain insight into microstructure in materials. This analysis enhances our understanding of the impacts of composition, manufacturing techniques, and heat treatments on the microstructure and subsequently the mechanical properties of alloys. Consequently, diverse techniques have been employed to thoroughly examine the microstructure of materials, encompassing both qualitative and quantitative analyses. The characterization techniques that are typically used to study IMPs include Light microscopy (LM), scanning electron microscopy (SEM), scanning transmission electron microscopy (STEM) and X-ray diffraction (XRD). In addition, supporting software tools are frequently utilized for the processing of data acquired from these techniques. Examples include ImageJ for image analysis and ATEX/Profex for diffractogram analysis.

2.6.1 Light Microscopy (LM)

Optical microscopy refers to the observation of structures that can be resolved through the use optical/light microscope [53] and utilizes light in the visible spectra to illuminate specimen [54]. It is essential to obtain a 2D overview of the microstructural features such as morphology, size, and distribution of intermetallic phases to the capability of that microscope and imaging requirements such as different magnifications, resolution, depth of field and lens aberrations. Additionally, built-in video cameras that are compatible with TV monitors are extensively used for easy display and recording of micrographs and videos [55].
This invaluable piece of equipment comes in different configurations to suit the needs of the investigation. Such as being upright or inverted, having a specific illumination system (reflected light microscope or transmission light microscope), using a specific light sources (i.e Tungsten-halogen filament lamps) and having a choice of examination mode (bright field, dark field and Oblique illumination) [55][56][54].

Reflected light microscopy is a commonly employed technique for imaging metallic microstructures, utilizing the Köhler illumination principle to achieve the desired uniform light field on the surface of the object. This principle involves the use of the collector lens to create an image of the light source at the first condenser lens or at the aperture of the illumination condenser, as shown in Figure 2.15. Subsequently, the second condenser lens reproduces this image of the light source in the back focal plane of the objective lens, following reflection of the light by the reflector. Consequently, the surface of the specimen receives uniform illumination. Condenser lenses, in conjunction with the objective lens, generate an image of the radiant field stop within the plane of the surface of the sample [55].

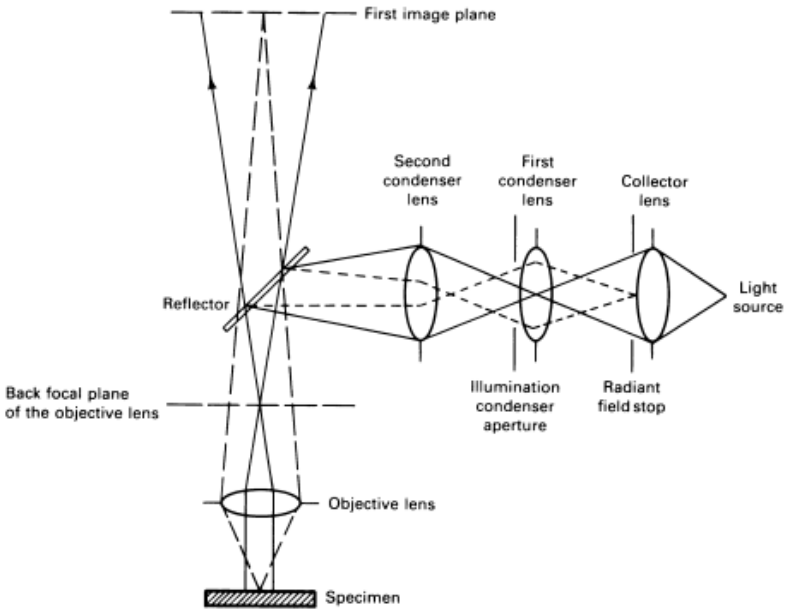

Figure 2.15: The Köhler illuminatoin principle schematic in reflected light microscope [55].

2.6.2 Scanning electron microscopy (SEM)

Electron microscope (EM) is also an invaluable tool in microstructural analysis, and the two should not substitute each other wholly but should be used in conjunction for enhanced evaluation. It uses a beam of electrons to illuminate and interact with not only the outer surface but penetrates the sample to a certain depth in Scanning Electron Microscope (SEM) and through the sample using Transmission Electron Microscope (TEM). This interaction allows for in-depth analysis of the microstructure as explained in the following subsubsections.

2.6.2.1 Scanning Electron Microscope (SEM) coupled with Energy Dispersive X-ray spectroscopy (EDX)

SEM is a highly versatile tool for examining the microstructure of metallic materials. In comparison to the optical microscope, it significantly improves resolution, reaching approximately 10 nm in routine instruments and dropping to below 3 nm in ultimate values—expanding magnification capabilities from 10,000× to 150,000×. It also boasts a larger depth of focus by over two orders of magnitude, ranging from 1 m at 10,000× to 2 mm at 10× [54]. SEM, with attached equipment for energy-dispersive x-ray analysis, enables semi-quantitative and, in favorable cases, quantitative composition analysis of the sample features [54],[57],[58]. These qualities are necessary when analysing components of the sample that cannot be clearly imaged, identified or distinguished in a typical OM due to its limited capabilities.

In SEM, the electron beam is generated from a heated cathode and directed through a series of magnetic lenses to focus the beam of a diameter ranging from approximately 10 nm (100 Å) in standard instruments to 1 nm (10 Å) in high-resolution instruments. Acceleration voltages vary from 1000 to 50,000 V, and the current of primary electrons responsible for for

magnification falls within the range of $10^{-}8$ to $10^{-}7$ A [54].

The electron beam scans the specimen creating an interaction volume shown in Figure 2.16 and the electrons excited by the beam are emitted from the specimen and collected in an electron detector [59]. Backscattered electrons exit the surface with a diverse range of energies. Some of the factors affecting this energy distribution are the number of outer-shell electrons, the material's atomic number, and the specimen's surface inclination. When the atomic number of the impacted material decreases, fewer electrons are backscattered, and more energy is lost. Conversely, in materials with higher atomic numbers, numerous electrons are backscattered by surface-close atoms, resulting in minimal energy loss. Thus, materials with higher atomic numbers shines brighter compared to materials with lower atomic numbers [54],[59]. This is valuable for differentiating IMPs of different phases.

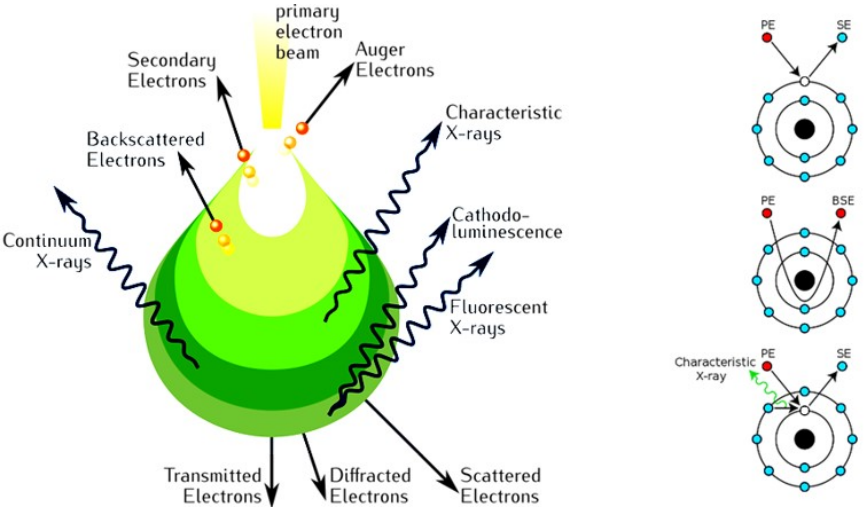

Figure 2.16: The interaction volume created by a beam of electron interacting with a sample [60].

The X-rays excited by the electron beam form two types of spectra: (1) the bremsstrahlung with a continuous spectrum and (2) the characteristic radiation with a distinct line spectrum which can be analyzed by energy-dispersive spectrometry (EDS) to yield information about the chemistry of the material [54],[57],[58], [59]. This can be used to attain information about the chemical composition of IMPs and other components in metallic materials.

2.6.2.2 Transmission Electron Microscopy (TEM)

Transmission Electron Microscope (TEM), which involves passing electrons through the sample, provides visual information on the size, distribution, morphology and selected area electron diffraction (SAED). Furthermore, high resolution TEM (HRTEM) provides resolution at the sub-nm level and offers information not only on the size and morphology, but also on the crystallinity of specimens via atomic spacing measurements, coupled with the electron diffraction pattern and fast Fourier transforms (FFTs). Scanning TEM (STEM) is usually combined with energy-dispersive X-ray spectroscopy (EDS) in high angle annular dark field (HAADF)

to produce chemical x-ray and composite maps to quantify the elemental distributions within the specimens[58]. Both HAADF-STEM and STEM-EDS can used to elucidate the structures of the IMPs extracted from the Al substrates.

2.6.3 X-Ray Diffraction (XRD)

X-ray diffraction (XRD) is a non-destructive analytical technique whose principle hinges on the generation of characteristic diffraction patterns of a crystalline substance produced when x-rays interacts with the samples under investigation. X-rays are electromagnetic radiation whose wavelengths lie between 0.1Å and 100Å, similar to the interatomic distances in a crystal. This similarity allows crystal structures to diffract X-rays. XRD is used to assess the crystalline nature and phases of both bulk and extracted IMPs.

XRD is initiated by directing x-rays towards the sample through a slit of an ideal size and upon interaction with the sample, they are either scattered or transmitted by the electrons of the atoms in the specimen. It is important to note that these atoms lie in lattice planes with particular arrangement in a unit cell, see Figure 2.17. When the scattered x-rays interact constructively, a resulting x-ray displays a larger amplitude and a peak intensity is registered. This phenomena happens when the Bragg's law requirements for constructive interference are met according to equation 2.15:

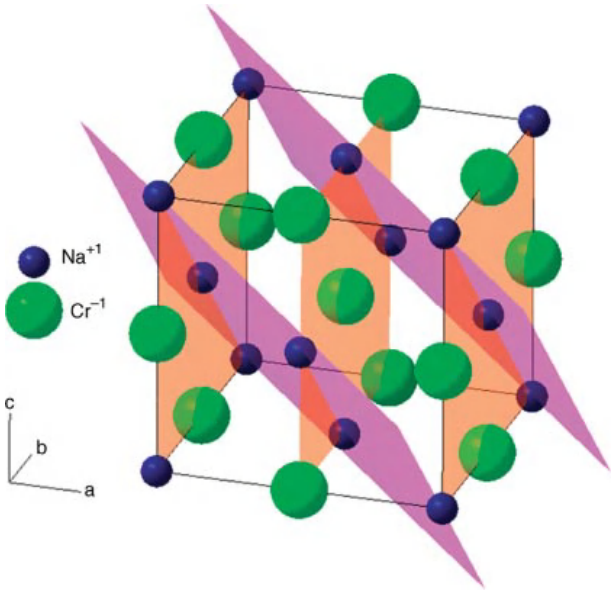

Figure 2.17: Arrangements of atoms in a unit cell with lattice planes

$$n\lambda = 2d_{hkl}\sin\theta \tag{2.15}$$

where :

n : Order of interference.

λ : x-ray wavelength.

d_{hkl} : distance between lattice planes h, k and l.

θ : angle of incident x-ray.

According to this relationship, constructive interference of x-rays scattered from adjacent planes happens when the path difference is an integer number of wavelengths. Figure 2.18 shows the geometric representation of this phenomena. The detector records the radiation diffracted at lattice planes that satisfy Bragg's law. Therefore, for a specific wavelength λ, the angle (peak position) θ or 2θ at which constructive interference occurs is measured and represented as a pattern which is unique for a substance and can therefore be seen as a fingerprint of a crystalline substance, allowing for crystallographic phase analysis. Additionally, the intensity of the peaks facilitates the determination of the quantitative composition of the phases in the samples.

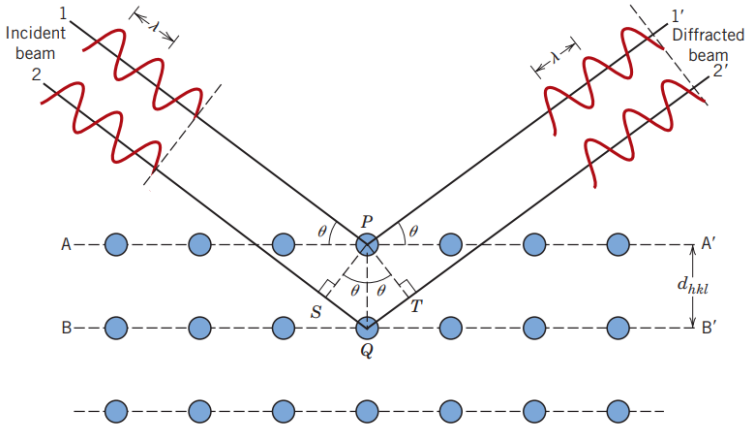

Figure 2.18: Diffraction of x-rays from planes of atoms in a crystal [61].

In a powder diffraction there are many possible orintations due to the polycrystalline nature of the sample. Thus, identical lattice planes in different crystals scatter x-rays in various directions, displaying a unique diffraction pattern for constituent phases present in the sample. This is then followed by peak identificationn in the diffraction pattern. This involves assigning the observed peaks to phases forming them. This is achieved by comparing the measured multiphase diffraction pattern with a database containing known phases, including expected ones like Al_mFe, Al_3Fe, Al_6Fe, Al_5FeSi and Al_8Fe_2Si.

Quantitative analysis involving determining the proportions of present phases is achieved through additional post-processing such as the Rietveld Refinement method which uses the least squares method to minimize the difference between the calculated and measured patterns as seen in equation 2.16. The index i represents the angular position in the powder pattern (refer to equation 2.17).

$$Min = \sum_{n=0}^{n-1} (W_i (Y_{obs,i} - Y_{calc_i})^2) \tag{2.16}$$

$$2\theta_i = 2\theta_{start} + i\Delta 2\theta \tag{2.17}$$

$where$:

$Y_{obs,i}$: observed intensity.

$Y_{calc,i}$: calculated intensity.

θ_{start} : starting angle.

$\Delta 2\theta$: angular step width

W_i : weight derived from the variance of $Y_{obs,i}$

3.Experimental Procedure

3.1 Summary of experimental techniques.

This chapter covers the two experimental approaches used to investigate the effect of varying solidification/cooling rates during DC casting, homogenization, and chemical compositions on the IMP microstructure in two aluminum alloys: AA8021 and AA8079. Before conducting laboratory experiments, the chemical compositions of as-cast samples were analyzed using inductively coupled plasma (ICP) spectroscopy. This data was then used to predict the expected IMP phases through thermodynamic calculations using JMatPro. The summary of these experimental approaches is shown in Figure 3.1.

In the first approach, as-cast and homogenized bulk samples extracted from both the surface and center of the ingot, were examined using traditional metallography techniques. These included SEM-EDS and light microscopy, combined with ImageJ for image analysis. The second approach focused on characterizing the extracted and partially extracted IMP particles (powder), produced through matrix dissolution and deep etching, respectively. The powder was analyzed using SEM-EDS, STEM, and XRD, with the Rietveld method employed to identify and quantify the IMP phase fractions.

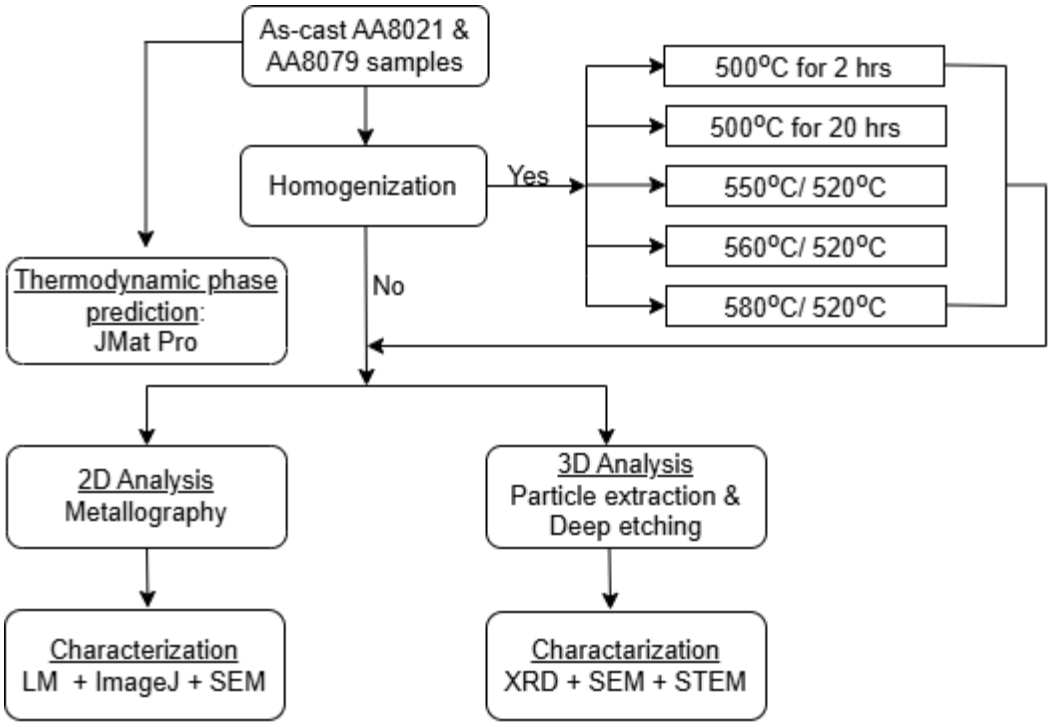

Figure 3.1: A summary of experiments carried out in this study

3.2 Material and sampling

In this research project, the materials investigated are AA8021 and AA8079 aluminium alloys, which were provided to the University of Cape Town's Centre for Materials Engineering (CME) by Hulamin rolled products in Pietermaritzburg. The chemical compositions of these alloys are provided in Table 3.1 below. There is a clear variation in Fe, Si and Ti wt% composition between these alloys. AA8079 contains relatively higher amount of Si compared to AA8021, which contains relative higher Fe than AA8079.

Table 3.1: Chemical compositions of AA8021 and AA8079 aluminium alloys.

Alloy	Si	Fe	Cu	Mn	Mg	Ti	Other	Aluminium
AA8021	0.034	1.147	≤ 0.01	≤ 0.01	≤ 0.005	0.015	≤ 0.038	matrix
AA8079	0.25	0.903	≤ 0.01	≤ 0.01	≤ 0.005	0.040	≤ 0.086	matrix

In Section 2.5.1.1, a discussion was provided explaining how the cooling rate of the ingot decreases gradually from its outer surface towards the centre during casting. This variation in cooling rates leads to microsegregation and differences in the IMP microstructure. To account for these effects on the IMP microstructure, the samples were collected from two distinct regions, as illustrated in Figure 3.2. These regions are termed surface (near surface) and center based on their locations within the DC cast ingot slice that was used as the source material for this work.

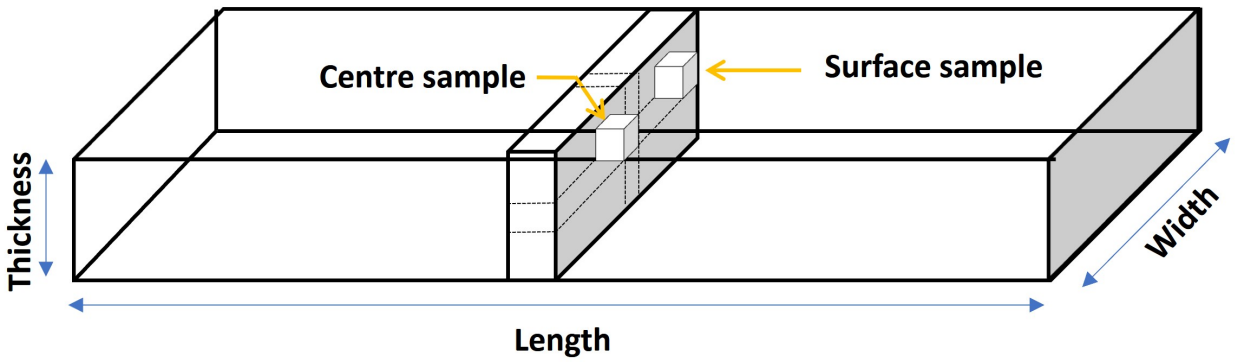

Figure 3.2: A schematic representation of the sampling regions along the ingot specimen.

3.3 Homogenization

In this study, two different homogenization practices were followed: one-step and two-step homogenization practices. The heating and cooling rates for both practices were maintained at 50°C/hr to ensure equilibrium temperature between the sample and the furnace. Overall, five distinct homogenization treatments were implemented, and a description of these practices is provided below in Table 3.2. The abbreviations listed in this table will be used consistently throughout this thesis to refer to the corresponding homogenization treatments.

Table 3.2: Abbreviations and descriptions of homogenization practices

Condition	Temperature 1	Time 1	Temperature 2	Time 2
AC (As Cast)	-	-	-	-
HT1	500°C	2 hours	-	-
HT2	500°C	20 hours	-	-
HT3	550°C	4 hours	520°C	2 hours
HT4	560°C	4 hours	520°C	2 hours
HT5	580°C	4 hours	520°C	2 hours

3.3.1 One-step homogenization

In a one-step homogenization treatment, graphically summarized in Figure 3.3, specimens were thermally treated in a programmable furnace following the steps outlined below. The heating and cooling rates were chosen to mimic industrial homogenization conditions, with the soaking time serving as the independent variable. The steps included:

i heating the specimens in a programmable furnace from room temperature (25°C) to 500°C at a heating rate of 50°C/hr.

ii soaking at this temperature for durations of either 2 or 20 hours.

iii Furnace cooling to room temperature at a cooling rate of 50°C/hr

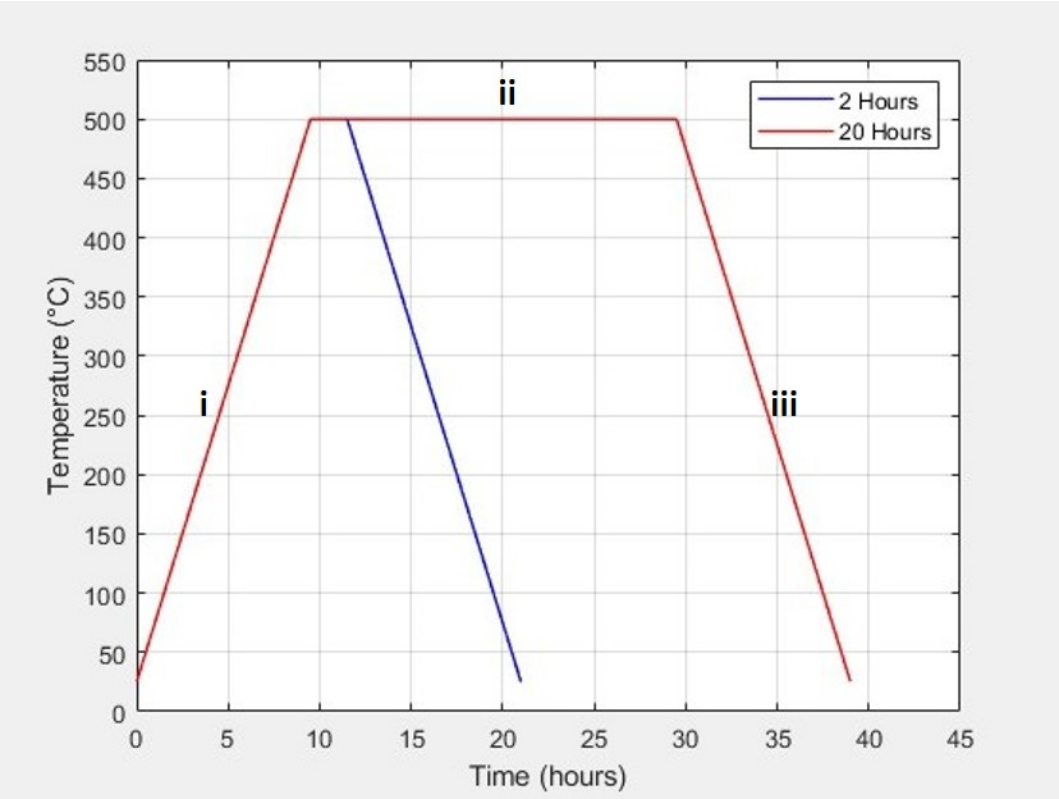

Figure 3.3: Single-step homogenization profiles at 500°C for 2 and 20 hours

3.3.2 Two-step homogenization

The two-step homogenization practice, as summarized graphically in Figure 3.4, involved the following steps:

i Heating the specimens in a programmable furnace at a constant rate of 50°C/hr from room temperature (25°C) to varying higher temperatures; (550°C, 560°C and 580°C).

ii Soaking the specimens at these higher temperatures for four hours.

iii cooling the furnace to 520°C at rate of 50°C/hr.

iv Soaking the specimens at 520°C for an additional two hours.

v Finally, cooling the specimens to room temperature at a rate of 50°C/hr to simulate industrial homogenization conditions.

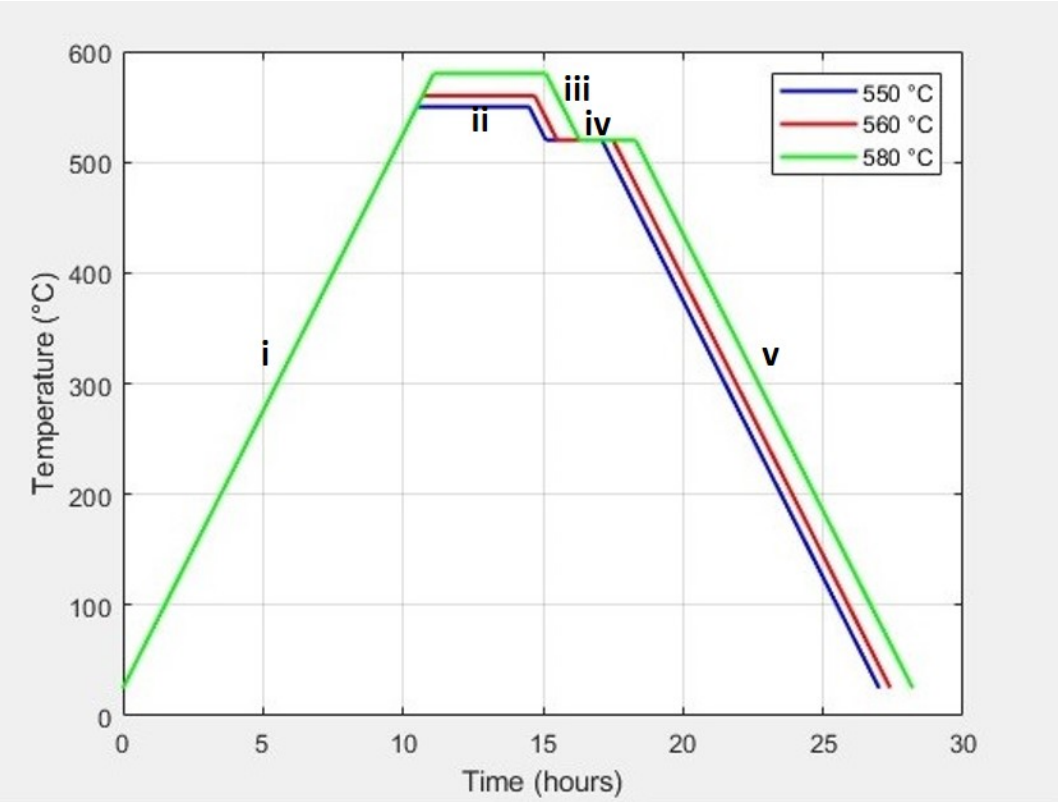

Figure 3.4: Two-step homogenization profiles with varying initial soaking temperatures at 550°C, 560°C and 580°C.

3.4 2D microstructural characterization

Microstructural observations and analysis of the bulk solid sample using various types of microscopes (LM and EM) necessitate thorough metallographic sample preparation, as outlined in the subsequent subsections.

3.4.1 Metallographic sample preparation.

The samples in both as-cast and homogenized conditions were hot-mounted in black polyfast resin using a Struers Labopress-3 hot mounting presser. A force of 25 kN was applied during heating and cooling phases, each lasting seven minutes. Subsequently, the samples underwent grinding and polishing steps outlined in Table 3.3, performed using a Struers Tegramina-25 apparatus. The speed mentioned in Table 3.3 refers to the speed of the specimen holder, as labeled in Figure 3.5. The turntable speed was maintained at 150 rpm in a counter-rotation mode relative to the specimen holder. The initial grinding step utilized 1200 grit size SiC paper, followed by steps 2-5 which comprised the entire polishing procedure. The OP-S polishing step was divided into two stages (steps 4 and 5) to complement each other. Although the use of MD-Chem cloth in the OP-S step successfully removed 1 μm scratches, some pick-up was observed on the sample surface. To address this, the OP-S procedure was repeated using MD-Nap cloth, effectively removing the pick-up with minimal scratching. Finally, step 6 was executed, which was aimed at rinsing off the OP-S residue from the surface.

Table 3.3: Metallographic grinding and polishing sample preparation methods.

Sic paper/Polishing pad	Suspension	Force (N)	Time(minutes)	Speed (rpm)
1. 1200 grit paper	water	20	1	150
2. MD Mol cloth	DiaDuo-2 3μm	20	7	150
3. MD Nap cloth	DiaDuo-2 1μm	15	3	150
4. MD chem cloth	OP-S	15	3	100
5. MD Nap cloth	OP-S	15	2	100
6. MD Nap cloth	water	5	2	100

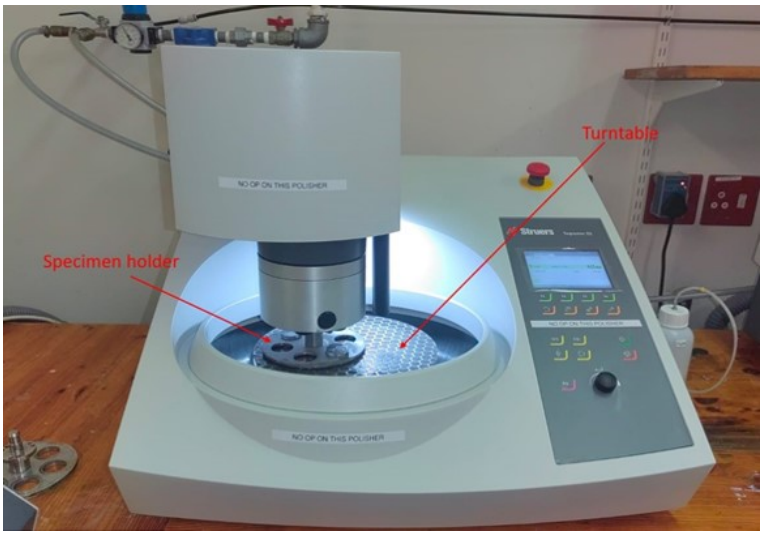

Figure 3.5: Struers Tegramina-25 grinding and polishing machine.

3.4.2 Light microscopy

As-polished and etched samples were examined using a Nikon Eclipse MA200 optical microscope. The primary objective of optical microscopy was to examine the present morphologies, capture micrographs for overall volume fraction quantification, and to identify different IMP phases based on their color contrast and morphology after etching. Etchants that were trialed includes Keller's reagent, 10% NaOH, and 5% HF. Their effects are illustrated in Figure 3.6. The ideal color contrast between the IMP phases could not be achieved through etching. Furthermore, etching exposed dispersoids in homogenized samples (indicated within the red dotted markings), which overestimated the volume fraction quantification. Consequently, microstructural examination was conducted on as-polished samples.

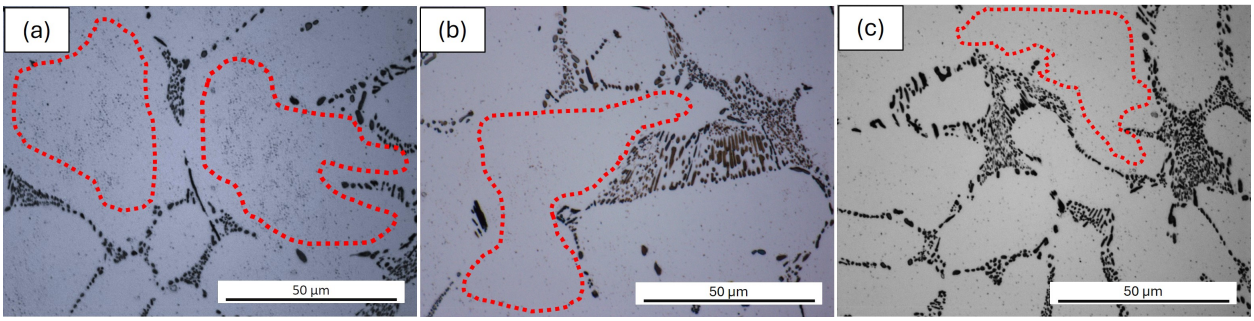

Figure 3.6: Etching Effects of (a) 10% NaOH, (b) 5% HF, and (c) Keller's Solution on intermetallic particles.

3.4.3 Image analysis using ImageJ software

According to the literature, the concept of image analysis for the quantification of the volume fraction (VF), is based on the established Equation (3.1), which demonstrates that the percentage area (A%) can be interpreted as volume fraction (VF) [62].

$$\frac{A}{A_{tot}} = \frac{V}{V_{tot}} \tag{3.1}$$

ImageJ, an open source Java-based image processing application inspired by NIH Image and designed for the Macintosh platform, was used to measure the area fraction of IMPs in the samples. The functional principle of this program hinges on identifying the variation in pixel intensity between the IMPs and the Al matrix in the micrographs. The area fraction is then computed by calculating the ratio of the pixels within a specific intensity range (corresponding to the IMPs) to the total number of pixels in the micrograph.

The optical micrographs were acquired at 100x magnification. Due to the relatively small size of these IPMs, this bigger magnification ensured accuracy when thresholding (shading) the area covered by the IMPs. For statistically meaningful evaluation of the overall volume fraction, an average of 200 micrographs were analyzed. Due to this large quantity of micrographs required, a recorded macro within ImageJ, which is essentially a loop, was used to allow batch

processing of all micrographs in a specified folder. Because of the semi-automation nature of this mode, it was necessary to manually process the micrographs prior to ImageJ processing, to remove micrographs with defects/contamination that might introduce/contribute to data bias. Additionally, the thresholded migraphs were compared to the untresholded micrographs to assess the batch processing accuracy. The associated steps of this process are outlined in appendix A.

3.4.4 Scanning electron microscopy (SEM) paired with Energy dispersive X-ray spectroscopy microscopy (EDX)

The chemical composition of the IMPs was studied to establish a link between their observed morphology and the expected phases, as predicted by JMatPro. To achieve this, SEM coupled with EDS was employed. Solid specimens, carefully polished and mounted on a SEM specimen stub, were analyzed in their unetched state using a Nova NanoSEM 230. An acceleration voltage of 20 keV, with an appropriate spot size and a 6 mm working distance, proved effective for examining the IMPs' composition. Some of the IMP phases were smaller than the interaction volume of the electron beam, which led to readings being influenced by signals from the matrix. As a result, the SEM-EDS data from bulk samples required careful interpretation and occasionally yielded inconclusive results. Therefore, various SEM-EDS techniques, including mapping, line-scan, and spot analysis, were employed to address these challenges.

3.4.5 X-Ray Diffraction on solid/bulk samples

An advanced method of phase identification and quantification of the IMP known as XRD was performed on the unmounted bulk/solid samples with a height of 2mm. The aluminum matrix in the solid samples interfered with the detection of the IMPs, which were present in minimal quantities (approximately 3 wt%). As a result, the XRD spectra predominantly showed peaks related to aluminum, as shown in Figure 3.7. The prominence of these aluminum peaks obscured the smaller peaks necessary for identifying the IMP phases.

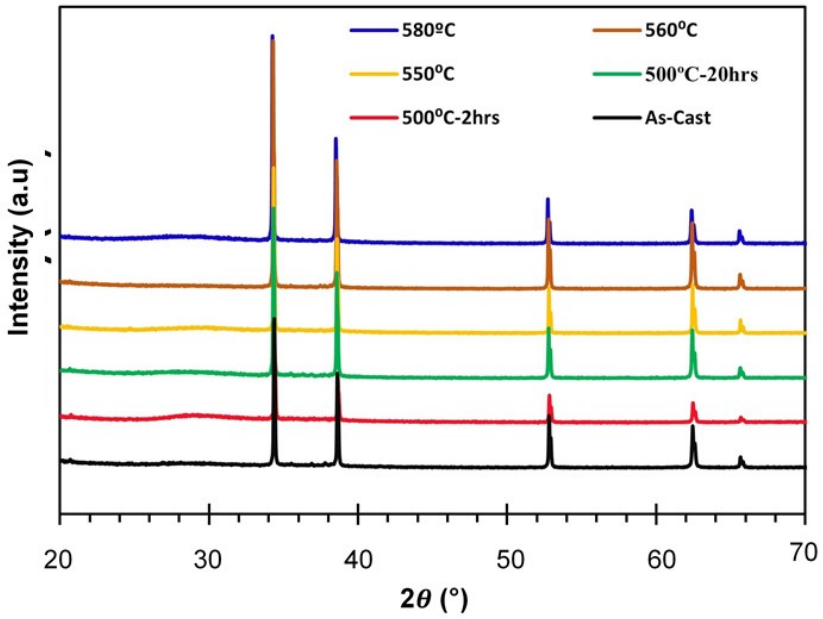

Figure 3.7: XRD spectra of solid AA8021 surface sample.

3.5 3D microstructural characterization

With 2D analysis presenting its own limitations and challenges as explained in subsections 3.4.4 and 3.4.5, 3D technique was then employed as a complementary method. This technique focuses on characterizing powdered samples, where the IMPs were either fully extracted and isolated from the aluminium matrix or partially extracted and left protruding from the aluminium matrix. The detailed processes of complete matrix dissolution, partial dissolution, XRD analysis, SEM-EDS and STEM are outlined in the subsequent subsections 3.5.1 and 3.5.2.

3.5.1 Matrix dissolution and particle extraction using phenol

The common method used for the extraction of IMPs in aluminium alloys is SiBut [63], which involves the dissolution of aluminium in dry 1-Butanol at elevated temperature. The reaction of aluminum with 1-butanol is highly sensitive to water. Therefore, the 1-butanol should be dried prior to the reaction, which is challenging to achieve consistently. Consequently, a different method was used for IMP extraction. In a study conducted by Gupta et al.[63], Sato and Izumi [64], an alternative method to SiBut was explored for particle extraction. This method involves dissolving the aluminum matrix in boiling phenol. The dissolution process proceeds according to the following reaction:

$$\mathrm{Al} + 3\,\mathrm{HOC_6H_5} \rightarrow \mathrm{Al(OC_6H_5)_3} + 1.5\,\mathrm{H_2} \tag{3.2}$$

According to Sato and Izumi [64], the dissolution of a sample with a mass greater than 0.3g results in the formation of aluminum phenolate, which contaminates the extracted powder. Gupta et al. [63] argued and demonstrated that samples with a mass of up to 6g could be dissolved successfully without the precipitation of aluminum phenolate. This argument is well justified, considering that according to Equation 3.2, aluminum phenolate will always form as a byproduct. Therefore, thorough cleaning of the particles after decanting the solvent is necessary. The matrix dissolution setup is shown in Figure 3.8b.

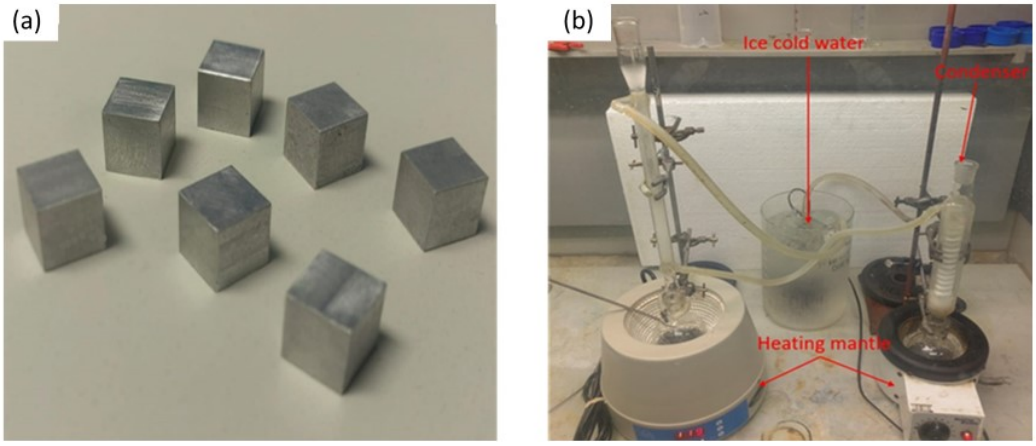

Figure 3.8: As-cast and homogenized samples wire cut from the bulk Al specimen (a) and Particle extraction experiment set-up (b) for IMPs extraction from these cubes.

The 1x1x1 cm^3 solid samples depicted in Figure 3.8a were sliced into 1mm sheets to enhance the surface area and promote a higher rate of reaction. The samples weighed within the range of 2-2.5g. Figure 3.8b illustrates the setup adopted for this procedure in our experiments to extract the IMPs from the cubes shown in Figure 3.8a. In a typical extraction process: 70 ml of molten phenol was measured using a warm measuring cylinder and transferred into a 250 ml round bottom flask and boiled at $182°C$ for approximately 5 minutes to allow for drying (evaporation of water). The sheets were then transferred one at a time into the boiling phenol using tweezers to prevent the phenol from boiling over. Subsequently, the condenser was connected to reflux. The progress of the extraction was monitored by observing the production of hydrogen gas, which was occasionally collected in a balloon fitted at the top of the condenser. Once hydrogen gas production ceased, indicating the completion of the reaction, 70 ml of benzyl alcohol was added to the mixture. The mixture was then left to cool down to room temperature overnight and this allowed the flocculation of the extracted IMPs. Once the IMP precipitated, the solvent was carefully decanted/extracted using a serological pipette and pump, taking care not to draw particles out. The black products were washed in benzyl alcohol repeatedly until the solvent became clear and transparent. These were finally washed twice using methanol. The products were dried in an oven at $50°C$ and weighed on an electronic weighing scale.

3.5.2 Powder X-Ray diffraction

The dried black powders of the extracted IMPs were deposited onto a zero-background silicon (Si) wafer support and characterized using powder XRD on a Bruker D8 advance X-Ray diffractometer, using cobalt (Co) Kα radiation ($\lambda = 0.178897$ nm). The diffraction patterns were recorded between $5 - 120^{\circ}$ (2θ) with a step size of 0.0169322 and at a scan rate of 4 sec/step. The recorded diffraction spectra were loaded into Profex and matched to the peaks of the spectra stored in the database. These stored spectra are phase-specific, enabling phase identification in each sample. However, some expected phases were not found in the database and were subsequently exported from the crystallography open database (COD), which contains a more extensive set of spectra. Additionally, an attempt was made to quantitatively analyze each generated spectrum using the Rietveld refinement method to determine the phase distribution in each sample.

3.5.3 SEM and TEM powder characterization

The SEM-EDX characterization procedure of IMP in 3D was performed on the samples which were deep etched by partial dissolution in phenol. Deep etching involves partially dissolving a surface layer of the bulk sample, exposing the 3D structure of the IMP. The experimental setup for this procedure is identical to that used for complete particle extraction, with the key difference being that deep etching is performed for a shorter duration (approximately 6 minutes), followed by repeated rinsing in hot benzyl alcohol and lastly methanol. Figure 3.9 shows the sample after deep etching, secured in a stub for SEM-EDS examination. The same settings on as in SEM-EDS on solid samples were used.

Figure 3.9: AA8021-AC solid sample on SEM specimen stub after deep etching (partial dissolution)

.

Topographical effects in deep-etched samples commonly causes variation in signal intensities, which may often cause apparent differences in chemical composition. To manage this, TEM and STEM were included as additional characterization techniques of this IMP powder. Specimens for scanning transmission electron microscopy (STEM) imaging were prepared by

drop-casting a colloidal solution onto 3-mm standard carbon-supported films on copper grids. These were air dried under ambient conditions. Samples were analysed using TEM, HR-TEM and STEM on a FEI Osiris FEGTEM instrument, operating at 200 keV. The chemical compositions of individual IMPs were investigated using energy dispersive X-ray spectroscopy (EDS) in STEM mode. Spectrum imaging was used in which an EDS spectrum is obtained at each pixel in the STEM Image, to produce a three-dimensional (3-D) dataset. Slow acquisition and image drift correction were applied during each frame. Scanning TEM (STEM) imaging used bright field and high angle annular dark field (HAADF).

4.Results

The as-cast and homogenized samples from the centre and surface of the AA8021 and AA8079 ingots were analysed using optical microscopy, scanning electron microscopy (SEM) coupled with energy dispersive X-ray spectroscopy (EDS), high-angle annular dark-field scanning transmission electron microscopy (HAADF-STEM) with EDS, powder X-ray diffraction (XRD) and thermodynamic simulations to evaluate and determine the size, morphology, distribution and volume fractions of intermetallic particles (IMPs). The results obtained from these experimental techniques are conveniently categorized into 3 groups:

- thermodynamic prediction of intermetallic particle microstructure.
- evaluation of the as-cast microstructure.
- evaluation of the homogenized microstructure.

4.1 Predicted IMP microstructure using JMatPro

Thermodynamic phase predictions were performed using JMatPro (Version 4.0) to forecast the expected phases and their corresponding volume fractions in the alloys in the as-cast and homogenized conditions. To account for the effect of varying chemical compositions, phase predictions are provided seperately for AA8021 and AA8079 alloys. Table 4.1 summarizes in detail the chemical formulae for the phases identified in these alloys, replacing the default phase designations originally used in JMatPro. M contained in both Al_2Si_2M and Al_3M_DO22 systems represents modifying elements (Sr, Na, Ti, V, etc). Trialuminide Al_3M_DO22 is the stable form in Al-(Ti,V) [65][66].

Table 4.1: The Al-based phase designations and their corresponding chemical compositions from the JMatPro database

chemical formula	Database phase designation
Al_3Fe or $Al_{13}Fe_4$	Al_3Fe
Al_8Fe_2Si	ALFESI_ALPHA
Al_5FeSi	ALFESI_BETA
$Al_{15}(Fe,Mn)_3Si_2$	ALPHA
Mg_2Si	MG2SI
Al_6Mn	AL6MN
Al_9FeNi	AL9FENI
Al_3M_DO22	AL3M_DO22
Al_2Si_2M	AL2SI2M

4.1.1 Equilibrium phases in AA8021 and AA8079

For the composition of AA8021 provided in Table 3.1, JMatpro predicts the phases shown in Figure 4.1(a). This temperature-step plot details the evolution of IMPs in terms of type/phase and volume fraction (in wt%) over the temperature range 25 - 700°C. The plot predicts the presence of at least nine different phases at room temperature in the as-cast condition. These phases include Al_3Fe, $Al_{15}(Fe,Mn)_3Si_2$, Al_5FeSi, Al_2Si_2M, Al_3M_DO22, Al_9FeNi, Mg_2Si and Al_6Mn , with the Al_3Fe being the predominant phase (approximately 2.5 wt%), while the other phases are below 0.5 wt%. Upon heating, at about 180°C, Al_5FeSi dissolves completely, while Al_3Fe slightly dissolves in favour of Al_8Fe_2Si. As the temperature increases in the range 200-490°C, all the other present phases dissolve in favour of Al_3Fe such that only this phase is expected to be present above 500°C. However, above 450°C, Al_3Fe appears to drop in volume fraction without any phase transformation taking place, which is related to the increase in the solid solubility of elements such as Mn and Fe at temperatures above 450°C.

Similarly, based on the composition of AA8079 provided in Table 3.1, JMatpro forecasts the phases presented in Figure 4.1(b). The phases predicted in AA8079 are identical in number and type to those observed in AA8021. However, according to the thermodynamic phase predictions in JMatPro, AA8079 is expected to have significant amount of Al_5FeSi and Al_3Fe between 0 and 180°C, after which they dissolve to form $Al_{15}(Fe,Mn)_3Si_2$ and Al_8Fe_2Si. The stability of these two alpha phases weakens at 350°C with concurrent formation of Al_3Fe that continues to increase in wt%. Above 500°C, $Al_{15}(Fe,Mn)_3Si_2$ is fully consumed while Al_8Fe_2Si rapidly dissolves at the expense of Al_3Fe which exists as the only phase above 580°C.

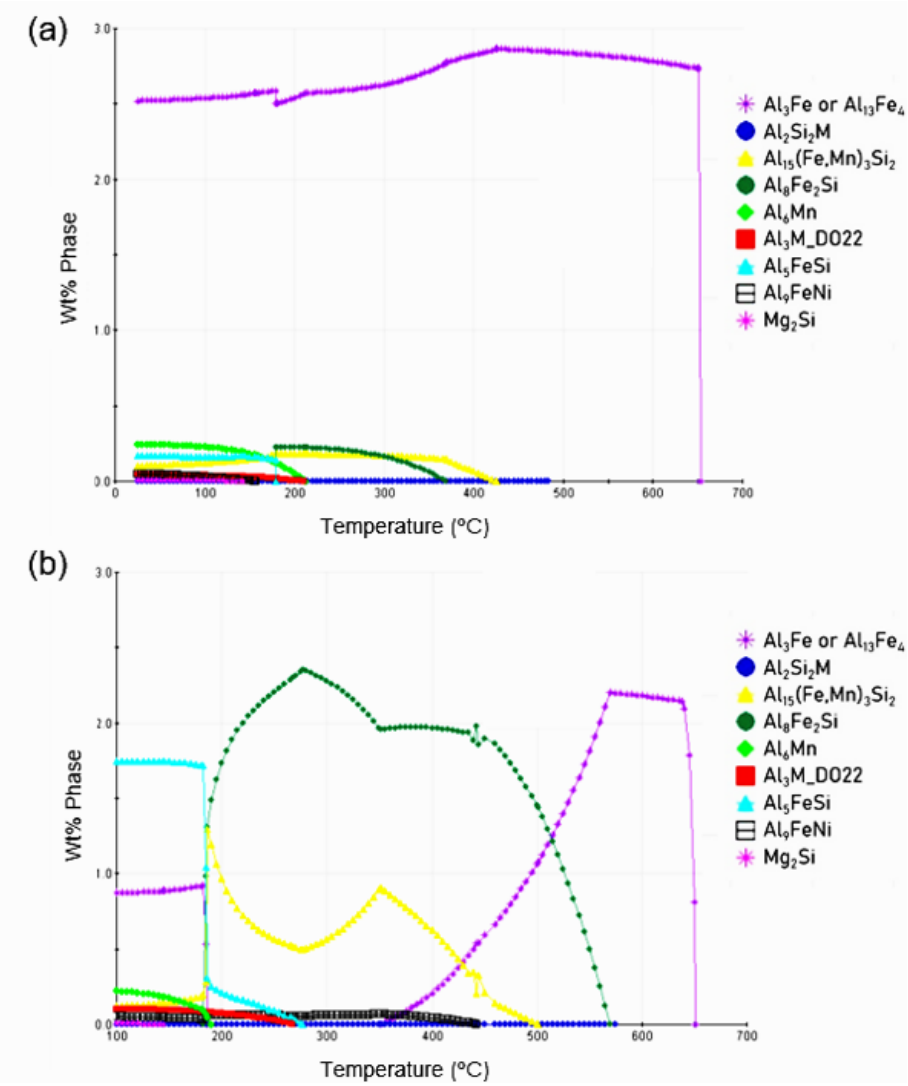

Figure 4.1: Stepped equilibrium calculation of phases in AA8021 (a) and AA8079 (b).

4.2 As-Cast Microstructure Characterisation

To gain insight into the influence of the casting practice, specifically solidification rate and chemical composition, on the development of the IMP microstructure in the as-cast AA8XXX, a comparative analysis of the microstructures was performed on the as-cast samples. First, this analysis focused on the differences between the two alloys; AA8021 and AA8079 that have different chemical compositions.
Second, within each alloy across different regions of the ingots (surface and edge) that experience varying cooling/solidification rates. The qualitative and quantitative findings presented herein encompass the identification of existing morphologies, their respective phases, distributions, as well as the volume fractions and sizes.

4.2.1 Light Microscopy

Figure 4.2 shows optical micrographs of as-polished AA8021 and AA8079 samples in the as-cast state, taken at 100x magnification. The micrographs show a 2D view of the IMP microstructure. The samples were extracted from different regions of the ingots, which experienced varying cooling rates during solidification, as indicated by the black arrow that denotes the direction of increasing cooling rate. As an additional point of emphasis, an intermediate region between the surface and the centre has been included in these light micrographs but will not be discussed in the subsequent sections. The micrographs reveal three distinct characteristic morphologies: needle-shaped, plate-shaped and skeletal morphologies, highlighted in yellow, blue and red, respectively. These morphologies are unevenly distributed in the ingot of individual alloys, and appear to grow along preferred paths/region, forming a long-range network.
In the AA8021 alloy, the skeletal morphology is more prevalent on the surface of the ingot. Moving inward from the surface through the intermediate region toward the centre, a change in the IMP morphology is observed as needle- and plate-shaped morphologies become more dominant. In contrast, the AA8079 alloy predominantly exhibits needle- and plate-shaped morphologies. The needle-shaped morphology is most prominent at the surface, gradually decreasing towards the center, while the plate-shaped morphology increases.

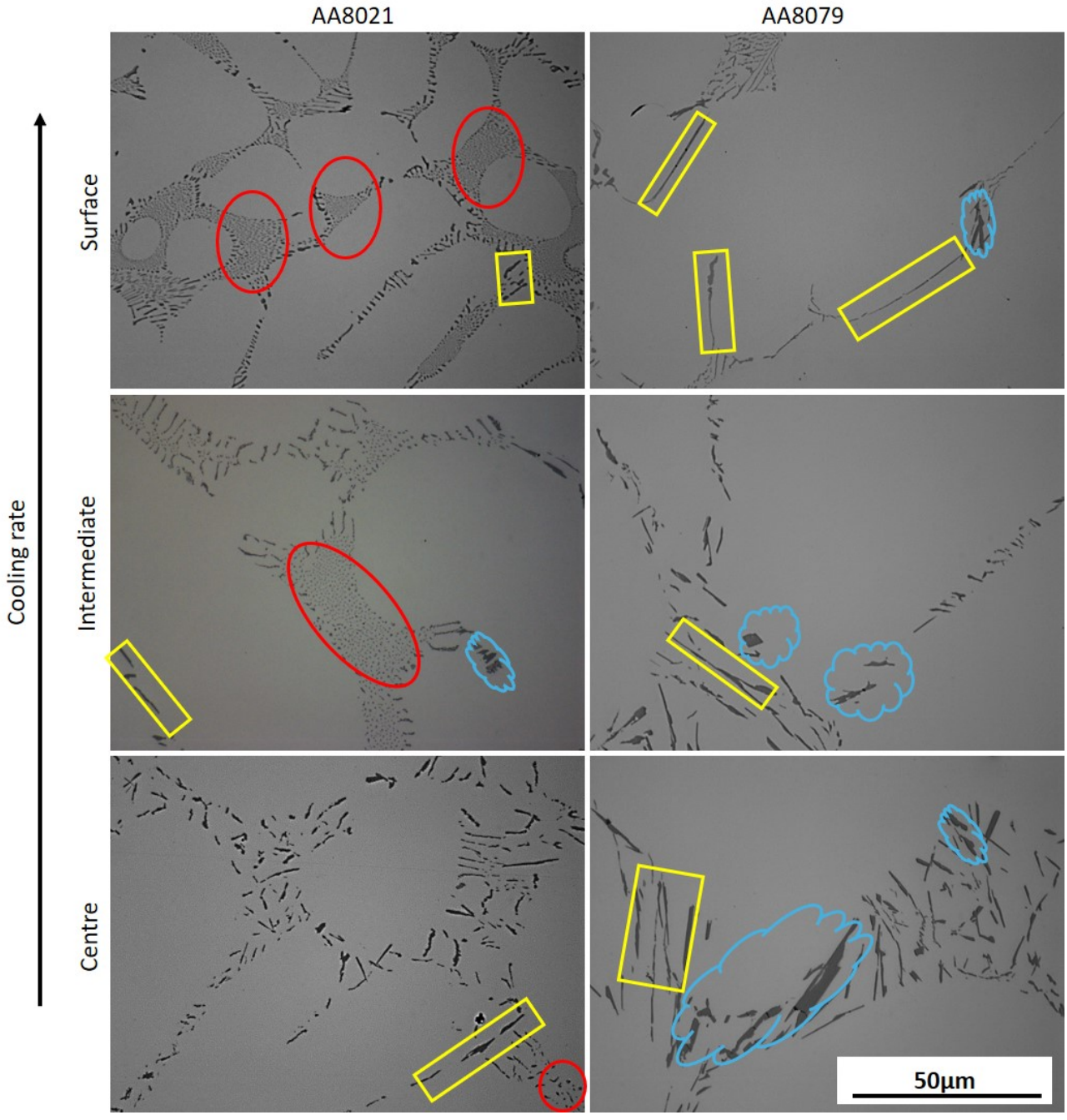

Figure 4.2: As-cast IMP microstructure of AA8021 and AA8079 alloys from surface, intermediate, and center regions of the ingot

.

4.2.2 SEM-EDS

Two-dimensional (2D) imaging techniques often misrepresent the microstructures of the IMPs due to their inherent limitations to flat plane view. Specifically, 2D representations fail to capture critical features such as particle depth, connectivity, and true spatial distribution, all of which are essential for accurate morphological analysis. To obtain a realistic understanding of the IMP morphology, a three-dimensional (3D) perspective is required.

In this study, deep etching of the sample in boiling phenol successfully revealed the 3D structure of the IMPs. However, the surface of the deep-etched sample was uneven and rough, as shown in Figure 3.9, in Subsection 3.5.3. This made light microscopy unsuitable for imaging the IMPs. Thus, SEM was used.

Presenting each sample individually would be redundant and inefficient. Instead, the focus is on reporting and analysing only the distinct morphologies identified across the samples. This is motivated by the established understanding that IMP phases exhibit different morphologies during the solidification process [67],[68]. Nonetheless, the light micrographs in Figure 4.2 provide a preliminary overview of how these morphologies compare among the samples. Therefore, the selected micrographs were chosen to provide a comprehensive overview, specifically highlighting the morphological findings for each alloy across the ingot. Figures 4.3 (a) and 4.3 (b) shows the IMP morphologies present in AA8021. This technique clearly reveals an existing interconnected network of IMPs with three distinct morphologies: skeletal, plate- and needle-shaped morphologies indicated in green, red, and yellow, respectively. The skeletal morphology observed in 2D view in Figure 4.15, display a feathery-shape in 3D, where rod-like or needle-like structures stick out from the main stem. Notably, AA8021 surface sample is predominantly characterised by this skeletal morphology, with traces of plate-like morphology also present.

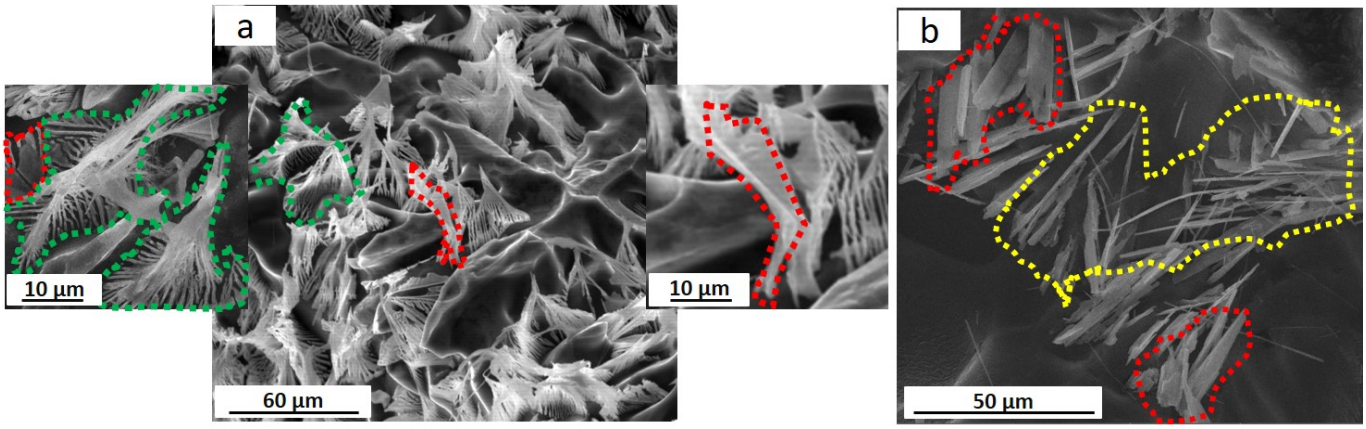

Figure 4.3: SEM backscatter electron micrographs of deep-etched AA8021-AC samples, illustrating the different morphologies across different regions of the ingot: (a) surface and (b) center, with distinct phases outlined using various colors.

Unlike the morphologies observed in AA8021, the as-cast ingot of AA8079 exhibited two

distinct morphologies: needle-shaped structures (highlighted in red) and plate-shaped structures (indicated in yellow). These features are shown in Figure 4.4(a) and Figure 4.4(b).

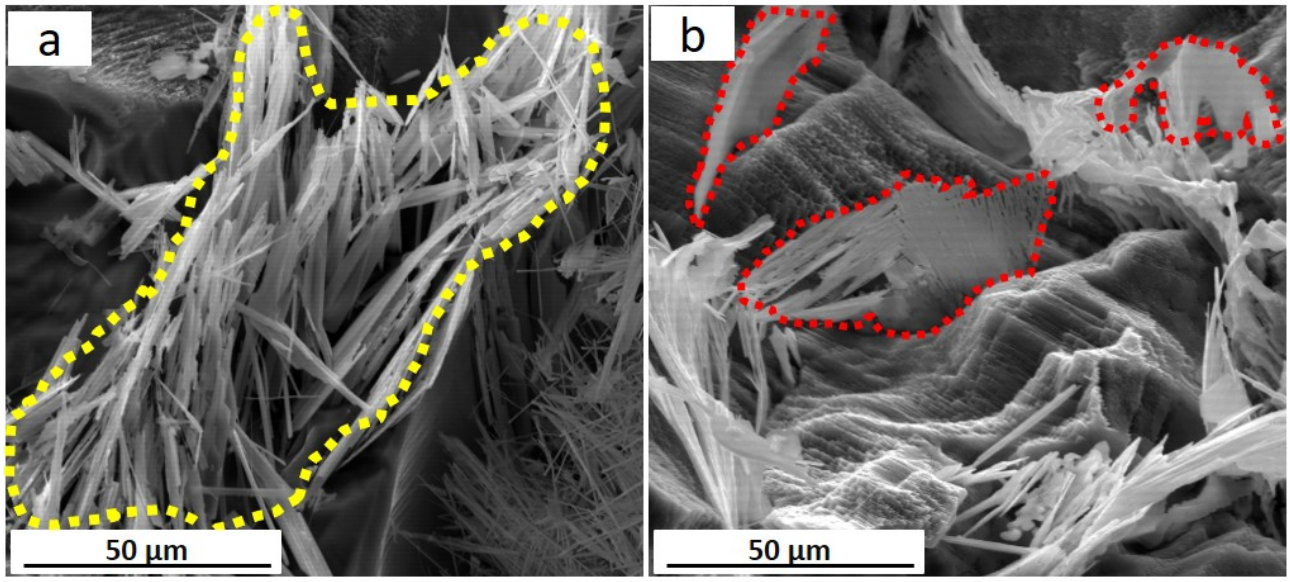

Figure 4.4: SEM backscatter electron micrographs of deep-etched AA8079-AC samples, illustrating the different morphologies across different regions of the ingot: (a) surface and (b) center, with distinct phases outlined using various colors.

To identify the phases associated with these morphologies, qualitative and quantitative SEM-EDS analyses were performed. However, elemental mapping and quantification on as-polished samples proved to be challenging because the interaction volume exceeded the size of some IMPs. Figure 4.5 presents the results of SEM-EDS mapping attempts on the three distinct morphologies. In Figure 4.5a, mapping the skeletal-shaped morphology with size less than 3μm, EDS does not reveal any significant elemental differences between the matrix and the IMPs. A similar observation was made for needle-shaped morphology, with thicknesses also below 3μm, as indicated by the arrows in Figure 4.5b. In this morphology, only Fe was identifiable using this technique. In contrast, the elemental mapping of the plate-shaped morphology in Figure 4.5b shows Al, Fe, and Si as the principal elements. The Si content appears notably low.

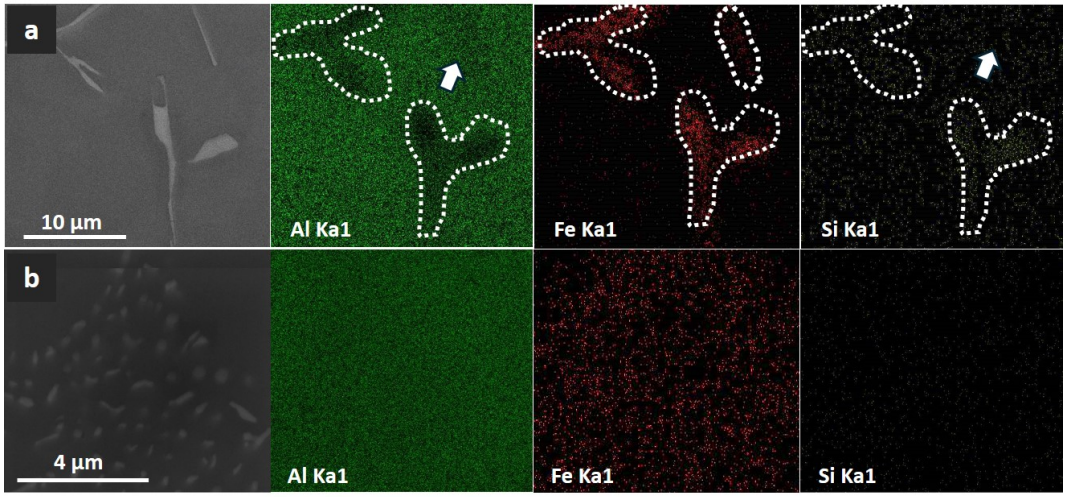

Figure 4.5: SEM-EDS mapping of skeletal (a), and needle- and plate-shaped (b) morphologies in an as-polished specimens.

SEM-EDS using spot analysis was performed to quantify the elemental composition of the distinct morphologies. Figure 4.6 highlights the skeletal-shaped, needle-shaped, and plate-shaped morphologies in green, yellow, and red, respectively, where the analysis was conducted. The results, summarized in Table 4.2, indicate that only Al and Fe were detected in the skeletal and needle-like morphologies. In contrast, the plate-like morphology contains traces of Si.

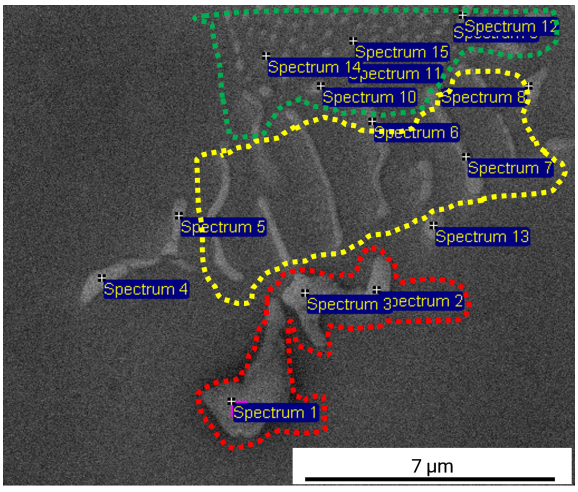

Figure 4.6: SEM-EDS spot analysis on deep-etched skeletal morphology

Table 4.2: SEM-EDS elemental analysis of Al, Fe and Si in different Morphologies of an as-polished sample (at%)

Spectrum	Al	Si	Fe	Total
1	78.2	1.86	19.94	100
2	77,9	0.8	21.30	100
3	93.02	0	6.98	100
4	89.77	0	10.23	100
5	91.34	0	8.66	100
6	93.27	0	6.73	100
7	88.51	0	11.49	100
8	93.21	0	6.79	100
9	90.51	0	9.49	100
10	93.65	0	6.35	100
11	92.92	0	7.08	100
12	92.35	0	7.65	100
13	88.22	0	11.78	100
14	100	0	0	100
15	93.85	0	6.15	100

To minimize the influence of the matrix on the SEM-EDS results, mapping was performed on deep-etched samples for the identified morphologies. Figure 4.7a and 4.7b show that the skeletal and needle-shaped morphologies contain Al, Fe, and Si. Despite the height differences where the IMPs protrude above the matrix (circled in white dashed lines), EDS analysis shows that the IMPs contain less Al and more Fe compared to the matrix. The Si content shows minimal variation between the IMPs and the matrix, making qualitative distinctions challenging.

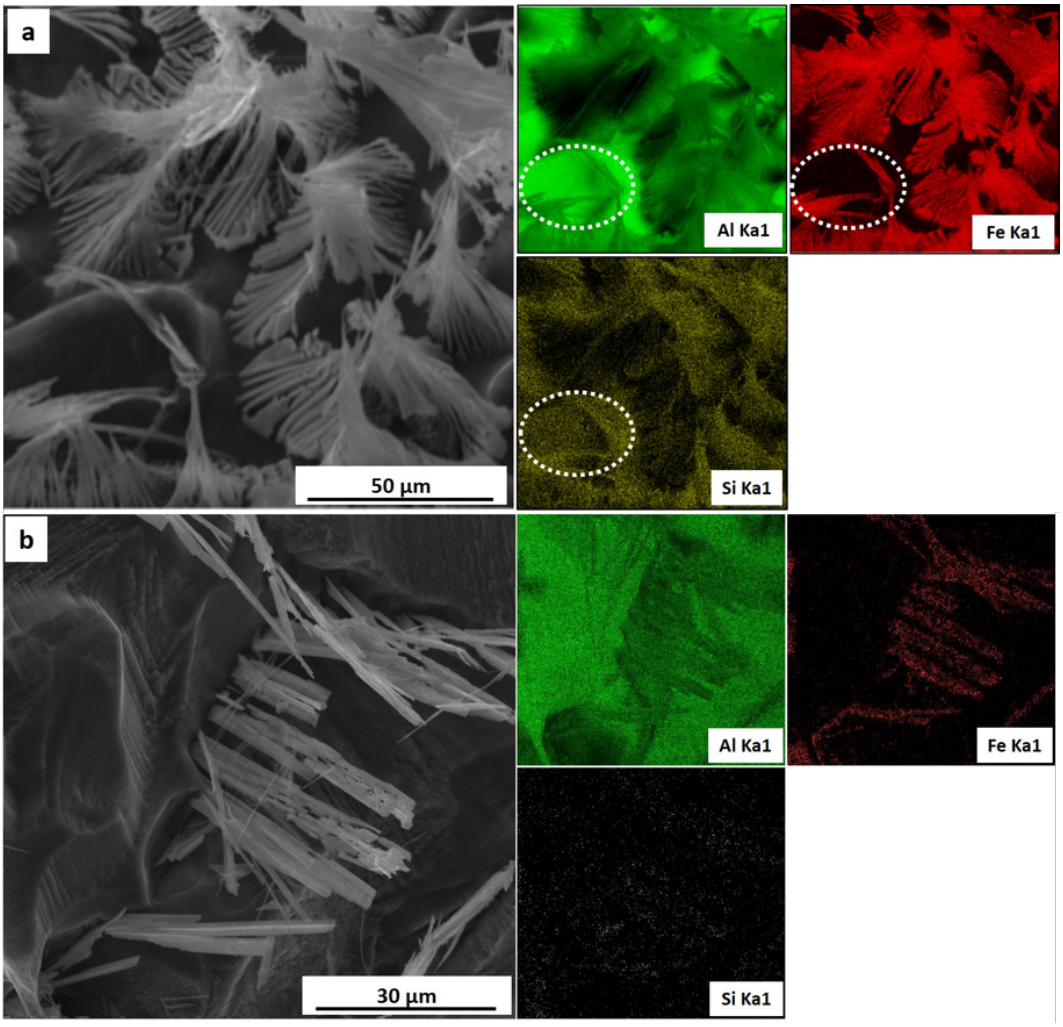

Figure 4.7: SEM-EDS mapping of skeletal feathery (a), needle- and plate-shaped (b) morphologies after deep etching.

These observations were further investigated using SEM-EDS line-scanning on bulk samples. This technique shows how the elemental abundance changes across a region of interest as the electron beam scans through it. The measured line-scans across skeletal, plate- and needle-shaped morphologies are presented in Figures 4.8a,b and c respectively. These scans also show a decrease in Al, an increase in Fe, and an almost constant Si content from the matrix across the IMPs.

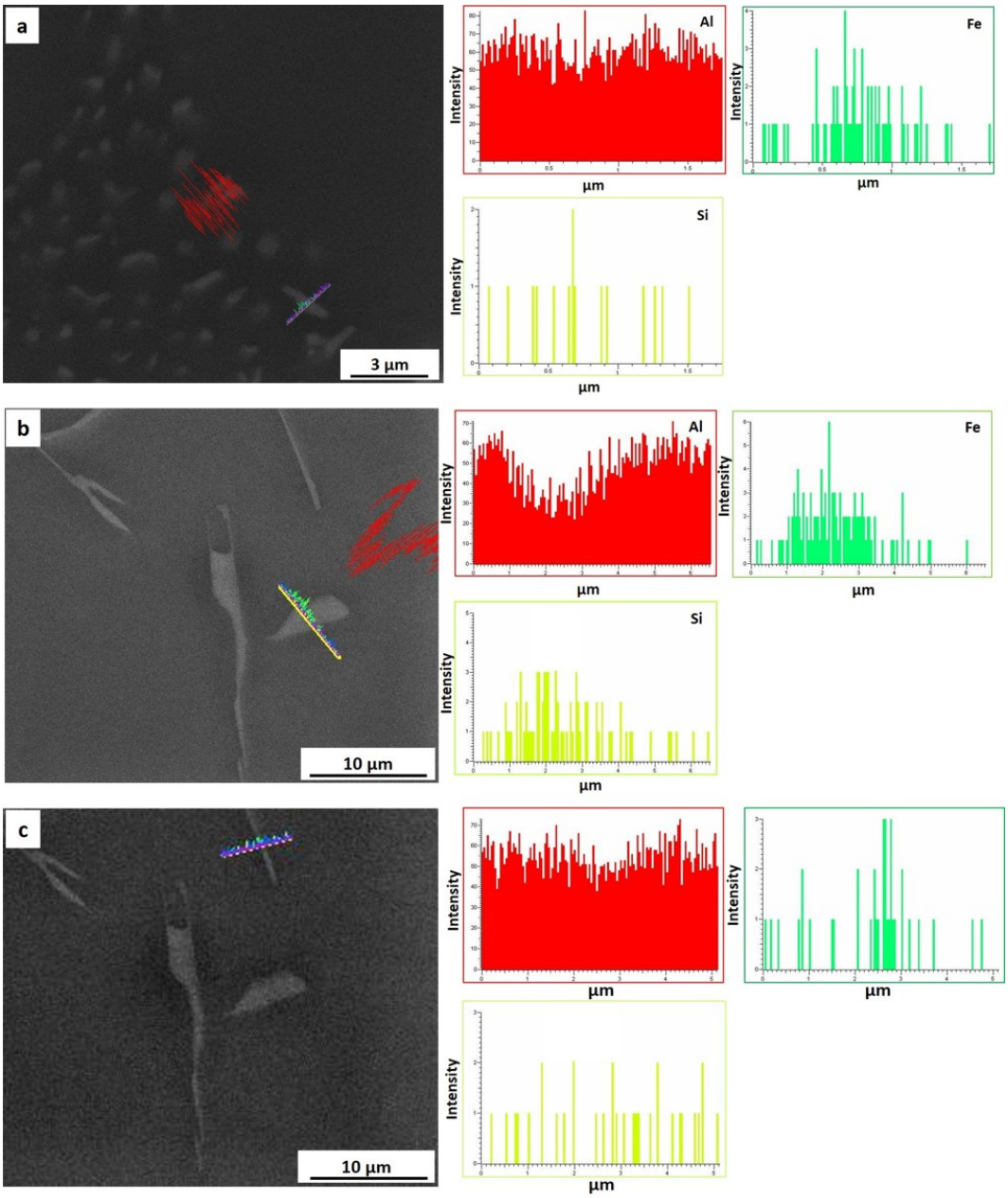

Figure 4.8: SEM-EDS line scan across skeletal (a), plate-shaped (b) and needle-shaped morphologies in as-polished specimens.

Again, in the absence of the matrix interference, spot analysis yielded some useful data despite the possibility of signal scattering. From the spot analysis carried out on the different morphologies, the ratios of Al:Fe were calculated, and the resulting stoichiometric ratio was used to identify the type of phase associated with that specific morphology. Figure 4.9 and Figure4.10 show the 3 previously identified morphologies and the corresponding areas where the different spot analysis was performed. The corresponding readings, the calculated Al:Fe ratios, and the phase assignment are shown in Tables 4.3 and 4.4. The resulting calculations indicate that the skeletal morphology is associated with the Al_mFe, while needle-shaped and plate-shaped morphologies are associated with Al_6Fe and Al_3Fe respectively.

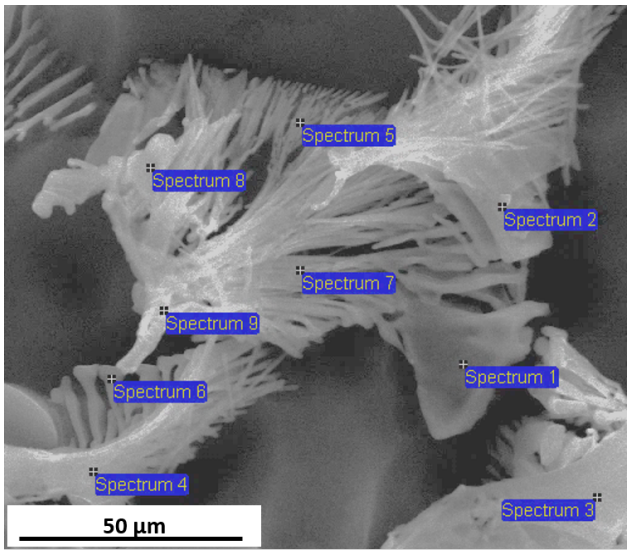

Figure 4.9: SEM-EDS spot analysis on deep-etched skeletal morphology

Table 4.3: SEM-EDS spot measurements on skeletal-shaped morphology in at.%

Spectrum	Al	Si	Fe	Al:Fe	Phase
1	75.73	0.09	24.18	3.13	Al_3Fe
2	78.01	0.9	21.09	3.69	Al_3Fe
3	73.59	0.56	25.85	2.84	Al_3Fe
4	79,43	1.64	18.93	4.20	Al_mFe
5	80.52	1.82	17.66	4.56	Al_mFe
6	85.23	0.72	14.05	6.07	Al_6Fe
7	72.71	2.52	24.77	2.94	Al_mFe
8	77.36	1.84	20.80	3.72	Al_mFe
9	78.98	1.53	19.49	4.05	Al_mFe

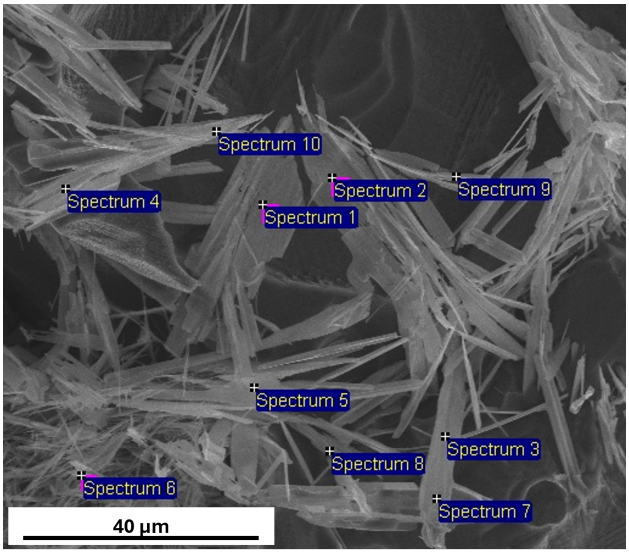

Figure 4.10: Figure 4.15: SEM-EDS spot analysis on deep-etched needle- and plate-shaped morphologies.

Table 4.4: SEM-EDS spot measurements on needle- and plate-shaped morphologies in at.%

Spectrum	Al	Si	Fe	Al:Fe	Phase
1	75.26	2.89	21.85	3.44	Al_3Fe
2	72.42	2.24	25.34	2.86	Al_3Fe
3	73.21	1.65	25.14	2.91	Al_3Fe
4	74.31	3.12	22.57	3.29	Al_3Fe
5	84.62	0.64	14.74	5.74	Al_6Fe
6	66.13	0.95	32.92	2.01	-
7	70.78	2.82	26.4	2.68	Al_3Fe
8	71.37	2.21	26.42	2.70	Al_3Fe
9	86.53	0.01	13.46	6.42	Al_6Fe
10	85.4	0.59	14.01	6.10	Al_6Fe

4.2.3 HAADF-STEM and STEM-EDS

Figure 4.11a and Figure 4.11b show representative bright field BF-TEM and HAADF-STEM micrographs of the as-extracted IMPs from the aluminium matrix, respectively, using phenol. These IMPs are observed to contain mixtures of elongated, rod-like, dendritic, near-spherical, irregular, and cuboidal morphologies. Figure 4.11c is an image acquired using HR-TEM, which reveals that the IMPs have visible continuous lattice fringes orientated in the same direction. This suggests that the IMPs have a characteristic single crystalline structure. In addition, the fast Fourier transform (FFT) extracted from the HR-TEM image (inset in Figure 4.16c) also confirms that the selected individual particle is a perfect single crystal.

The elemental distributions within individual IMPs were determined using HAADF-STEM coupled with energy dispersive X-ray spectroscopy (EDS). Figure 4.12(a-e) shows HAADF-STEM micrograph and the corresponding elemental maps of the individual IMP. STEM-EDS analysis of the highly branched dendritic structures suggests that they are pure Al oxide, this being the remnants of the purification process. The rest of the darker geometries are IMPs. The composite EDS map of the nanorod-shaped particle reveals uniform compositional distributions of Al, Fe and Si (Figure 4.12e) within the IMP. Furthermore, cross-sectional intensity profile (Figure 4.12f) extracted along the maximum length (white arrow) from the EDS spectrum image shows the IMP to have Al-enrichment on the surface, with the corresponding atomic ratios of Al_3Fe (Si less than 1 at.%). The STEM-EDS results mapping results in show that silicon Si content in these IMPs is insignificant in these IMPs, resulting in Si noise covering the outer sides of the IMPs.

This is not a true representation of Si proportion within the IMPs. To avoid the noise

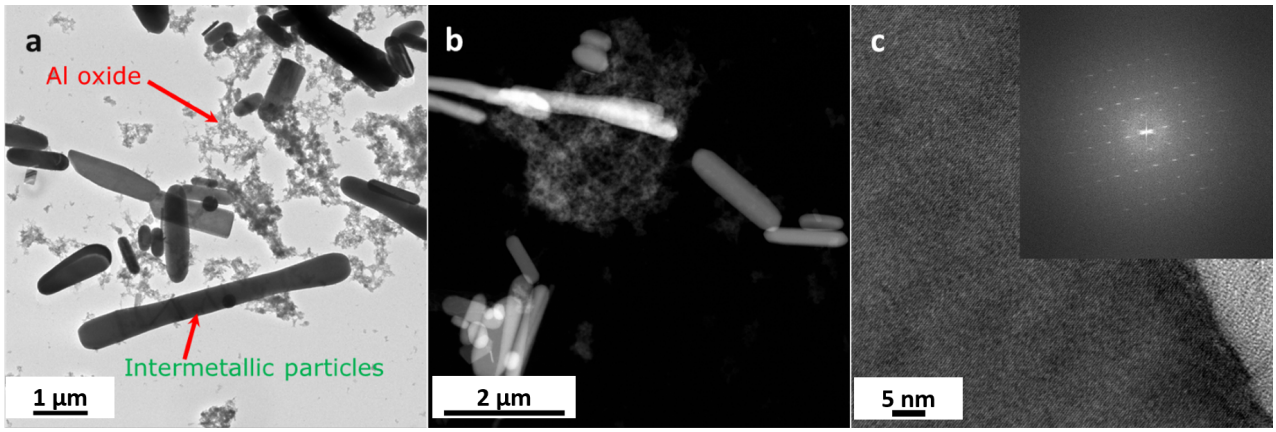

Figure 4.11: BF-TEM (a), HAADF-STEM (b) and HR-TEM (c) micrographs of the as-extracted IMPs. The inset in (c) is the corresponding FFT.

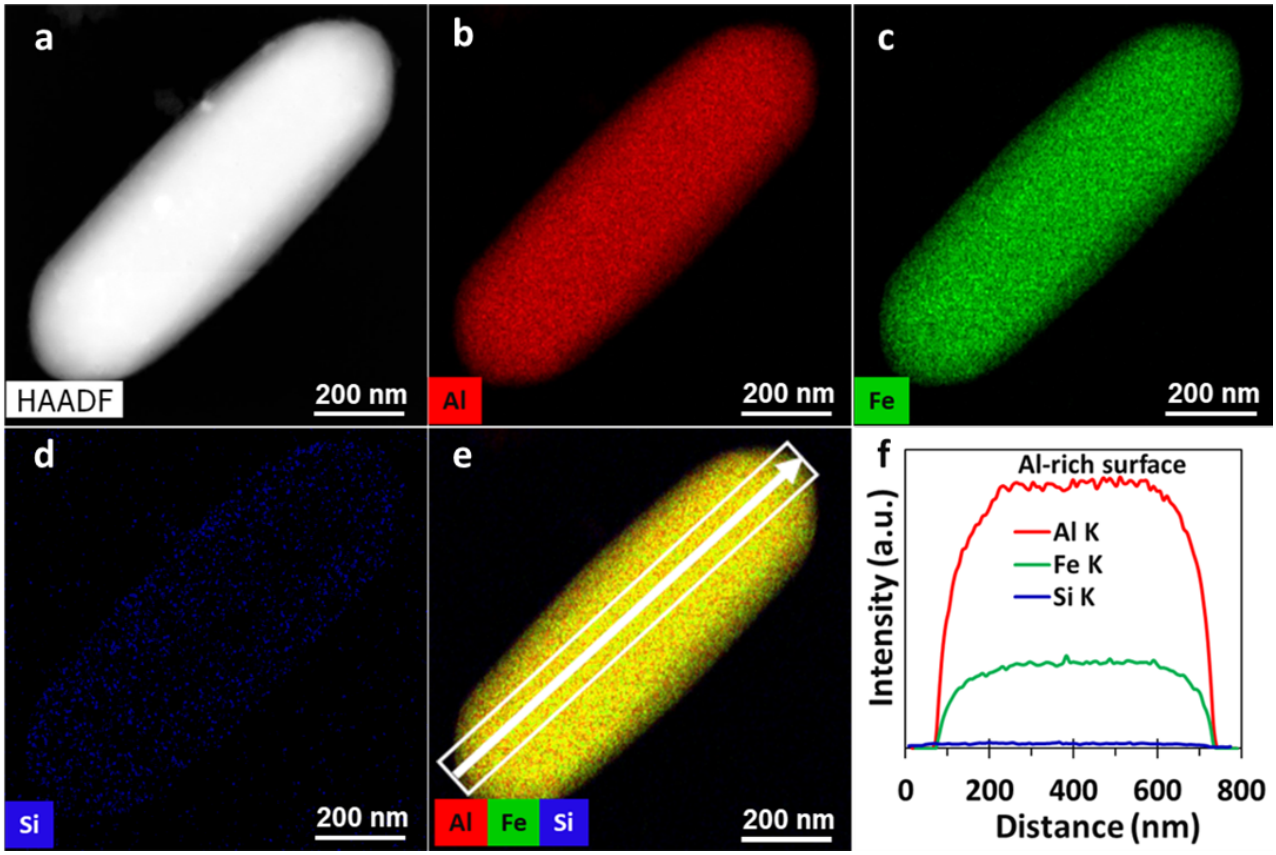

Figure 4.12: HAADF-STEM micrograph (a), STEM-EDS maps of Al (b, red), Fe (c, green), Si (d, blue) and the associated composite EDS map (e). The line scan profile (f), extracted along the white line path in the composite map in (e).

interference with the approximate Al:Fe ratios, the Si analysis was excluded in Figure 4.13. Additional STEM-EDS imaging and the composite EDS maps were performed on randomly chosen different geometries of the IMPs, as shown in Figure 4.18(a-c). Although these different

morphologies show similar homogeneous distributions of Al and Fe within the IMPs, their estimated ratios were estimated as Al:Fe ratios were 6:1 (Figure 4.13a), 2.8:1 (Figure 4.13b) and 4:1 (Figure 4.13c), which correspond to the Al_6Fe, Al_3Fe and Al_mFe phases, respectively.

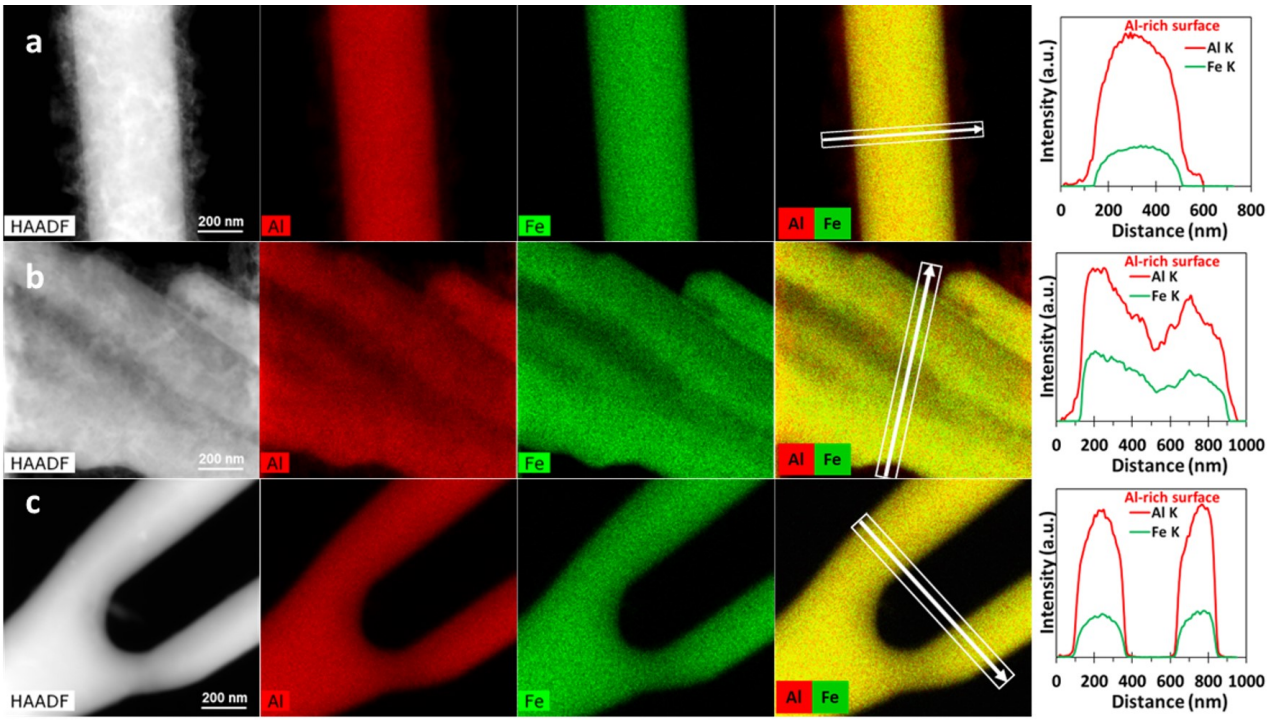

Figure 4.13: HAADF-STEM micrograph (a-c, first column), STEM-EDS elemental maps of Al (red, second columnb), Fe (green, third column) and the corresponding composite EDS maps illustrating uniform distribution of Al and Fe within the IMPs (fourth column). The line scan profiles (last column) extracted along the white line path in the composite maps (fourth column).

4.2.3.1 XRD

XRD measurements were conducted to evaluate the crystalline nature of the IMP powder. The resulting spectra were analyzed using Profex, which enabled the identification and matching of peaks to identify the IMP phases present in the samples. The peak assignments were performed manually using labeled shapes for ease of illustration and interpretation, as shown in Figure 4.14. This is the spectra for the AA8021 surface sample in different conditions. The spectra for other samples are presented in the appendix C. XRD patterns confirm that these IMPs are crystalline in nature. From these spectra, some peaks are narrow and well-defined with apex tips, while some are broad with tiny sub-peaks. However, most peaks were positively matched, and the resulting phases are summarized in Table 4.5. The as-cast condition, (AA8021) contains three phases: Al_6Fe, Al_3Fe and Al_mFe, with corresponding crystallographic reference numbers; MP-570001, COD-1571554 and COD-1571553 respectively. These phases are distributed unevenly in the ingot, with Al_mFe only existing at the surface of the ingot. Conversely, the AA8079 contains only Al_6Fe and Al_3Fe, which occur in both surface and central regions. Quantitative analysis of the phases using the Rietveld method was unsuccessfully attempted due to peak broadening and some of the peaks which could not be positively matched.

Table 4.5: Identified IMP phases in As-Cast AA8021 and AA8079 alloys using XRD

	AA8021-Surface	AA8021-centre	AA8079-surface	AA8079-centre
Al_mFe	✓	✗	✗	✗
Al_6Fe	✓	✓	✓	✓
Al_3Fe	✓	✓	✓	✓

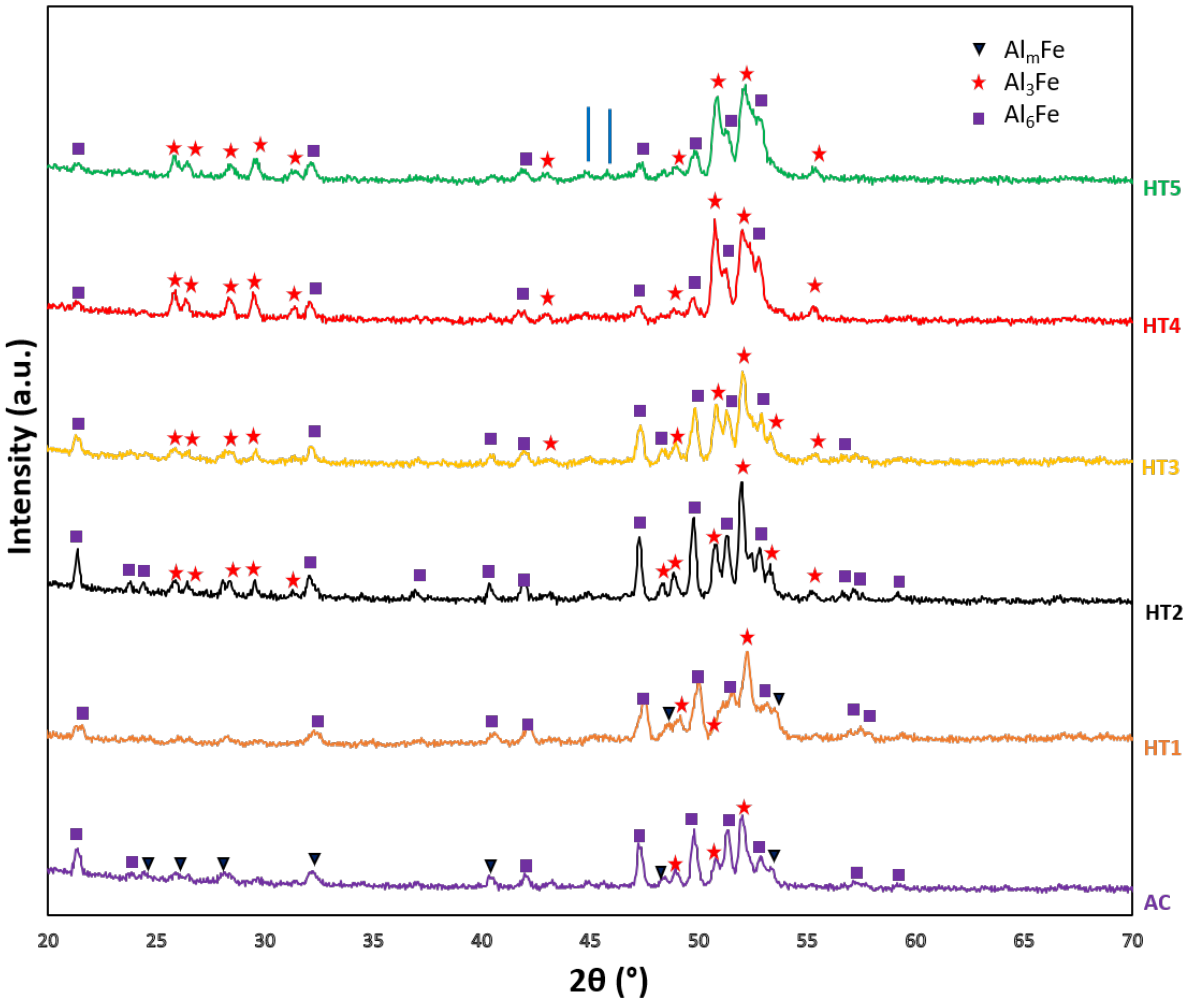

Figure 4.14: XRD Spectra of AA8021 Surface Sample with Peak Assignments

4.2.4 Volume fraction quantification

Accompanying the aforementioned IMP microstructural trends, is a variation in area/volume fraction across the ingot and between the alloys. Figure 4.15 shows how the IMP volume fractions compare between the alloys and different regions (surface and centre), in the as-cast state. The graph reveals two primary trends regarding the volume fraction of IMPs.

Firstly, there is a notable difference in the overall volume fractions between the two alloys. The AA8021 alloy consistently exhibits a higher overall volume fraction compared to AA8079, highlighting the distinct chemical composition characteristics.
Secondly, variations in the overall volume fraction are observed within the ingot of each alloy, that is, across the different regions. The surface region displays the highest proportion of IMPs, with a decrease observed as the region shifts from the surface through to the centre.

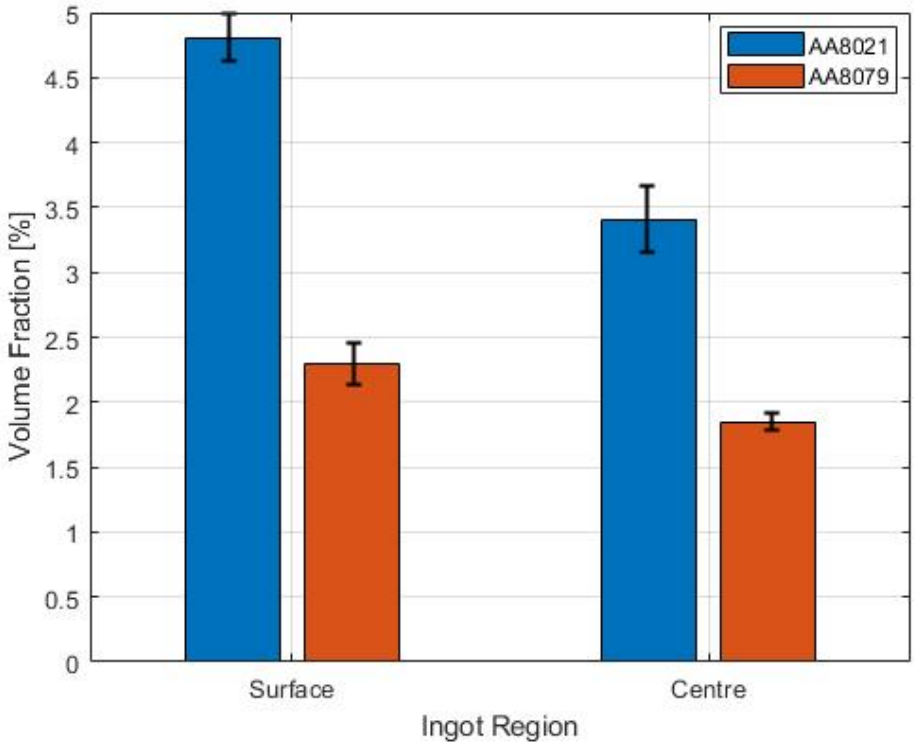

Figure 4.15: Volume fractions of IMP in As-Cast AA8021 and AA8079 Aluminum Ingots across 3 regions

.

To obtain statistically reliable data, various stereological measurements were conducted. First, to address the possible error contribution by field-to-field variation, the number of fields of view (n) or number of micrographs required to calculate and report reliable average volume fraction was determined by plotting the number of fields of view (n) against the volume fraction. The range of n over which the average volume fraction plateaued was identified and, a value n was selected within this range to approximate the average volume fraction. Figure 7.18 shows various plots for the surface sample of AA8021 alloy, under all six different conditions (AC, HT1, HT2, HT3, HT4 and HT5), while plots for all other samples are provided in Appendic D. Examining the starting points of the red horizontal lines of the plots, it is evident that the minimum number of fields of view required to calculate a meaningful average volume fraction varies among the samples. Furthermore, it is observed that micrographs or number of fields of view fewer than 50, yields unstable average values.

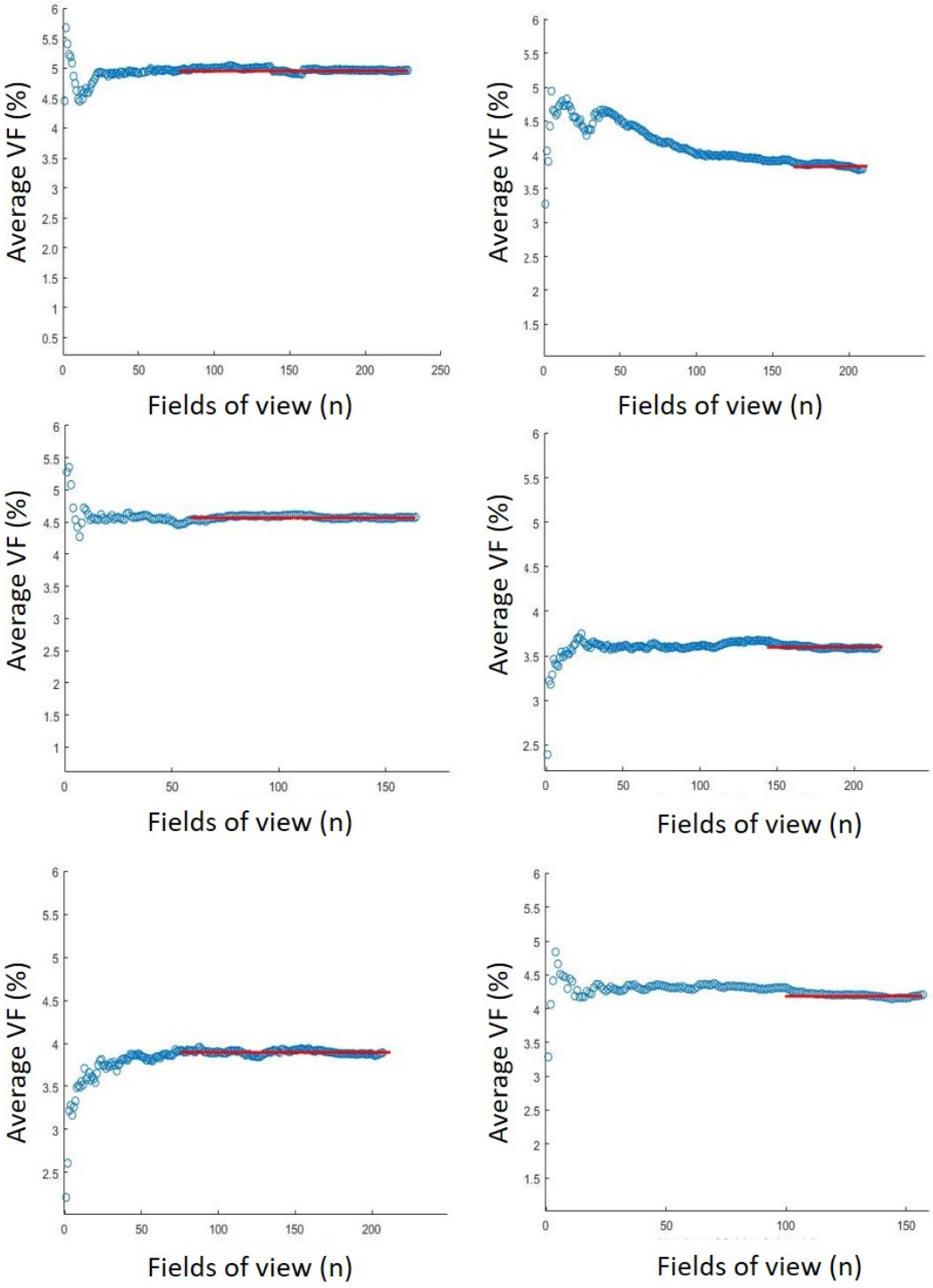

Figure 4.16: Minimum number of fields of view required to obtain a statistically meaningful volume fraction in AA8021 surface sample under different processing conditions

.

In the subsequent stereological measurements, the volume fraction data was evaluated for its distribution, to assess if it followed a normal distribution. Figure 7.21 shows the

distributions of volume fractions of the surface samples of AA8021 under all six different conditions (AC, HT1, HT2, HT3, HT4 and HT5). The distributions for all other samples are provided in the Appendices 7.1. These distributions confirm that the volume fraction data are normally distributed and the mean is a relevant measure of central tendency. Using equations 4.1 and 4.2, the 95% confidence interval (CI) and the subsequent percentage relative frequency (RF) were calculated. The results showing the relationship between the percentage relative frequency and the number of fields of view, 'n' are presented in Tables 7.3 and 7.4, in the appendices. An illustration of the observed trend is presented in Figure 4.17. This shows that the volume fraction estimation becomes more acceptable/accurate as the fields of view increase.

$$95\%\ \text{CI} = \pm\frac{zs}{\sqrt{n}} \tag{4.1}$$

$$\text{RA} = \frac{100 \times 95\text{CI}}{\mu} \tag{4.2}$$

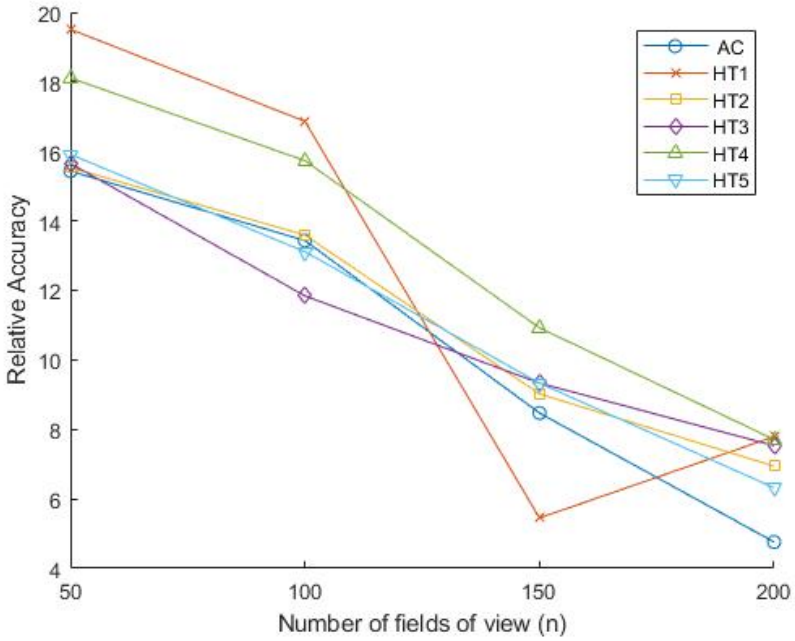

Figure 4.17: Relationship between relative accuracy and number of fields of view

.

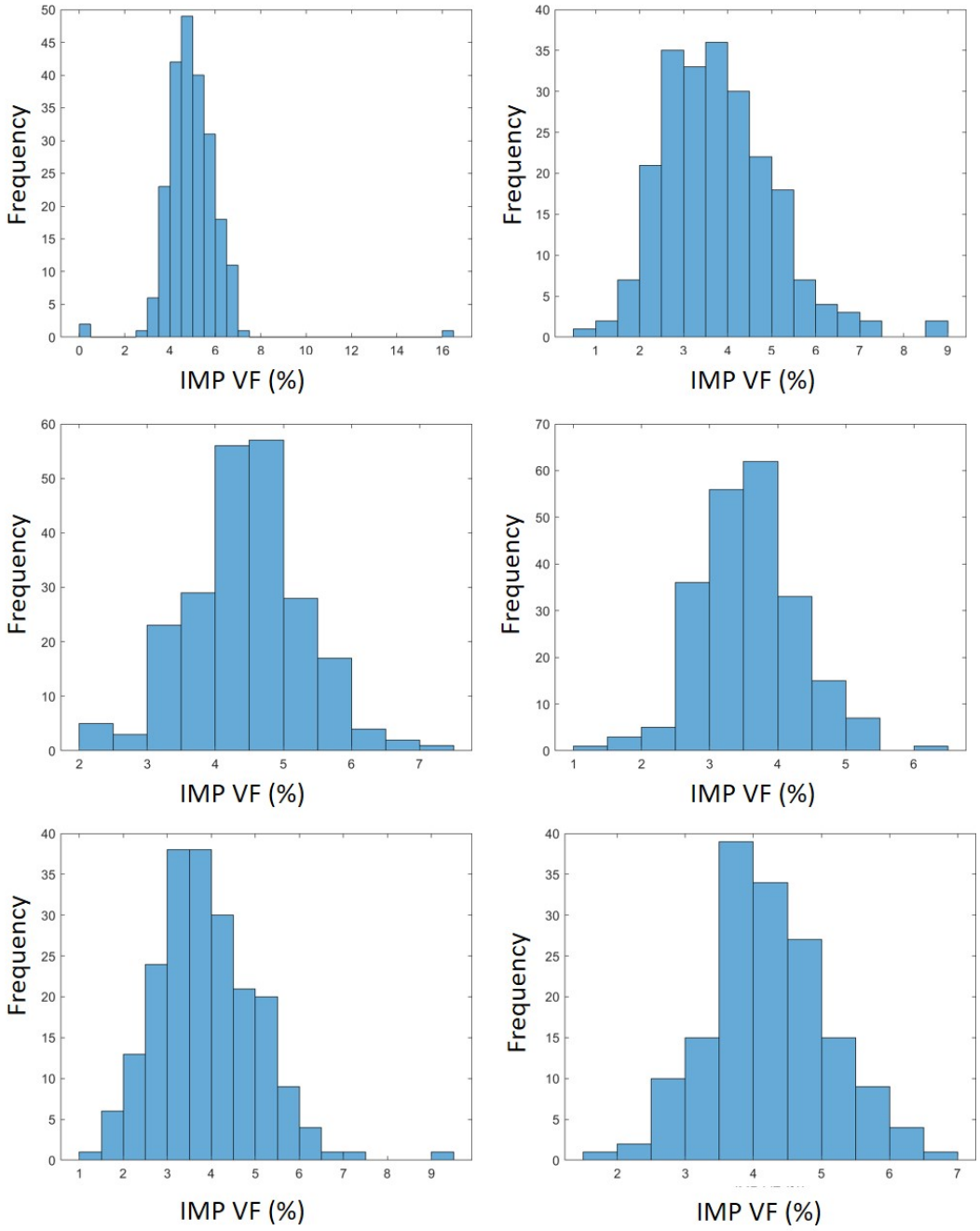

Figure 4.18: Distribution of volume fractions from approximately 200 fields of view in AA8021 surface under different processing conditions.

4.3 Homogenized microsctructure characterization

Two types of AA8XXX alloys (AA8021 and AA8079) were subjected to five different homogenization treatments: HT1, HT2, HT3, HT4, and HT5, to evaluate the impact of homogenization treatments on the IMP microstructure. The investigation examines changes in morphology, phase composition, volume fraction, and size of the IMPs resulting from these thermal treatments. Thus, the findings presented here provide information on the microstructural transformations induced by homogenization.

4.3.1 Light microscopy

Five different homogenization treatments were successfully carried out on samples extracted from the two regions of interest; the surface and centre of the AA8021 and AA8079 alloys. The optical micrographs shown in Figure 4.19 illustrate the 2D view of homogenization effects on IMP microstructure in the AA8021 surface samples. Similarly, Figure 4.20 demonstrates the evolution of IMPs in the AA8079 centre samples. For reference, supplementary micrographs for regions not presented in this section are provided in the appendix B.
In the surface samples of AA8021, the 2D view shows minimal changes in IMP microstructure across the various homogenization treatments. There is an increase in the spacing between branches of the skeletal morphology (highlighted in red). This indicates a transition from a fine, highly dense skeletal structure to a slightly coarser morphology.
The AA8079 center sample, which shows both needle-shaped and plate-shaped morphologies, demonstrates a notable transformation in the IMPs (highlighted by red dotted lines). As homogenization temperature and duration increase, the needle- and plate-like morphologies gradually spheroidize and become bulkier.

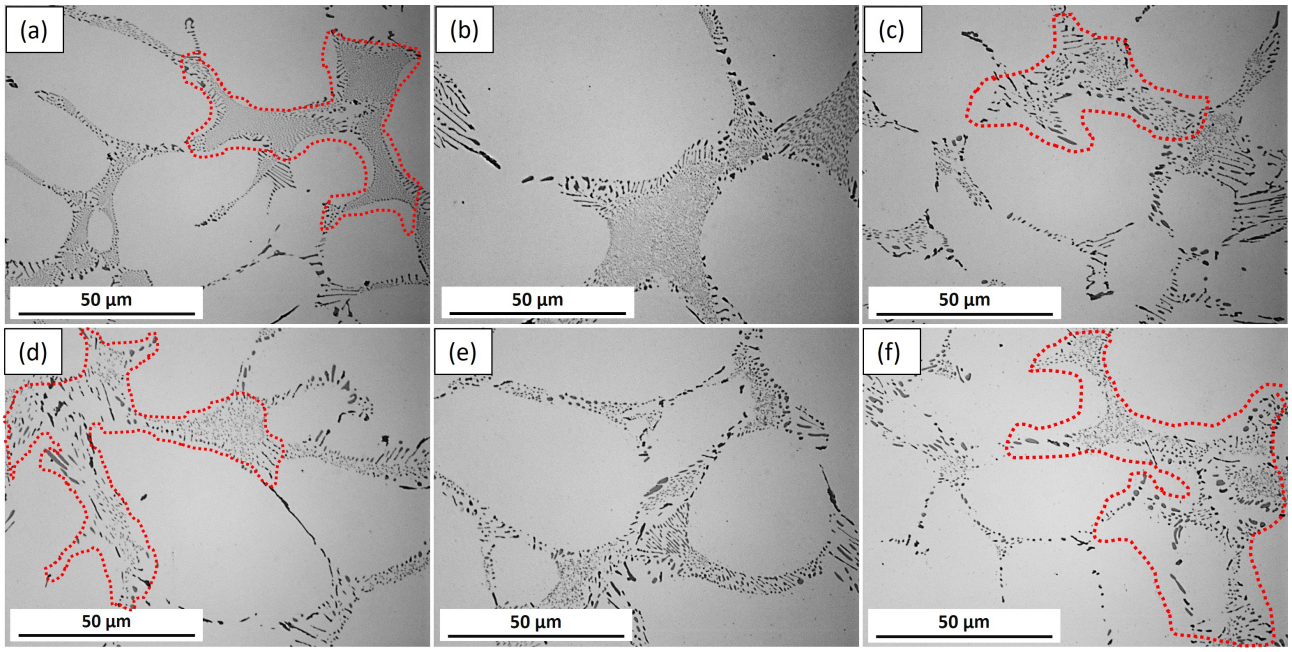

Figure 4.19: Optical micrographs showing the evolution of IMP in AA8021 surface from (a) AC condition through different homogenization treatments: (b) HT1, (c) HT2, (d) HT3, (e) HT4, and (f) HT5.

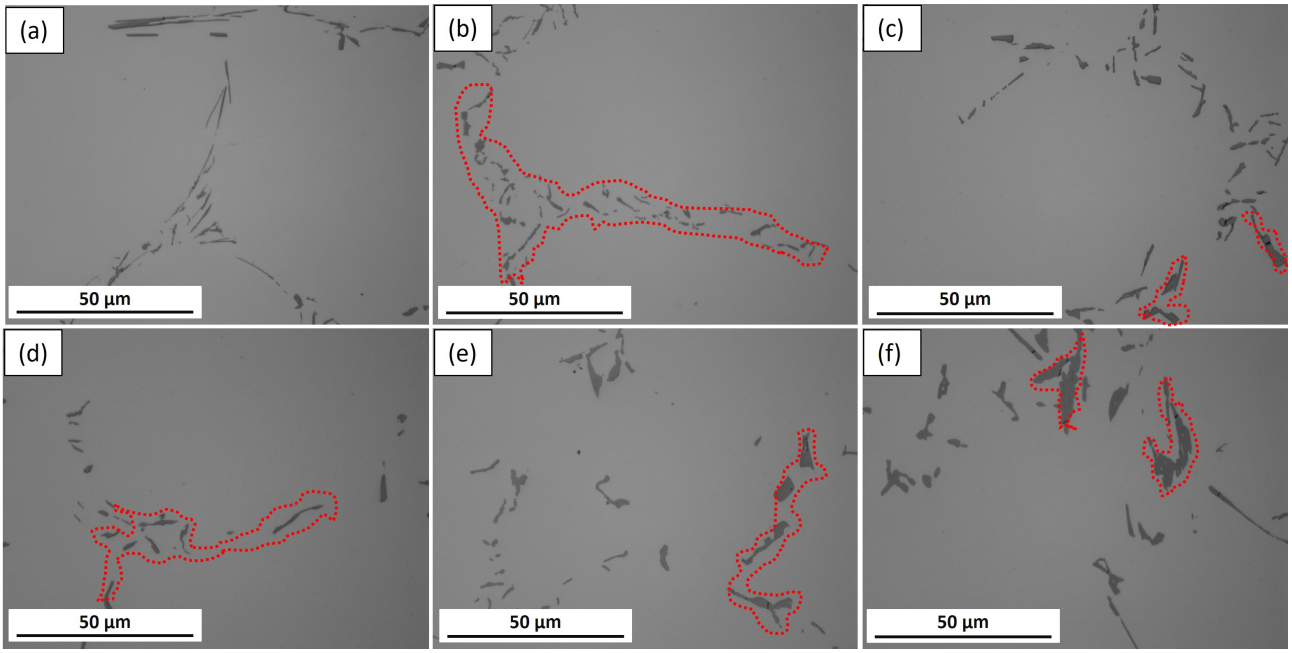

Figure 4.20: Optical micrographs showing the evolution of IMP in AA8079 centre from (a)AC condition through different homogenization treatments: (b) HT1, (c) HT, (d) HT3, (e) HT4, and (f) HT5.

4.3.2 SEM-EDS

Deep etching was crucial for gaining better insight into the effects of homogenization on the morphological evolution of IMPs. Figure 4.21a-c illustrates the changes observed on skeletal morphology after different heat treatments: (a) HT1, (b) HT2 and (c) HT5. After HT1, the skeletal structure shows signs of breaking down. The main stem became thinner, and the branches appear to fragment from the stem. In contrast, longer duration (HT2) and high-temperature (HT5) homogenization treatments led to complete disintegration of the skeletal structure. The resulting morphologies varied from spherical, plate-like, rod-like shapes to irregular shapes.
The evolution of needle- and plate-shaped structures is presented in Figure 4.21d-f. After HT1, both needle- and plate-shaped morphologies remained unchanged. With prolonged heating (HT2), these morphologies became uneven with small bumps. At high-temperature homogenization (HT5), these morphologies are observed to undergo further transformation, becoming coarser and spheroidal. However, some traces of needle-shaped IMP were still observed after homogenization.

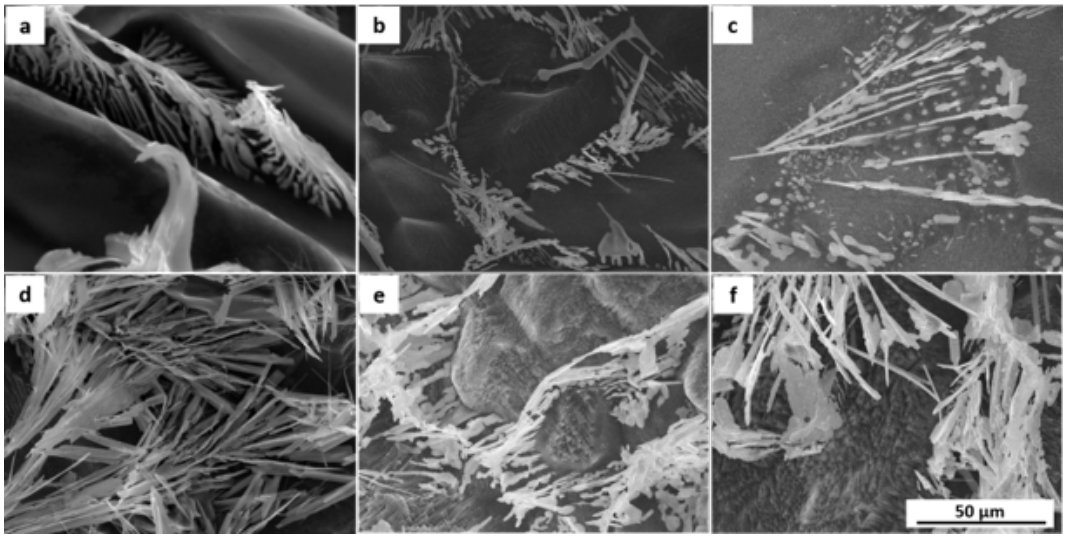

Figure 4.21: Homogenization effects on skeletal morphology after (a)AC, (b)HT2 and (c)HT5 and on nedle- and plate-like morphologies after (d) AC, (e)HT2 and (f) HT5.

Upon homogenization, the resulting morphologies were indistinctive in 3D view, thus challenging to selectively characterise quantitatively without a clear characteristic morphology by SEM-EDS. This is shown in Figure 4.22a which represents prior skeletal and Figure 4.22b showing prior needle- and plate-shaped morphologies. However, through qualitative analysis of EDS mapping, these IMPs retain the same type of elements, which are Al, Fe, and traces of Si.

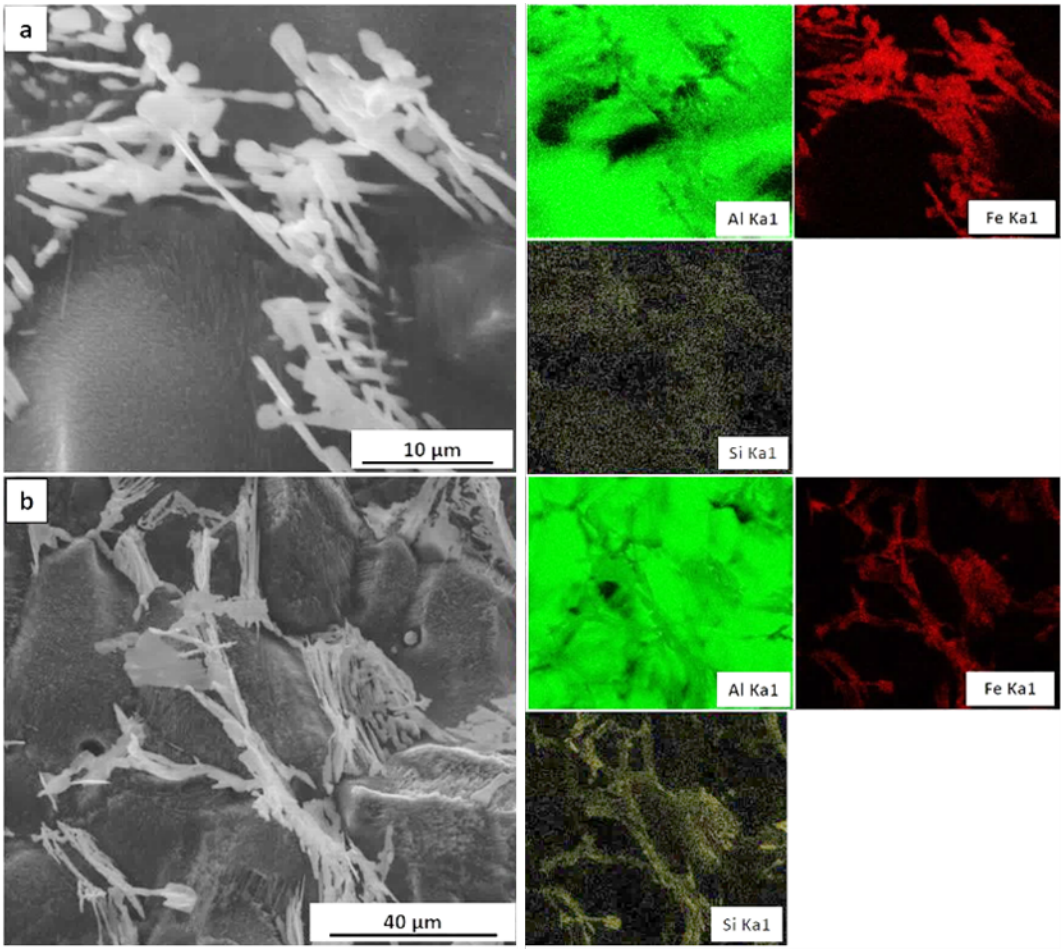

Figure 4.22: SEM-EDS mapping on prior skeletal (a) and needle- and plate-shaped morphologies after homogenization.

4.3.3 XRD characterization

Tables 4.6 and 4.7 summarizes the phases found in the AA8021 before and after various homogenization treatments. The surface sample of AA8021 showed the presence of Al_mFe after HT1 homogenization treatment, which soon transformed completely after HT2. After any of the high temperature homogenization treatments (HT3, HT4 and HT5), this phase was absent. The only phases present were Al_6Fe and Al_3Fe.

The phase distributions observed in AA8079, across the ingot after various homogenization treatments, are summarized in Tables 4.8 and 4.9. This alloy displayed a deviation from the observation made in AA8021 in that Al_mFe was absent from all the samples in different processing conditions, regardless of the region on the ingot. This left the two phases: Al_6Fe and Al_3Fe, prevalent after as-cast and after each homogenization treatment.

Table 4.6: IMP phases identified from the surface of AA8021 samples after various homogenization treatments, using XRD

	AC	HT1	HT2	HT3	HT4	HT5
Al_mFe	✓	✓	✗	✗	✗	✗
Al_6Fe	✓	✓	✓	✓	✓	✓
Al_3Fe	✓	✓	✓	✓	✓	✓

Table 4.7: IMP phases identified from the centre of AA8021 samples after various homogenization treatments, using XRD

	AC	HT1	HT2	HT3	HT4	HT5
Al_mFe	✗	✗	✗	✗	✗	✗
Al_6Fe	✓	✓	✓	✓	✓	✓
Al_3Fe	✓	✓	✓	✓	✓	✓

Table 4.8: IMP phases identified from the surface of AA8079 samples after various homogenization treatments, using XRD

	AC	HT1	HT2	HT3	HT4	HT5
Al_mFe	✗	✗	✗	✗	✗	✗
Al_6Fe	✓	✓	✓	✓	✓	✓
Al_3Fe	✓	✓	✓	✓	✓	✓

Table 4.9: IMP phases identified from the centre of AA8079 samples after various homogenization treatments, using XRD

	AC	HT1	HT2	HT3	HT4	HT5
Al_mFe	✗	✗	✗	✗	✗	✗
Al_6Fe	✓	✓	✓	✓	✓	✓
Al_3Fe	✓	✓	✓	✓	✓	✓

4.3.4 Volume fraction quantification

Figure 4.23a and Figure 4.23b, illustrate the effects of varying homogenization practices on the IMP volume fractions across the ingot regions: surface and centre, in AA8021 and AA8079, respectively. Figure 4.23a shows that there is no general trend common across the two different regions of AA8021 alloy, but notably, the surface experiences a drop in IMP volume fraction upon homogenization, while the volume fraction of IMPs increases slightly at the centre region. HT4 appears to achieve an even distribution of volume fraction across the ingot. On the other hand, the volume fraction in AA8079 generally decreases regardless of the ingot region after homogenization (Figure 4.23b). Neither the homogenization temperature nor the soak time seem to be correlated to the recorded volume fraction. As with homogenization in AA8021, there is one homogenization practice that yields an even distribution of IMPs in the ingot, except that in AA8079, the homogenization practice occurs during HT5.

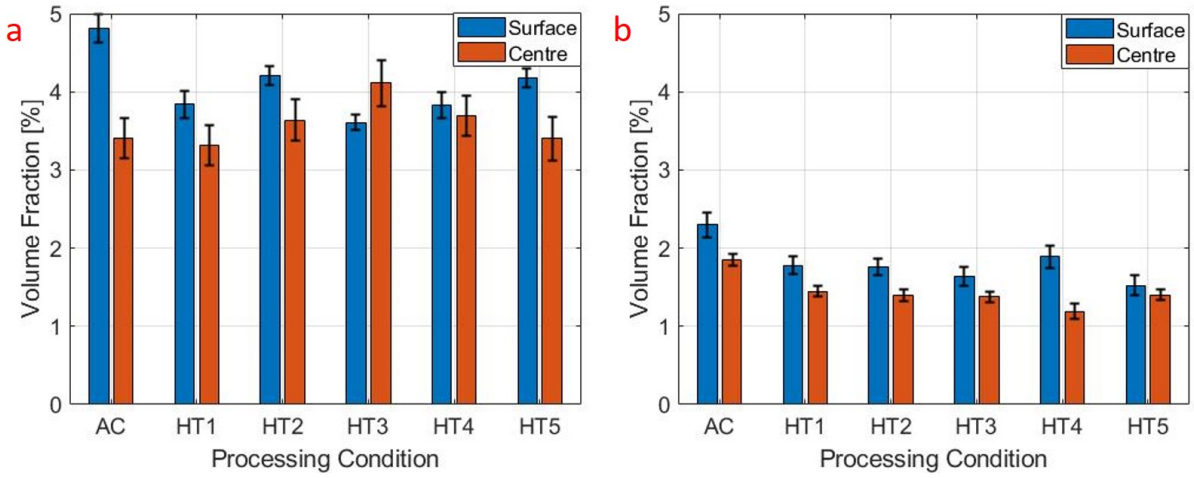

Figure 4.23: IMP Volume fractions in AA8021 before and after various homogenization treatments.

5.Discussion

The AA8xxx series aluminum alloys comprises of various chemical composition systems, each defined by different principal alloying elements. One such system is the Al-Fe-Si alloy, which has Fe and Si as its principal alloying elements. It is well established that the alloying elements significantly influence the evolution of the intermetallic particle (IMP) microstructure, including the phase type, size, morphology, volume fraction, and distribution of IMPs. In addition to alloy composition, factors such casting practice, specifically the cooling rate during solidification, and the homogenization treatment play important roles in shaping the IMP microstructure.

While the impact of these factors on the IMP microstructure is well-documented for other aluminum alloys, the AA8xxx series alloys are relatively new, and there is limited understanding of how they respond to these factors. This gap in knowledge has motivated further research to better understand their behavior.

To address the research question concerning the influence of alloying elements, cooling rate, and homogenization treatment on the IMP microstructure, experiments were conducted on two different alloys distinguished by their varying Fe and Si contents. The study then explored the regions within these alloys where the DC cast ingot experiences varying cooling rates, and compared the as-cast IMP microstructure to that after different homogenization treatments.

Based on the results presented in the preceding chapter, it was observed that the intermetallic particles formed within these alloys are very thin and create a network that constitutes less than 5% of the alloy. This made it challenging to examine the microstructure conclusively using isolated traditional techniques. As a result, a combination of traditional and advanced characterization techniques was employed to effectively assess the influence of these factors on the IMP microstructure. The techniques used included:

- light microscopy on as-polished surface.
- SEM-EDS on as-polished and deep etched samples.
- HAADF-STEM with EDS on extracted particles/powder.
- Powder X-Ray Diffraction (XRD).

5.1 Thermodynamic Phase Predictions and Deviations in AA8021 and AA8079 Alloys

Prior to conducting laboratory experiments, ICP analysis was performed on the AA8021 and AA8079 aluminum alloys. The results revealed that AA8021 has a contains higher Fe content and lower Si when compared to AA8079, which has relatively lower Fe and higher Si. Thermodynamic calculations performed using JMatPro based on these ICP results, indicated the phases to be expected in these alloys. It predicted that Al_3Fe would be the dominant phase in both alloys, with Al_6Mn, $Al_{15}(Fe,Mn)_3Si_2$ and Al_5FeSi present in trace amounts. Interestingly, the calculation for AA8079 indicated that an increase in Si results in a higher volume fraction of Si-containing phases, without increasing the overall volume fraction of the IMPs. This may suggest that the Si increment imposed in AA8079 is not large enough to drive increased precipitation of IMPs because Si is more soluble is aluminium matrix and more soluble in these stable phases. Additionally, because while Si is increased, Fe is simultaneously decreased, which may be working together.

However, these theoretical predictions contradicted the experimentally observed results, which contained metastable phases such as Al_mFe and Al_6Fe but lacked the predicted equilibrium phases, such as Al_6Mn, $Al_{15}(Fe,Mn)_3Si_2$ and Al_5FeSi. This discrepancy is due to the transformation kinetics prediction under equilibrium cooling conditions (< 0.015 K/s). DC casting experiences non-equilibrium cooling (ranging from 1-20 K/s), especially at the surface. Thermodynamic calculations assume equilibrium cooling/heating, in which the atoms of the alloying elements have enough time to diffuse and arrange themselves to the lowest energy possible, thus forming phases that are stable in the temperature under consideration. This however, is not the case in practice. Cooling and heating is never considered to be in equilibrium, hence the deviation between the predicted vs the observed IMP phases [50]. Section 5.2 and section 5.3 discusses these effects in detail. Despite the deviations in predicted phases, thermodynamic calculations were useful in narrowing down the expected and unexpected phases for analysis of XRD, SEM, and STEM results.

5.2 The effect of chemical composition on the IMP microstructure

To interrogate the effect of the compositional variation between the investigated alloys, notably the Fe and Si compositions, the IMP microstructures of the AA8079 and AA8021 were analysed and compared before homogenization, with both samples being from regions with equivalent cooling rates. Figure 5.1 illustrates a summary of the results from the light microscopy investigation. Light microscopy revealed differences in the morphology, size, and volume fraction of IMPs in each alloy. AA8021 exhibited a finer particle distribution with a higher volume fraction (4.81%) of IMPs, predominantly in skeletal morphology and small fraction of needle-shaped morphology. In contrast, AA8079 displayed a coarser and less dense distribution of IMPs, with a mixture of needle- and plate-shaped morphologies and a smaller volume fraction (2.4%).

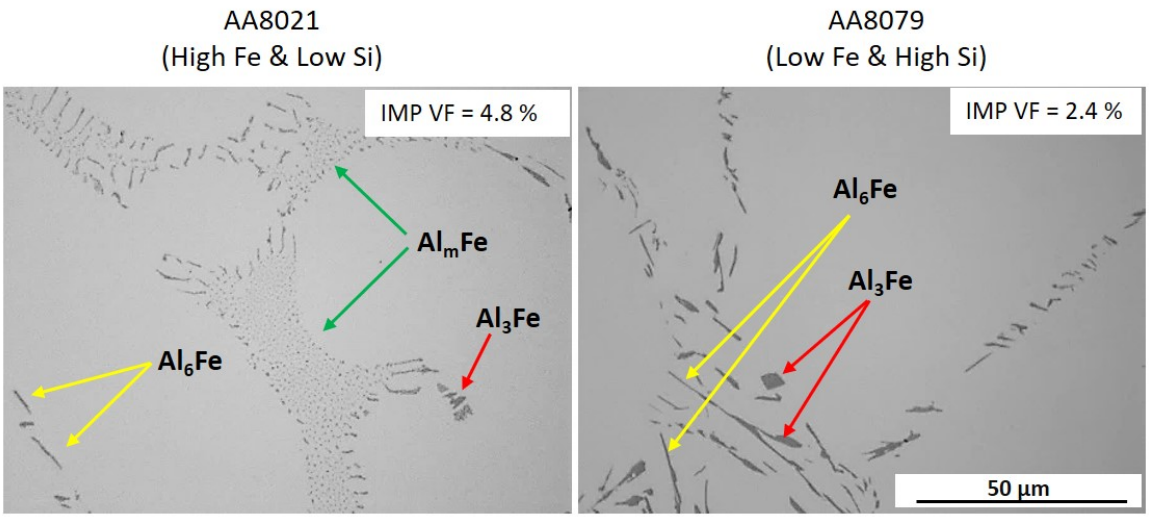

Figure 5.1: Effects of varying Fe and Si chemical composition on the IMP microstructure.

Through research, it has been demonstrated that upon solidification, IMPs tend to morphologies that are characteristic to phases [67], [50]. These findings could potentially be used for phase identification when analyzing the IMP microstructure. However, 2D morphology only represents a view from a single plane, making it possible for different IMP phases to appear similar in shape in 2D and a completely different morphology in 3D. For this reason, light microscopy was only effective for comparing the microstructures of the two alloys in terms of size, distribution, and volume fraction.

In an effort to identify the IMP phases in the alloys, initial SEM-EDS analysis was performed on as-polished samples to obtain both qualitative and quantitative chemical compositions. However, the results from the SEM-EDS mapping and spot analysis data proved inconclusive for the finer or smaller IMPs. This was due to the electron beam's interaction volume overlapping with the matrix, leading to overestimation of the Al content while suppressing the Fe and Si signals. As a result, the Al:Fe data from these techniques were unreliable for quantitative analysis, highlighting the limitations of traditional methods when dealing with fine-scale features. Despite these initial challenges, the SEM-EDS line scans provided valuable insights. The analysis revealed that the IMPs in both alloys were Fe-rich, containing significantly more Fe than the surrounding matrix, combined with aluminum and trace amounts of Si. This suggested that the IMPs were predominantly binary, with Si playing a minimal role, despite its presence. This finding supports the observations made by [50], who noted that while Fe-rich IMPs are typically binary, they tend to absorb limited amounts of Si—albeit in varying quantities depending on the phase formed.

To further refine these observations, SEM-EDS analysis was repeated on deep-etched samples. This approach helped to overcome some of the issues associated with matrix interference, providing clearer results. The analysis confirmed the presence of Al, Fe, and Si in the IMPs, and the 3D imaging revealed the three distinct morphologies initially suggested by the light micrographs. Notably, the skeletal morphology observed in 2D was actually more accurately

described as a feathery structure, consistent with previous findings reported by [23]. The subsequent SEM-EDS spot analysis of the different morphologies yielded more reliable results. With reduced interference from the matrix, the trace amounts of Si that were initially undetected were now observable. The resulting Al:Fe ratios for the different morphologies confirmed the identification of the Al_3Fe, Al_mFe and Al_6Fe corresponding to the plate-shaped, skeletal, and needle-shaped morphologies, respectively. Given concerns about topographic effects on the SEM-EDS results, complementary techniques—such as STEM-EDS and powder XRD—were employed. These additional methods qualitatively corroborated the findings, further supporting the identification of the phases and the observed microstructural differences between the alloys.

The combination of these powerful techniques revealed that in terms of phase distribution, AA8021 (with high Fe and low Si content) contains all three phases—Al_3Fe, Al_mFe and Al_6Fe, with Al_mFe being the dominant phase. In contrast, AA8079 (with low Fe and high Si content) contained only two phases (Al_6Fe and Al_3Fe), with a more balanced distribution of these phases. According to [50], [23], an increase in Si should favor the formation of Al_mFe over Al_6Fe, as Al_mFe is better able to absorb and accommodate more Si. However, this prediction is contrary to the findings of this study, where despite the increase in Si content in AA8079, Al_6Fe formation is more prevalent than Al_mFe. This discrepancy may be explained by the accompanying reduction in Fe content in AA8079. Dutta and Rettenmayr suggested that the relative amounts of Fe:Si in the eutectic liquid during solidification is a key factor in phase formation. A lower Fe:Si (approximately equal to one) ratio tends to favor the formation of Al_mFe, while higher and intermediate ratios tend to favor the formation of both Al_6Fe and Al_3Fe respectively [4]. Therefore, any alteration in the chemical composition of Fe and Si influences this ratio, ultimately affecting the resulting IMP phases.

Additionally, the fine size and high volume fraction of IMPs observed in AA8021, compared to AA8079, can be understood by considering the limited solid solubility of Fe in Al. This limitation forces the Fe to segregate out of the Al matrix, facilitating the formation of IMPs, because there is more Fe available for the transformation. Therefore, the more Fe there is, the higher the volume fraction. content increases, so does the volume fraction of IMPs, because there's more Fe to precipitate.Moreover, the addition of Fe in Al is known to refine the grains, as evidenced in the results by [3] illustrated in the micrographs in Figure 5.2. Consequently, the resulting IMPs are expected to be finer, as these IMPs form within the inter-dendrite arm spaces during solidification.

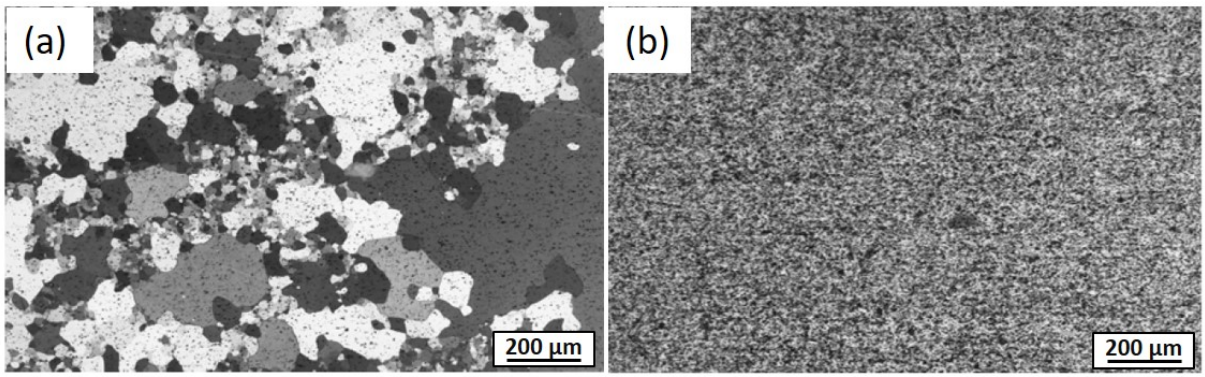

Figure 5.2: Effect of Fe content on grain size in AA1050 (a) and AA8021 (b) [3].

5.3 The role of cooling rate in shaping the IMP microstructure

Figure 5.3 summarizes the observations made for each alloy across two regions: the surface, where the cooling rate is high, and the center, where the cooling rate is lower. While the exact cooling rates were not measured in this study, they were inferred based on previous studies of DC-cast alloys [45]. The most prominent changes observed as a result of the varying cooling rates were in the volume fraction, morphology, and particle sizes of the IMPs.

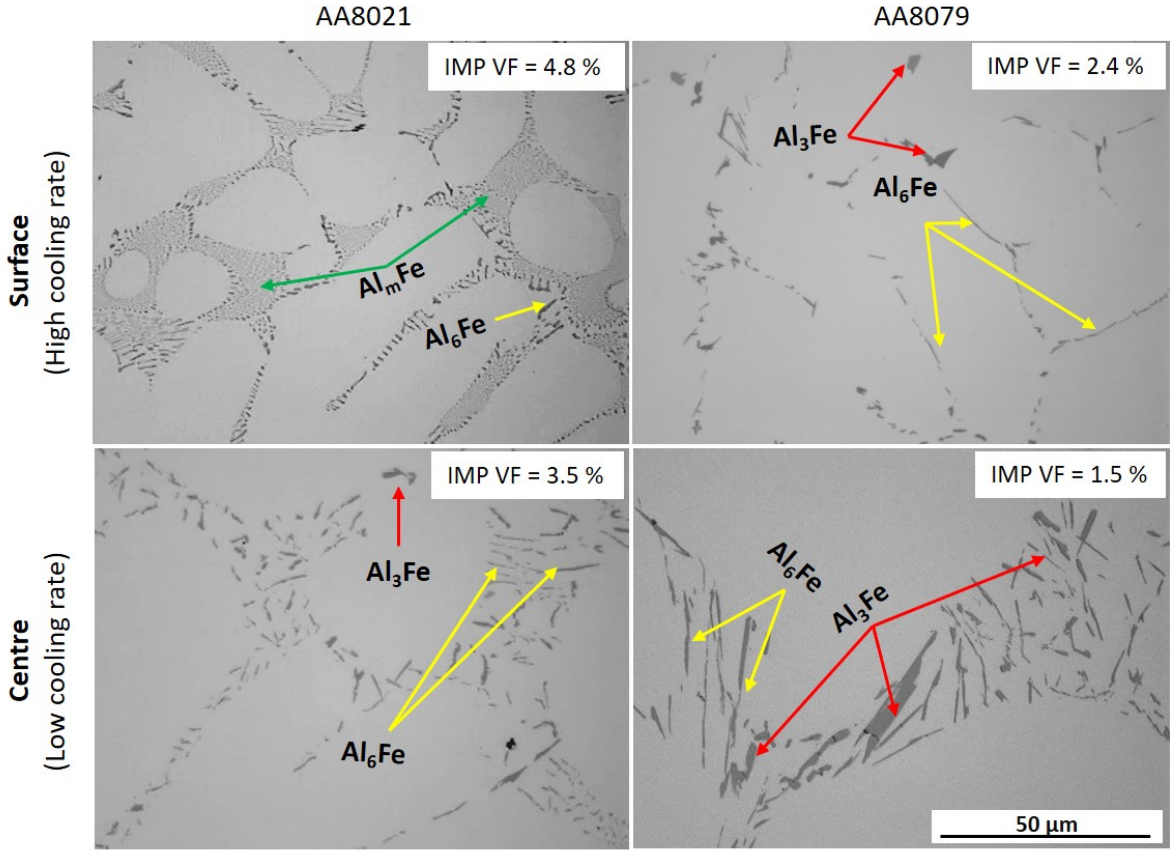

Figure 5.3: Effects of varying cooling rates on the IMP microstructure

In both alloys, a decrease in cooling rate from the surface to the center led to a drop in the volume fraction of IMPs, along with an increase in their size. At higher cooling rates, the alloying elements (Fe and Si) do not have enough time to diffuse and distribute evenly throughout the aluminum matrix. This results in a larger proportion of supersaturated liquid regions, which promotes the formation of intermetallic particles [23], [50]. The refinement of IMPs at higher cooling rates is associated with a decrease in DAS, because IMPs form in the spaces between the dendrites. At high cooling rates solidification is nucleation-driven, where multiple small nuclei form and speed up the solidification, in contrast to slower cooling rates,

where fewer nuclei grow into larger dendrites. As a result, the IMPs in regions that cooled rapidly are finer and more evenly distributed. In contrast, those in regions that cooled slowly are larger and more sparsely distributed [4], [23].

For AA8021, the surface region predominantly contains skeletal morphologies of IMPs, with minor amounts of needle- and plate-shaped particles, which correspond to the Al_mFe,Al_6Fe and Al_mFe phases, respectively. In the center, a mixture of needle- and plate-shaped morphologies were observed, with the needle-shaped morphology being dominant. For AA8079, the surface region mainly exhibited needle-shaped morphologies, with a smaller quantity of plate-shaped morphologies. The center, however, contains a mixture of these two with improved plate-shaped quantity. The cooling rate imposed on these alloys during solidification has a marked influence on the local microchemistry (Fe:Si) across the different regions of the ingot, hence the formation of distinct phases in different regions. According to allen et al [23] and previous researchers listed in Table 5.1 below, cooling rates greater than 10 K/sec favor the formation of the metastable Al_mFe phase, while cooling rates between 1-10 K/sec are ideal for the formation of the metastable Al_6Fe phase, and cooling rates less than 1 K/sec are more conducive to the formation of the stable Al_3Fe phase.

Table 5.1: Cooling rate eanges of formation of the common IMPs in hypoeutectic Al-Fe alloys

Phase	Cooling rate range, K s^{-1}	References
$FeAl_3$	0.1–3	Young and Clyne [113], Kosuge [58], Ping et al. [80], Skjerpe [96], Brusethaug et al. [17], Evans et al. [32], Maggs et al. [68]
$FeAl_x$	0.4–5	Young and Clyne [113], Westengen [112], Skjerpe [96]
Fe_2Al_9	1–6	Simensen and Vellasamy [94], Brobak and Brusethaug [16], Griger et al. [38]
$FeAl_6$	2–11	Adam and Hogan [1], Hughes and Jones [45], Young and Clyne [113], Westengen [112], Kosuge [58], Ping et al. [80], Brusethaug et al. [17], Maggs et al. [68]
$FeAl_m$	> 11	Young and Clyne [113], Westengen [112], Kosuge [58], Ping et al [80], Brusethaug et al. [17]

5.4 IMP microstructure evolution during homogenization

Homogenization is a critical thermal treatment in the rolling of wrought aluminum, usually employed to reverse microsegregation and attain even distribution of microchemistry, such as IMP and alloying elements, across the ingot. AA8021 and AA8079 alloys showed different responses to homogenization, although some trends overlapped. Figures 5.4 and 5.5 summarize these observations below.

Both alloys exhibited a reduction in IMP volume fraction in the high-solidification-rate regions (near the surface). This reduction likely results from the dissolution of metastable phases, where alloying elements are redistributed back into the matrix, some forming dispersoids. During solidification, the high cooling rate forces these slow-diffusing elements to adopt a high-energy configuration, forming metastable IMP phases. Homogenization provides enough time for these elements to diffuse into their lowest-energy configuration within the alloy. In the center region of the ingot, AA8021 showed little to no change in the IMP volume fraction (within the error bars), while AA8079 followed a trend similar to that of the surface region. This could be due to the fact that AA8079 form mostly Al_6Fe, which upon homogenisation, dissolves, hence the decline in volume fraction. Overall, a clear relationship between homogenization temperature, treatment time, and IMP volume fraction was not established. However, homogenization appears to promote a more even distribution of IMPs across the entire ingot. This is achieved through HT4 for AA8021 and HT5 for AA8079.

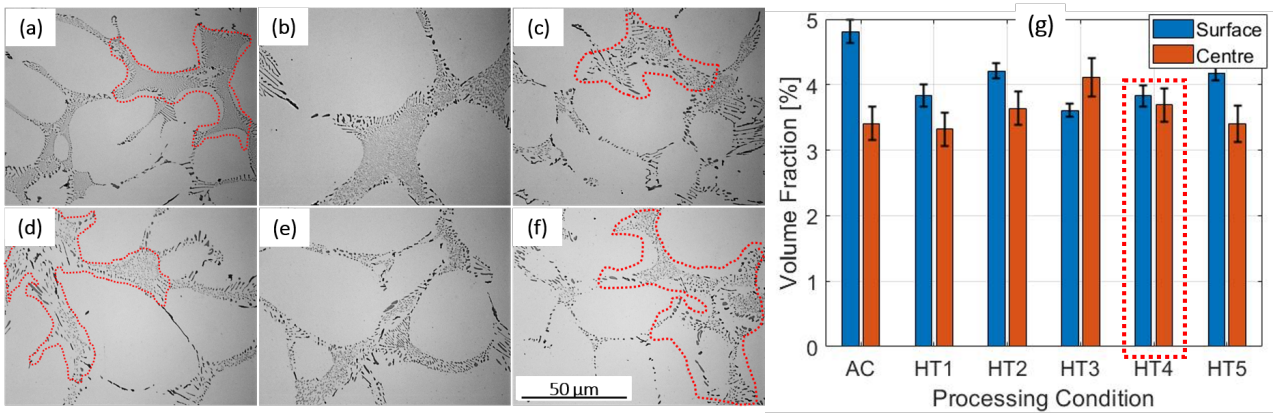

Figure 5.4: Optical micrographs showing the evolution of IMPs in the AA8021 surface (a) as-cast, followed by homogenization practices: (b) HT1, (c) HT2, (d) HT3, (e) HT4, and (f) HT5. Part (g) shows a bar graph of corresponding volume fraction changes.

Following HT1 (homogenization treatment at 500°C for 2 hours), the treatment induced fragmentation of the feathery/skeletal morphology. As both the homogenization temperature and duration increased, this morphology continued to fragment, eventually breaking down completely. Notably, the changes were difficult to observe in as-polished samples, where the morphology appeared unchanged. However, the coarsening process was evident in the decreased density of skeletal morphology branches and the increased dispersion of IMPs. Three-dimensional imaging revealed that the resulting or remnant IMPs exhibited primarily irregular

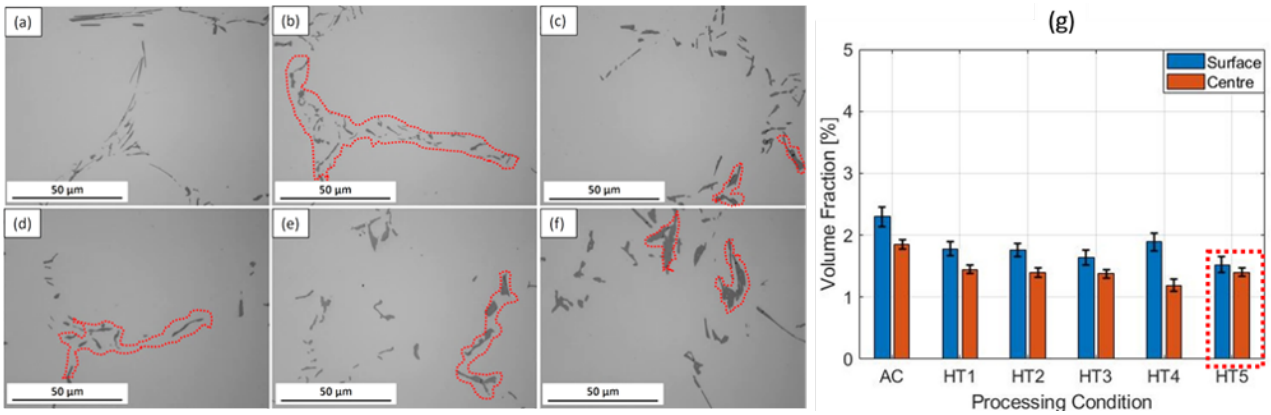

Figure 5.5: Optical micrographs showing the evolution of IMPs in the AA8079 surface (a) as-cast, followed by homogenization practices: (b) HT1, (c) HT2, (d) HT3, (e) HT4, and (f) HT5. Part (g) shows a bar graph of corresponding volume fraction changes.

shapes, with some traces of rod- and sphere-like structures, which upon inspection for chemical composition, confirmed to maintain their original elemental composition; Al and Fe with traces of Si.

In contrast to the fragmentation observed in skeletal structures, needle- and plate-shaped IMPs began to spheroidize and become bulkier, but this change only occurred after HT2 (homogenization at 500°C for 20 hours). This difference underscores the stability of Al_6Fe over Al_mFe. Both Al_6Fe and Al_mFe are metastable phases, meaning they inevitably transform into more stable phases under the right conditions, during heating. Previous studies have shown that Al_mFe is the less stable of the two, and transforms around 390°, while Al_6Fe starts its transformation at 490°. This explains the earlier breakdown of Al_mFe-linked skeletal morphologies and the delayed evolution of Al_6Fe-linked needle-shaped IMPs. Qualitative XRD analysis corroborated these findings, indicating the disappearance of Al_mFe after HT2 and the resulting existence of Al_6Fe and Al_3Fe. It is not well understood why Al_6Fe, as a metastable phase is still present after long duration and high temperature homogenisation practice. It could be that the long duration HT2 is inefficient because this phase starts to transform at 490°C, which the more time is required for HT3, HT4 and HT5.

6.Conclusions

This study focused on investigating the influence of chemical composition and cooling rate on the IMP microstructure and how this microstructure evolves after imposing varying homogenisation practices, which are mandatory in the fabrication process of DC cast aluminium alloys. In this study, the context of IMP microstructure refers to the volume fraction, particle sise, phase type, morphology and their distribution. Two different experimental approches: two-dimensional (2D) and three-dimensional (3D) analytical techniques were successfully used to interrogate the IMP microstructure. 2D analysis was achieved through the use of analytical tools such as light and electron microscopes on flat polished specimen combined with image analysis software. 3D analysis utilized SEM, STEM and XRD on extracted and partially extracted specimen. From the observations made using these techniques and approaches, the following conclusions were drawn:

- Both 2D and 3D analysis identified and distinguished three morphologies: plate-shaped, feathery/skeletal and needle shaped, corresponding to Al_3Fe, Al_mFe and Al_6Fe phases respectively. Al_mFe and Al_6Fe are metastable phases while Al_3Fe is a stable phase. The link between morphology and phase were established through qualitative and quantitative application of SEM and STEM on extracted and partially extracted (deep etched) particles. Therefore, it has been determined that it is possible to use morphology to qualitatively infer phase proportions in as-cast condition where morphologies are characteristic to specific phases.

- AA8021, with a combination of high Fe and low Si, forms a high-volume fraction of finer IMPs with Al_3Fe, Al_mFe and Al_6Fe phases, while AA8079, containing relatively lower Fe and higher Si contents, forms low volume fraction of relatively coarse IMPs dominated by needle- and plate-shaped morphologies, corresponding to Al_6Fe and Al_3Fe. Therefore, the higher the Fe content, the higher the number of IMPs and the more refined they are. Additionally, an in increased Si in AA8079 content improved stability of Al_3Fe, thus the Al_mFe phase in AA8079 was not detected, even at high cooling rate region (surface).

- Higher cooling rates at the surface of the ingot, irrespective of the chemical composition, lead to a relatively higher volume fraction of IMPs that are finer in size while a lower cooling rate at the centre causes the formation of low volume fraction of coarser IMPs. Additionally, the high cooling rate on the surface is ideal for the formation of metastable phases. AA8021 is dominated by Al_mFe and Al_6Fe phases at the surface and a combination of Al_6Fe and Al_3Fe at the centre. In contrast, AA8079 contains a combination of Al_6Fe and Al_3Fe at the surface and a mixture of Al_6Fe and Al_3Fe at the centre.

- Homogenisation practices induce the phase transformation of metsastable phases (Al_6Fe and Al_mFe) to stable Al_3Fe phase.This occurs through the dissolution and reprecipitation of Fe and Si. As a result, the volume fraction decreases because some dissolving elements form dispersoids or dissolve into the matrix. The dissolution of metastable phases is followed by spheroidization and coarsening as the stable phase reprecipitates and grows.

The microstructure after homogenisation often contains a mixture of refined and coarse IMPs.

- HT4 achieves a uniform distribution of IMPs in AA8021, while HT5 achieves the same in AA8079. These heat treatments represent ideal homogenisation practices that eliminate microsegregation. However, in AA8021, which predominantly contains a metastable phase, extensive IMP refinement was observed. Additionally, the high Fe content acts as a grain refiner, enhancing strength. Collectively, these observations highlight the effectiveness of AA8021 homogenized HT4.

7.Recommendations

The findings and conclusions presented in the previous chapters of this thesis shed light on the limitations of this study. Therefore, the following recommendations have been made to address these limitations and challenges encountered, to influence future research for improved interrogation and understanding of factors affecting the evolution of IMPs in the AA8XXX series aluminium allloys for better alloy processing.

- ICP analysis revealed that neither of the two principal alloying elements (Fe and Si) are controlled (kept constant) when interrogating the influence of each on the IMP microstructure. To gain a deeper understanding of the individual roles of Fe and Si in influencing the IMP microstructure, future studies should focus on alloys with a constant Fe content while varying Si levels, and vice versa. This would allow for a more controlled investigation of the effects of each alloying element on IMP formation, enabling clearer insights into their individual contributions.

- Due to the similarity in chemical compositions and limited crystallographic data for some Al-Fe-based IMPs, such as Al_mFe, accurately distinguishing them remains challenging. Further research is needed to improve the crystallographic database of these phases for more efficient and convenient identification .

- The volume fraction method used in this study is based on converting area fraction to volume fraction using a specific equation. Matrix dissolution using phenol is fast and efficient with zero loss of IMPs during extraction, thus a more accurate approach for quantifying volume fraction could involve submerging the extracted IMP powder in liquid and measuring the volume change to determine the IMP volume.

References

[1] V. P. Deshmukh, S. S. Patil, P. R. Shewale, and B. Vidyapeeth, *A study on the thermal characteristics of lithium ion battery for electric vehicles*, 2021. [Online]. Available: http://ijmer.in.doi./2021/10.08.06.

[2] P. Zhu, D. Gastol, J. Marshall, R. Sommerville, V. Goodship, and E. Kendrick, "A review of current collectors for lithium-ion batteries," *Journal of Power Sources*, vol. 485, p. 229 321, 2021.

[3] J. Hasenclever, "Microstructure and properties of alfe-alloys(aa 1050- aa 8021) for packaging," in *Materials Forum*, vol. 28, 2004, pp. 867–872.

[4] B. Dutta and M. Rettenmayr, "Effect of cooling rate on the solidification behaviour of al–fe–si alloys," *Materials Science and Engineering: A*, vol. 283, no. 1-2, pp. 218–224, 2000.

[5] I. Polmear, D. StJohn, J.-F. Nie, and M. Qian, *Light alloys: metallurgy of the light metals*. Butterworth-Heinemann, 2017.

[6] K. Georgitzikis, L. Mancini, E. d'Elia, and B. Vidal Legaz, *Sustainability aspects of bauxite and aluminium*, 2021.

[7] J. R. Davis, *Asm Specialty Handbook: Aluminum & Aluminum Alloys*. ASM international, 1993.

[8] Y. Zhang, Y. Qi, and J. Li, "Aluminum mineral processing and metallurgy: Iron-rich bauxite and bayer red muds," in *Aluminium Alloys and Composites*, K. O. Cooke, Ed., Rijeka: IntechOpen, 2018, ch. 2. DOI: 10.5772/intechopen.78789. [Online]. Available: https://doi.org/10.5772/intechopen.78789.

[9] *Tensile strength of pure aluminium - google search*, https://www.google.com/search?q=tensile+strength+of+pure+aluminium, (Accessed on 01/10/2024).

[10] *Tensile strength of light alloys - google search*, https://www.google.com/search?q=TENSILE+STRENGTH+OF+LIGHT+ALLOYS, (Accessed on 01/10/2024).

[11] A. K. Vasudevan and R. D. Doherty, *Aluminum alloys–contemporary research and applications: Contemporary research and applications*. Elsevier, 2012.

[12] J. R. Davis *et al.*, *Aluminum and aluminum alloys*. ASM international, 1993.

[13] E. Georgantzia, M. Gkantou, and G. S. Kamaris, "Aluminium alloys as structural material: A review of research," *Engineering Structures*, vol. 227, p. 111 372, 2021.

[14] O. S. I. Fayomi, A. P. I. Popoola, and N. E. Udoye, "Effect of alloying element on the integrity and functionality of aluminium-based alloy," *Aluminium alloys-recent trends in processing, characterization, mechanical behavior and applications*, pp. 243–262, 2017.

[15] T. Srivatsan and T. A. Place, "Microstructure, tensile properties and fracture behaviour of an al-cu-li-mg-zr alloy 8090," *Journal of materials science*, vol. 24, pp. 1543–1551, 1989.

[16] I. Jin, K. Gatenby, C. Gabryel, T. Anami, T. Watai, and I. Okamoto, *Production of aluminum alloy foils having high strength and good rollability*, US Patent 6,663,729, Dec. 2003.

[17] L. ZHANG, K. Xiaoshu, and B. ZHONG, "Effects of si content on microstructure and mechanical properties of 8079 aluminum alloy," *Research and Application of Materials Science*, vol. 2, no. 1, 2020.

[18] K. Delijić, V. Asanović, and D. Radonjić, "The effect of thermo-mechanical processing on the properties of some al-fe-si alloys with high fe/si ratio," in *Materials science forum*, Trans Tech Publ, vol. 555, 2007, pp. 559–563.

[19] D. EN, "573y3: Aluminium and aluminium alloys-chemical composition and form of wrought products-part 3: Chemical composition and form of products," *German version EN 573Y3*, 2013.

[20] W. Chen, P. Z. Zhao, Y. L. Zhou, and Y. F. Pan, "Effects of homogenization conditions on the microstructures of twin-roll cast foil stock of aa8021 aluminum alloy," in *Materials Science Forum*, Trans Tech Publ, vol. 877, 2017, pp. 296–302.

[21] T. Sathish, V. Mohanavel, T. Arunkumar, *et al.*, "Investigation of mechanical properties and salt spray corrosion test parameters optimization for aa8079 with reinforcement of tin+ zro2," *Materials*, vol. 14, no. 18, p. 5260, 2021.

[22] M. Shakiba, N. Parson, and X.-G. Chen, "Effect of homogenization treatment and silicon content on the microstructure and hot workability of dilute al–fe–si alloys," *Materials Science and Engineering: A*, vol. 619, pp. 180–189, 2014.

[23] C. Allen, K. O'reilly, B. Cantor, and P. Evans, "Intermetallic phase selection in 1xxx al alloys," *Progress in Materials Science*, vol. 43, no. 2, pp. 89–170, 1998.

[24] A. Garcia, P. Goulart, F. Bertelli, J. Spinelli, and N. Cheung, "Hypoeutectic al–fe alloys: Formation and characterization of intermetallics by dissolution of the al matrix," in *Encyclopedia of Aluminum and Its Alloys, Two-Volume Set (Print)*, CRC Press, 2018, pp. 1270–1286.

[25] D. V. Malakhov, D. Panahi, and M. Gallerneault, "On the formation of intermetallics in rapidly solidifying al–fe–si alloys," *Calphad*, vol. 34, no. 2, pp. 159–166, 2010.

[26] V. G. Rivlin and G. V. Raynor, "4: Critical evaluation of constitution of aluminium-iron-silicon system," *International Metals Reviews*, vol. 26, pp. 133–151, 1 Jan. 1981, ISSN: 03084590. DOI: 10.1179/imtr.1981.26.1.133.

[27] H. Tanihata, T. Sugawara, K. Matsuda, and S. Ikeno, "Effect of casting and homogenizing treatment conditions on the formation of al–fe–si intermetallic compounds in 6063 al–mg–si alloys," *Journal of Materials Science*, vol. 34, no. 6, pp. 1205–1210, 1999.

[28] V. Raghavan, "Al-fe-si (aluminum-iron-silicon)," *Journal of phase equilibria and diffusion*, vol. 30, no. 2, pp. 184–188, 2009.

[29] M. Lentz, G. Laptyeva, and O. Engler, "Characterization of second-phase particles in two aluminium foil alloys," *Journal of Alloys and Compounds*, vol. 660, pp. 276–288, 2016.

[30] R. Kumar, A. Gupta, T. R. Dandekar, and R. K. Khatirkar, "Evolution of microstructure and texture during homogenization in a strip cast aa8011 aluminum alloy," *Intermetallics*, vol. 130, p. 107 064, 2021.

[31] J. A. Taylor, "The effect of iron in al-si casting alloys," in *35th Australian foundry institute national conference*, Australian Foundry Institute (AFI) Adelaide, South Australia, vol. 31, 2004, pp. 148–157.

[32] J. Mathew, G. Remy, M. A. Williams, F. Tang, and P. Srirangam, "Effect of fe intermetallics on microstructure and properties of al-7si alloys," *Jom*, vol. 71, pp. 4362–4369, 2019.

[33] R. Rana, R. Purohit, and S. Das, "Reviews on the influences of alloying elements on the microstructure and mechanical properties of aluminum alloys and aluminum alloy composites," *International Journal of Scientific and research publications*, vol. 2, no. 6, pp. 1–7, 2012.

[34] R. G. Kamat, J. Ng-Yelim, and S. Saimoto, "Morphology and precipitation of a-al (fe, mn) si phase in hot rolled aa3004," *International Journal of Materials Research*, vol. 86, no. 1, pp. 49–53, 1995.

[35] W. Shen, A. Hu, S. Liu, and H. Hu, "Al-mn alloys for electrical applications: A review," *Journal of Alloys and Metallurgical Systems*, vol. 2, p. 100 008, 2023, ISSN: 2949-9178. DOI: https://doi.org/10.1016/j.jalmes.2023.100008. [Online]. Available: https://www.sciencedirect.com/science/article/pii/S2949917823000081.

[36] M. Dehmas, P. Weisbecker, G. Geandier, P. Archambault, and E. Aeby-Gautier, "Experimental study of phase transformations in 3003 aluminium alloys during heating by in situ high energy x-ray synchrotron radiation," *Journal of alloys and compounds*, vol. 400, no. 1-2, pp. 116–124, 2005.

[37] X. Wu, H. Zhang, F. Zhang, *et al.*, "Effect of cooling rate and co content on the formation of fe-rich intermetallics in hypoeutectic al7si0. 3mg alloy with 0.5% fe," *Materials Characterization*, vol. 139, pp. 116–124, 2018.

[38] W. Schneider, G. Laptyeva, M. Lentz, and K. F. Karhausen, "Through process microchemistry effects on the properties of 8xxx sheet," in *Materials Science Forum*, Trans Tech Publ, vol. 706, 2012, pp. 323–328.

[39] E. Santora, J. Berneder, F. Simetsberger, and M. Doberer, "Mechanical properties evolution for 8xxx foil stock materials by alloy optimization—literature review and experimental research," *Light Metals 2019*, pp. 365–372, 2019.

[40] Y. Birol, "Interannealing twin-roll cast al–fe–si strips without homogenization," *Scripta Materialia*, vol. 61, no. 2, pp. 185–188, 2009.

[41] W. Chen, M. Chen, X. Jin, and P. Zhang, "Effect of heating rate during annealing on microstructure and texture evolution of aa8021 aluminum foil," *Materials Research Express*, vol. 7, no. 9, p. 096 514, 2020.

[42] A. Verma, S. Kumar, P. Grant, and K. O'Reilly, "Influence of cooling rate on the fe intermetallic formation in an aa6063 al alloy," *Journal of Alloys and Compounds*, vol. 555, pp. 274–282, 2013.

[43] T. Materia, *Direct-chill casting - google search*, https://www.totalmateria.com/page.aspx?ID=CheckArticle&site=ktn&LN=NO&NM=384, (Accessed on 01/10/2024), 2016.

[44] A. Aliravci, "Kinetics, thermodynamics and mechanism of metastable al-almfe phase and fir-tree zone formation in dc-cast al-fe-si alloy ingots," 2006.

[45] J. Blackwell and J. Ockendon, "Exact solution of a stefan problem relevant to continuous-casting," *International Journal of Heat and Mass Transfer*, vol. 25, no. 7, 1982.

[46] S. Brusethaug, D. Porter, and O. Vorren, "The effect of process parameters on the fir-tree structure in dc-cast rolling ingots," *The 8th International Leichtmetalltagung, Leoben-Wien*, pp. 472–476, 1987.

[47] T. Kraft, M. Rettenmayr, and A. Roosz, "Undercooling effects in microsegregation modelling," *Scripta materialia*, vol. 35, no. 1, 1996.

[48] Y. Zhang, Y. Liu, Y. Han, C. Wei, and Z. Gao, "The role of cooling rate in the microstructure of al–fe–si alloy with high fe and si contents," *Journal of Alloys and Compounds*, vol. 473, no. 1-2, pp. 442–445, 2009.

[49] R. Kralik, B. KŘIVSKÁ, L. BAJTOŠOVÁ, M. ŠLAPÁKOVÁ, and M. Cieslar, "Homogenization of twin-roll cast aa8079 aluminum alloy studied by in-situ tem," *Transactions of Nonferrous Metals Society of China*, vol. 32, no. 7, pp. 2138–2149, 2022.

[50] J. Arbeiter, M. Vončina, D. Volšak, and J. Medved, "Evolution of fe-based intermetallic phases during homogenization of al–fe hypoeutectic alloy," *Journal of Thermal Analysis and Calorimetry*, vol. 142, no. 5, pp. 1693–1699, 2020.

[51] S. Patel and J. Mukhopadhyay, "Effect of homogenization on al-fe-si centerline segregation of twin-roll cast aluminum alloy aa 8011," in *Light Metals 2019*, Springer, 2019, pp. 351–355.

[52] R. Wagner, N. Preschitschek, S. Passerini, J. Leker, and M. Winter, "Current research trends and prospects among the various materials and designs used in lithium-based batteries," *Journal of Applied Electrochemistry*, vol. 43, pp. 481–496, 2013.

[53] L. E. Samuels, *Light microscopy of carbon steels*. Asm International, 1999.

[54] G. F. Vander Voort, *Metallography, principles and practice*. ASM international, 1999.

[55] H. Treating, M. Alloys, and S. Steels, "Light microscopy subject guide,"

[56] G. F. V. Voort, "Metallography and microstructures, vol 9, asm international," *Chemical and Electrolytic Polishing, Table*, vol. 3, pp. 281–293, 2004.

[57] D. C. Bell and A. J. Garratt-Reed, *Energy dispersive X-ray analysis in the electron microscope*. Garland Science, 2003, vol. 49.

[58] R. F. Egerton *et al.*, *Physical principles of electron microscopy*. Springer, 2005, vol. 56.

[59] M. Dunlap and J. Adaskaveg, "Introduction to the scanning electron microscope," *Theory, practice, & procedures. Facility for Advance Instrumentation. UC Davis*, vol. 52, 1997.

[60] VacCoat, *What is an electron microscope?* https://vaccoat.com/blog/electron-microscope/, (Accessed on 01/10/2025).

[61] W. D. Callister Jr and D. G. Rethwisch, *Materials science and engineering: an introduction*. John wiley & sons, 2020.

[62] E. E. Underwood, "Quantitative stereology for microstructural analysis," *Microstructural Analysis: Tools and Techniques*, pp. 35–66, 1973.

[63] A. Gupta, P. Marois, and D. Lloyd, "Review of the techniques for the extraction of second-phase particles from aluminum alloys," *Materials characterization*, vol. 37, no. 2-3, pp. 61–80, 1996.

[64] K. Sato and I. Izumi, "Chemical isolation of intermetallic compounds from aluminium and its alloys," *Bunseki Kagaku*, vol. 33, no. 11, E495–E498, 1984.

[65] J. Li, M. Albu, T. Ludwig, *et al.*, "Modification of eutectic si in al-si based alloys," *Materials Science Forum*, vol. 794-796, pp. 130–136, Jun. 2014. DOI: 10.4028/www.scientific.net/MSF.794-796.130.

[66] N. Saunders, "Thermotech al-data information,"

[67] Z. Que, Y. Wang, C. L. Mendis, *et al.*, "Understanding fe-containing intermetallic compounds in al alloys: An overview of recent advances from the lime research hub," *Metals*, vol. 12, no. 10, p. 1677, 2022.

[68] A. Y. Algendy, K. Liu, X. Chen, *et al.*, "Formation of intermetallic phases during solidification in al-mg-mn 5xxx alloys with various mg levels," in *MATEC Web of Conferences*, vol. 326, 2020, e02002.

Appendices

Appendix A

7.1 Appendix

1. Open ImageJ program and record macro.

   Select Plugins > Macros > Record. This opens a pop-up window that records all the procedure undertaken thereafter.

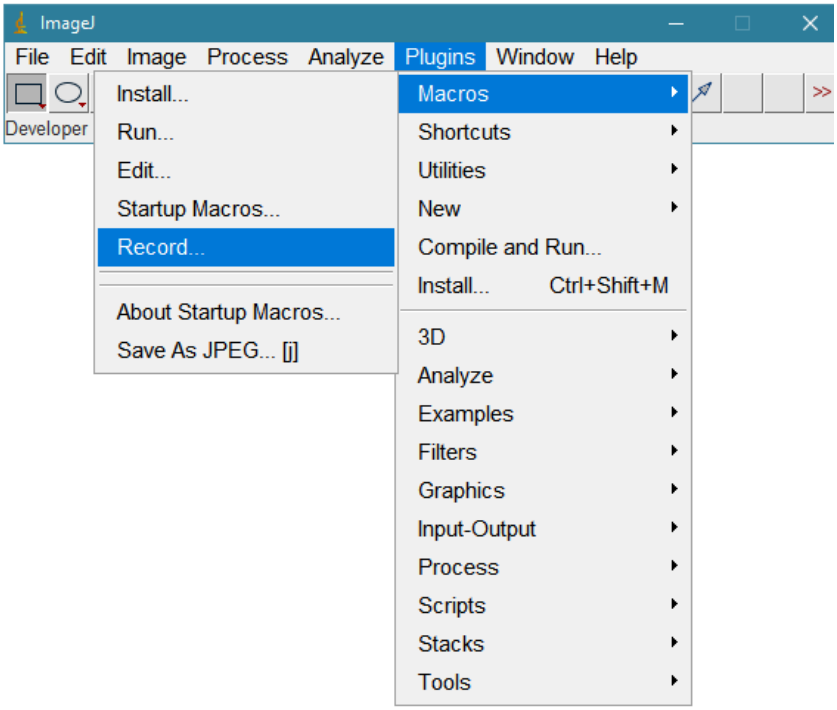

Figure 7.1: Recording macros in ImageJ for batch processing.

2. Calibrate the scale.
   Select file > Open > Select image with micron marker > Draw a line over micron marker > analyze > set-scale.
   A pop-up window Figure 7.3 opens and allows user to input the "known distance" which is equivalent to the value on the micron marker over which the line was drawn. consequently, the unit of length is μm and the distance in pixels is what the software automatically fills up after measuring the drawn line.

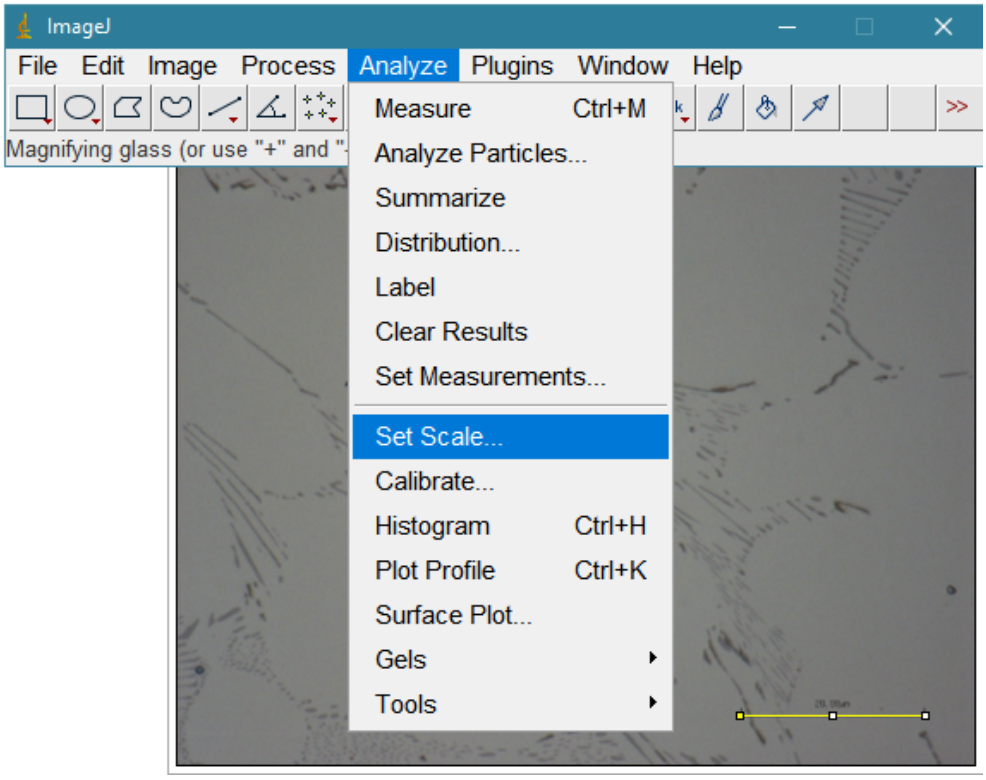

Figure 7.2: Calibration steps.

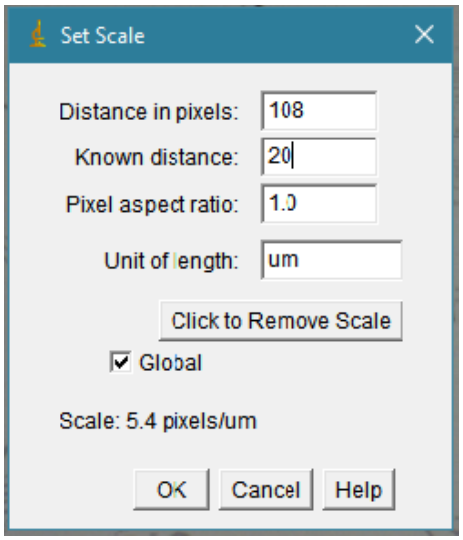

Figure 7.3: Values used for calibrating the software.

3. Set Measurements.

Select file > Open > Select image without micron marker in a directory containing all micrographs to be analyzed > Select analyze > Set measurements by ticking applicable checkboxes.

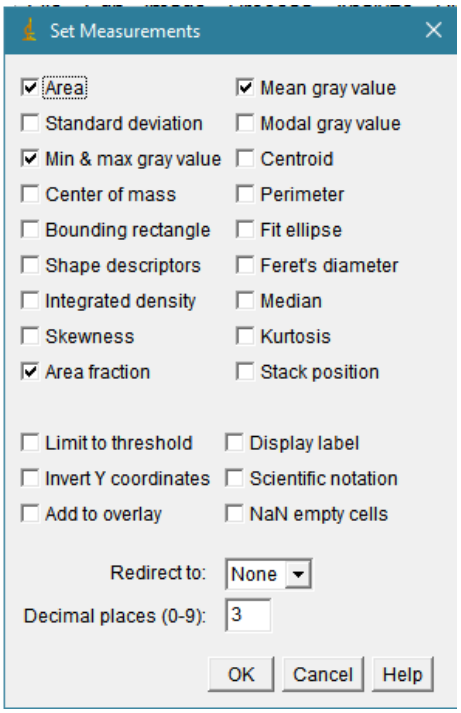

Figure 7.4: selecting measurement options.

4. Convert to Greyscale.

   Select image > type > 8-bit.

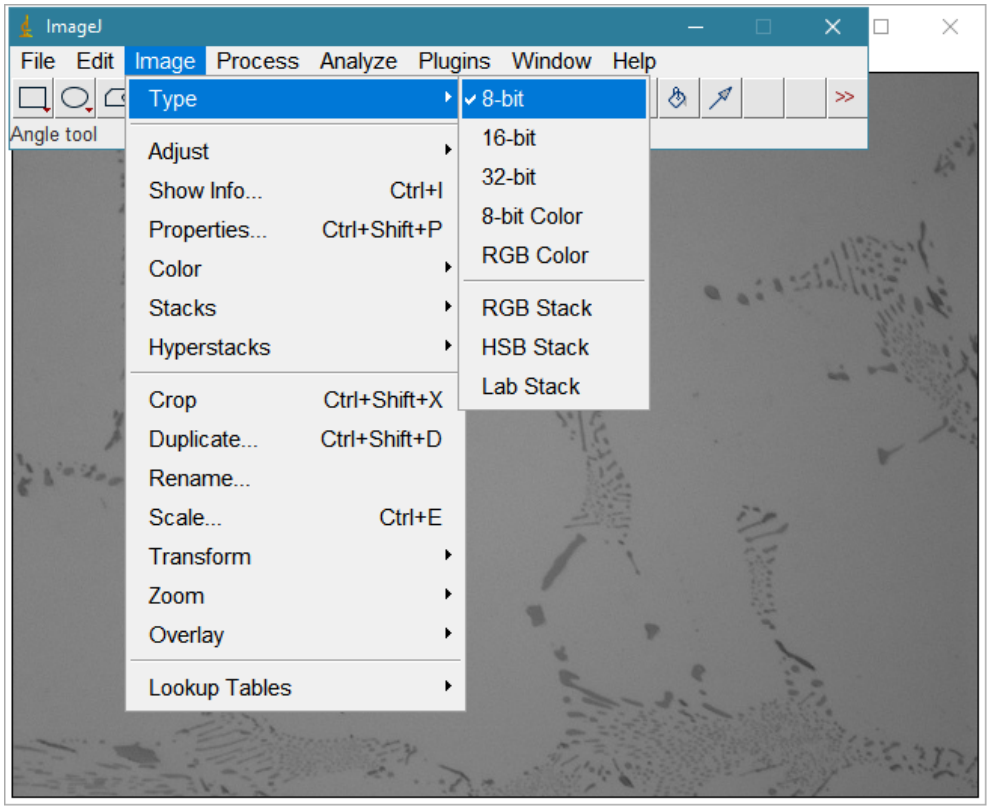

Figure 7.5: Converting the image to greyscale.

5. Threshold the image.

   Select image > adjust > threshold > use sliding button to highlight IMP > Apply.
   This functionality allows user to highlight the IMP which appear more darker relative to the light aluminium matrix. If the micrograph is unevenly illuminated, then use "background subtraction" found in the "Process" tab. Issues regarding lack of contrast were addressed using "enhance contrast" functionality found in "process" tab as well. These functionalities, where needed, were employed before thresholding.

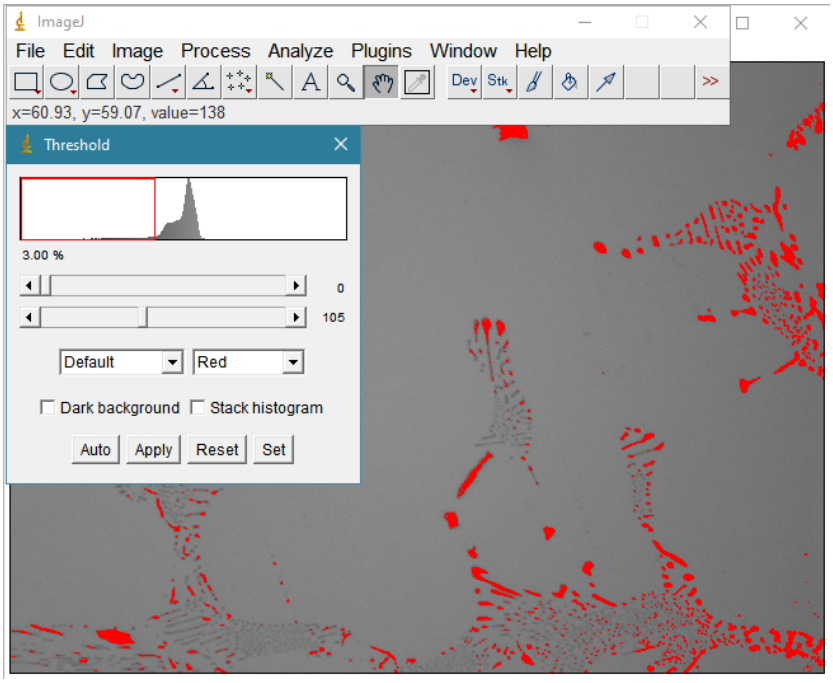

Figure 7.6: Image thresholding.

6. Analyse particles.
   Click analyze > Analyze particles > tick applicable checkboxes from pop-up window Figure 7.7 > Click "Ok".
   Analyze > Meaasure. Pop-up window appears as in Figure 7.9. The data was then copied to excel spreadsheet for further processing

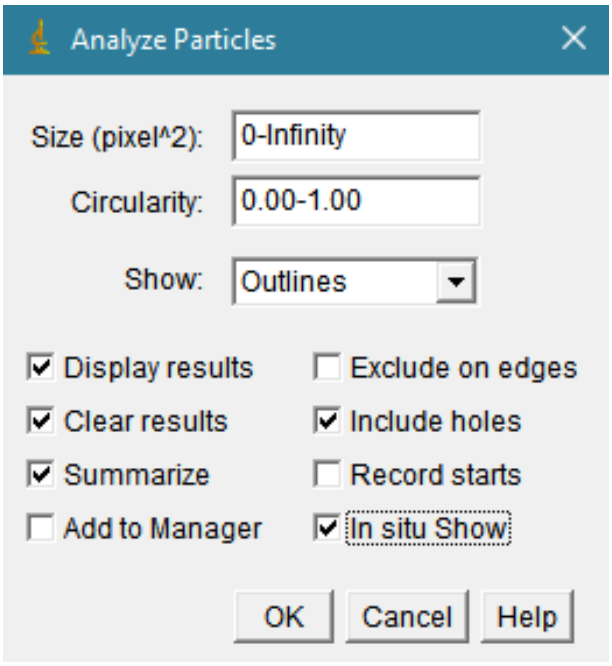

Figure 7.7: Analysing particles according to particles dimensions.

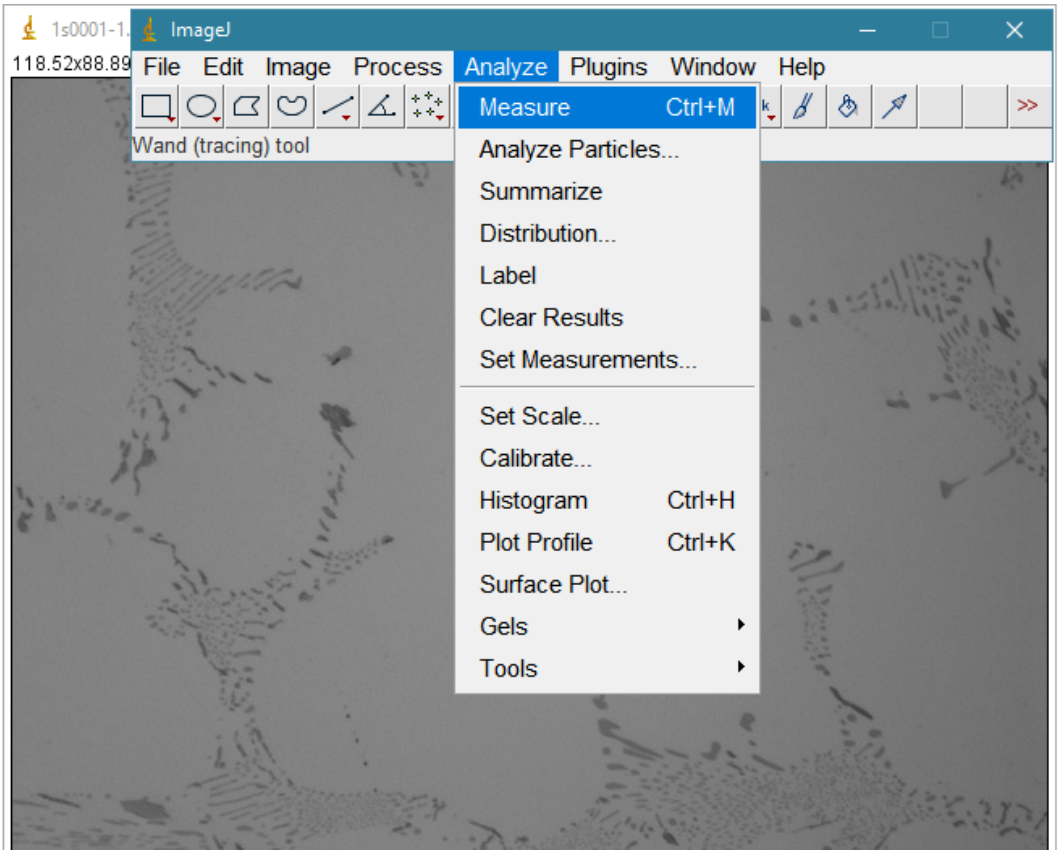

Figure 7.8: Measuring the desired values.

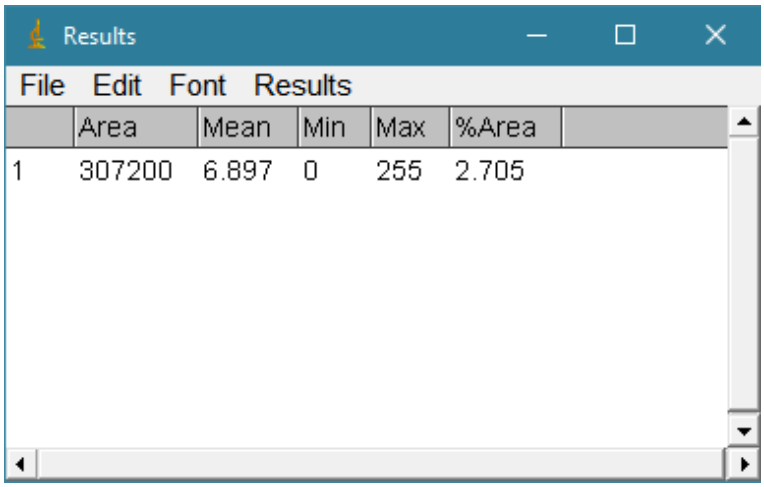

Figure 7.9: Measurement data output.

7. Run recorded macro.
   Macros > Run macro
   Open next image: File > Open Next > Re-run marco and repeat this process for all images in the directory.

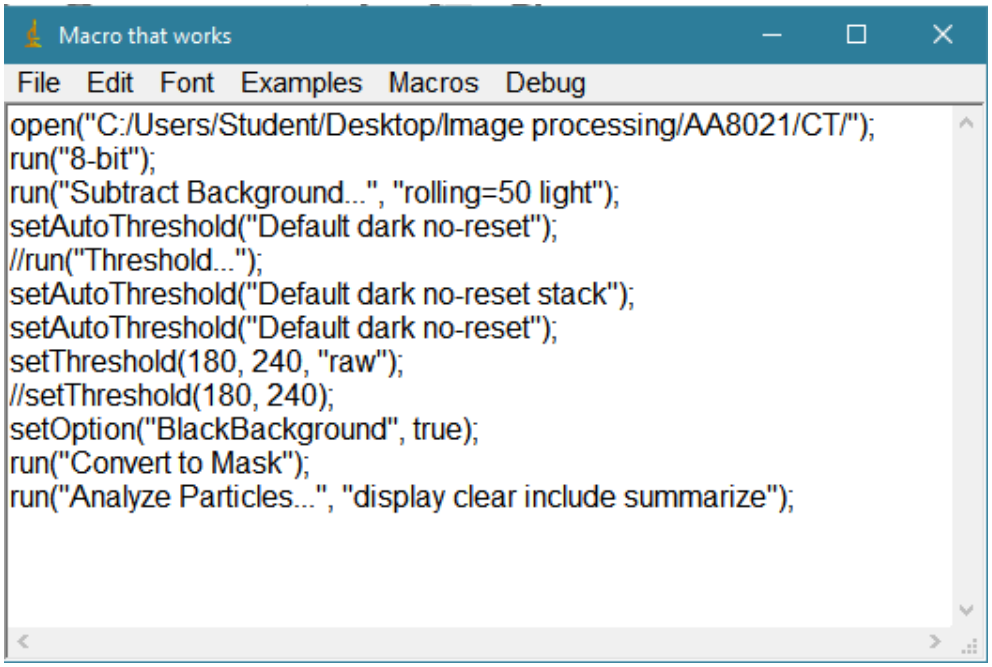

Figure 7.10: Recorded macros used for semi-automatic batch processing.

It is important to note that steps 1-3 were removed from the macro because they only needed to be calibrated once, for as long as the session is active.

Appendix B

The following figures show the evolution of the IMP microstructure of the samples exposed to different homogenization practices. The noticeable changes in IMP microstructure include size, morphology, distribution, and number density.

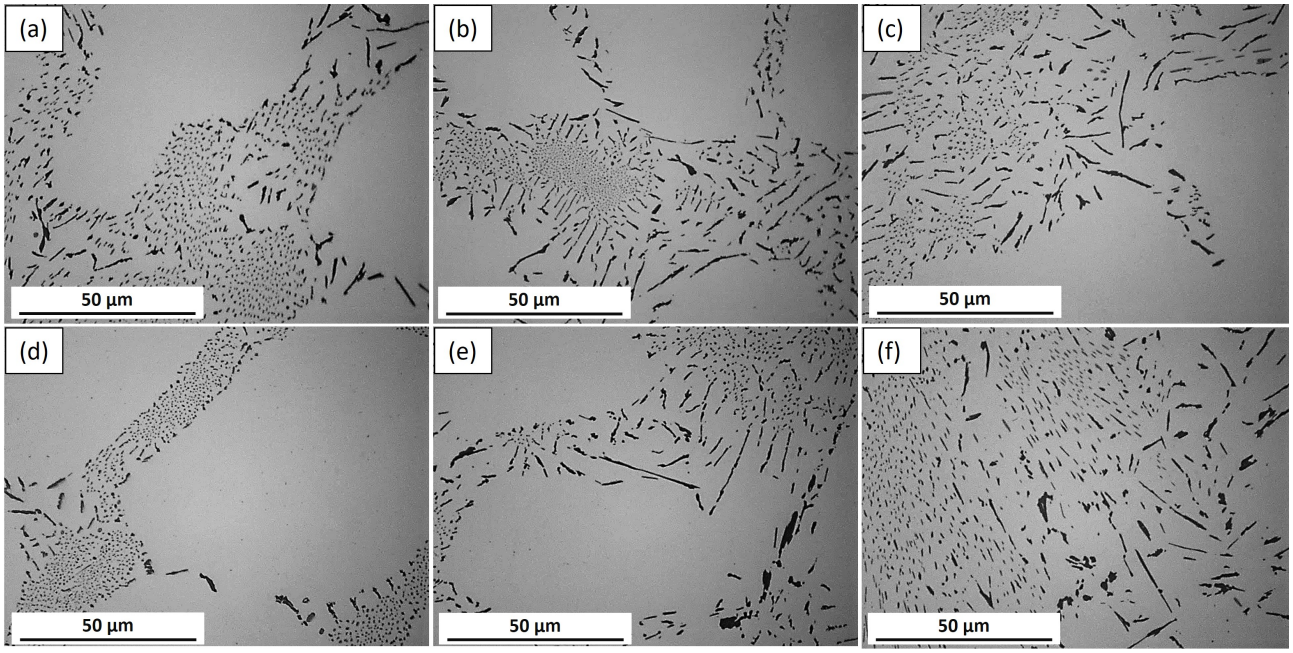

Figure 7.11: Optical micrographs showing the evolution of IMP in AA8021-CW from as-cast (a) through different homogenization treatments: (b) HT1, (c) HT, (d) HT3, (e) HT4, and (f) HT5.

.

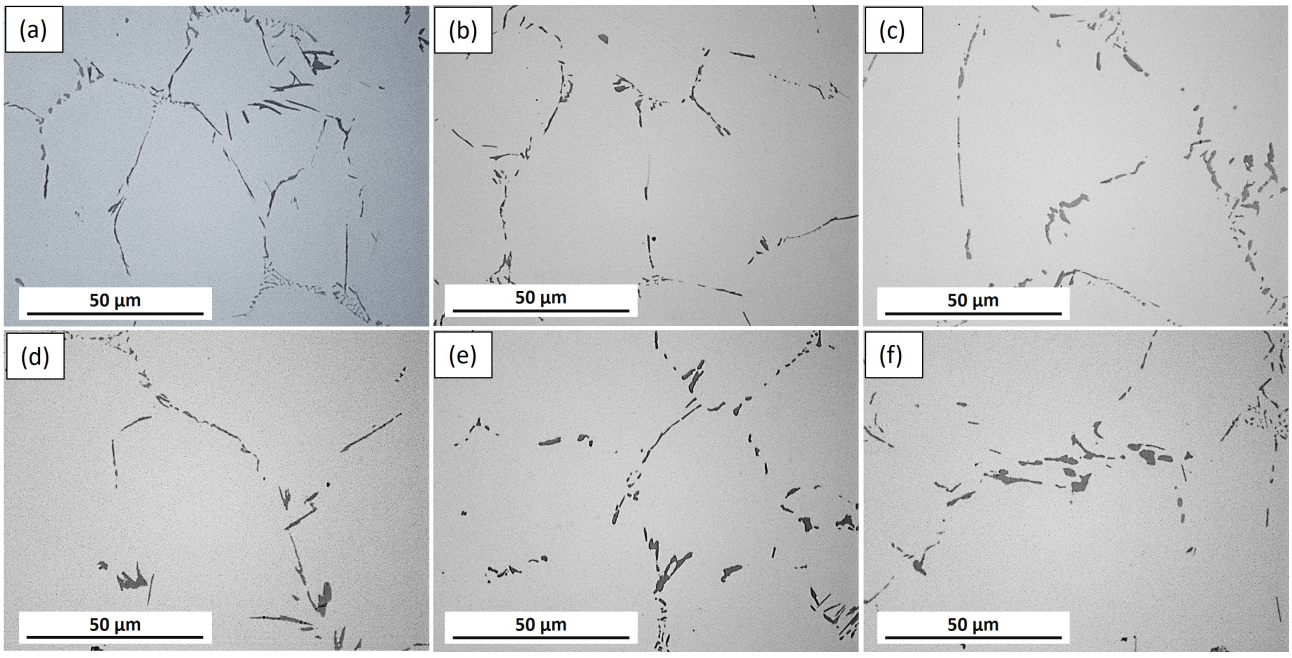

Figure 7.12: Optical micrographs showing the evolution of IMP in AA8079-EW from as-cast (a) through different homogenization treatments: (b) HT1, (c) HT, (d) HT3, (e) HT4, and (f) HT5.

.

Appendix C

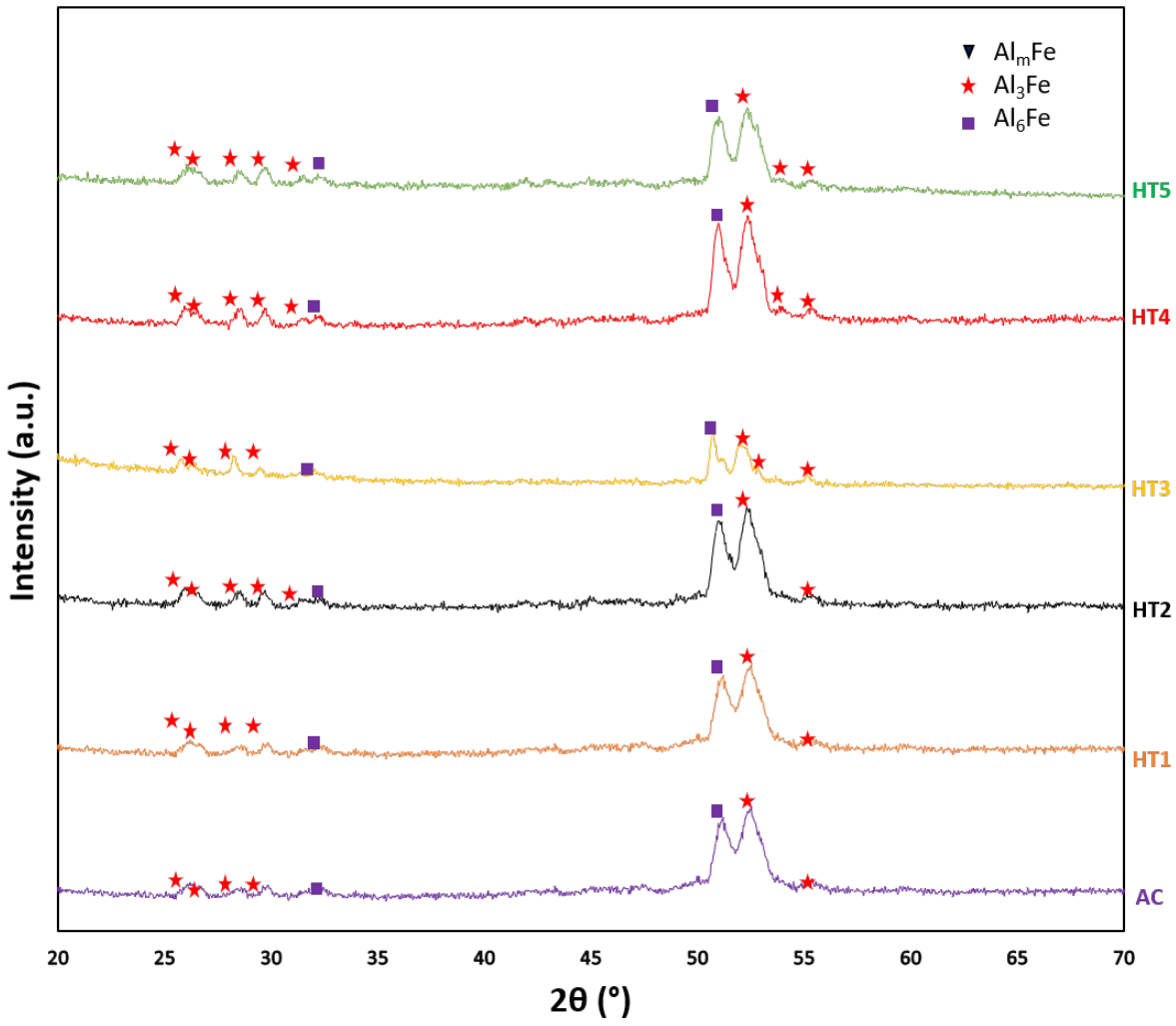

Figure 7.13: XRD Spectra of AA8021 centre Sample with Peak Assignments

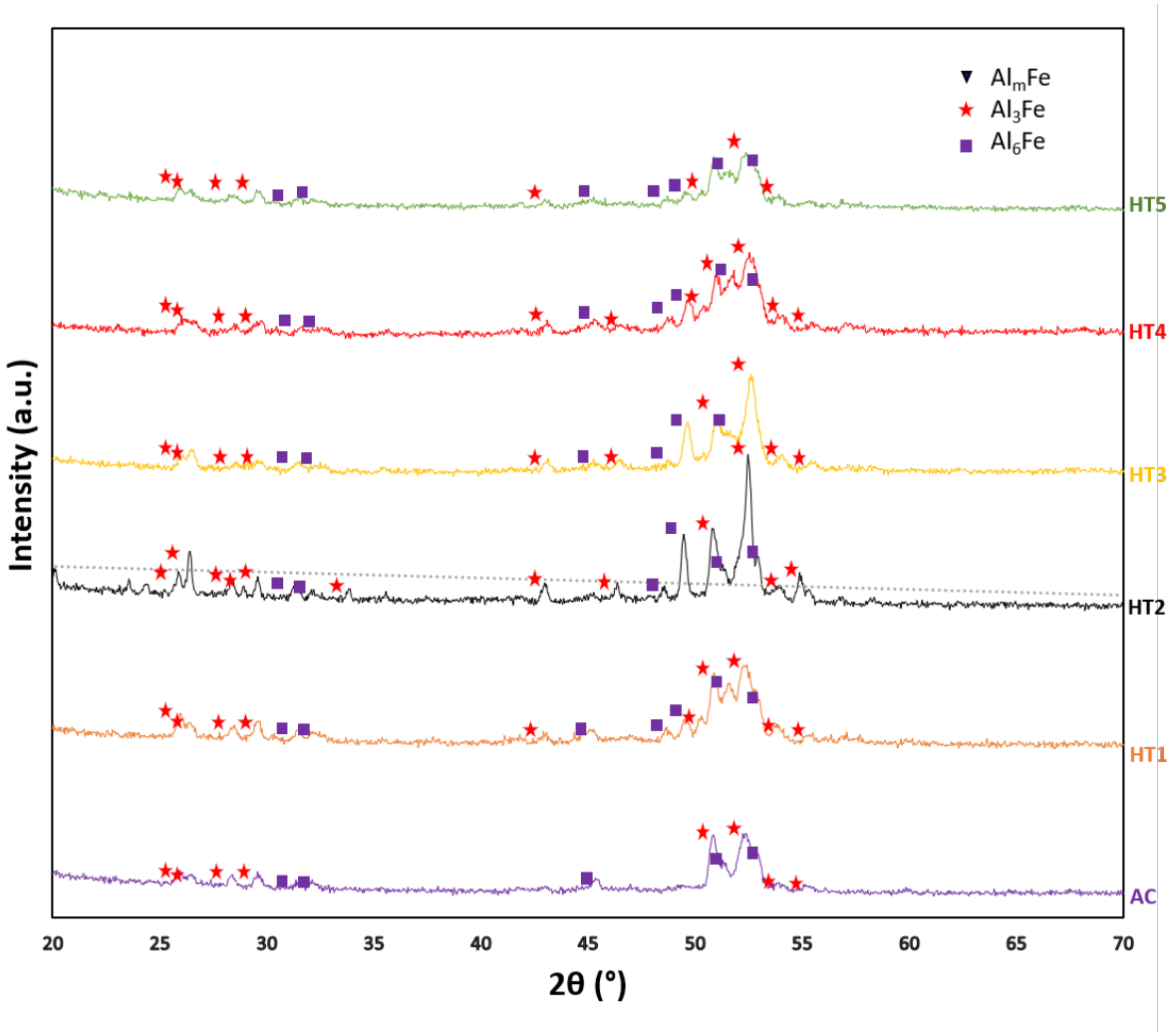

Figure 7.14: XRD Spectra of AA8079 Surface Sample with Peak Assignments

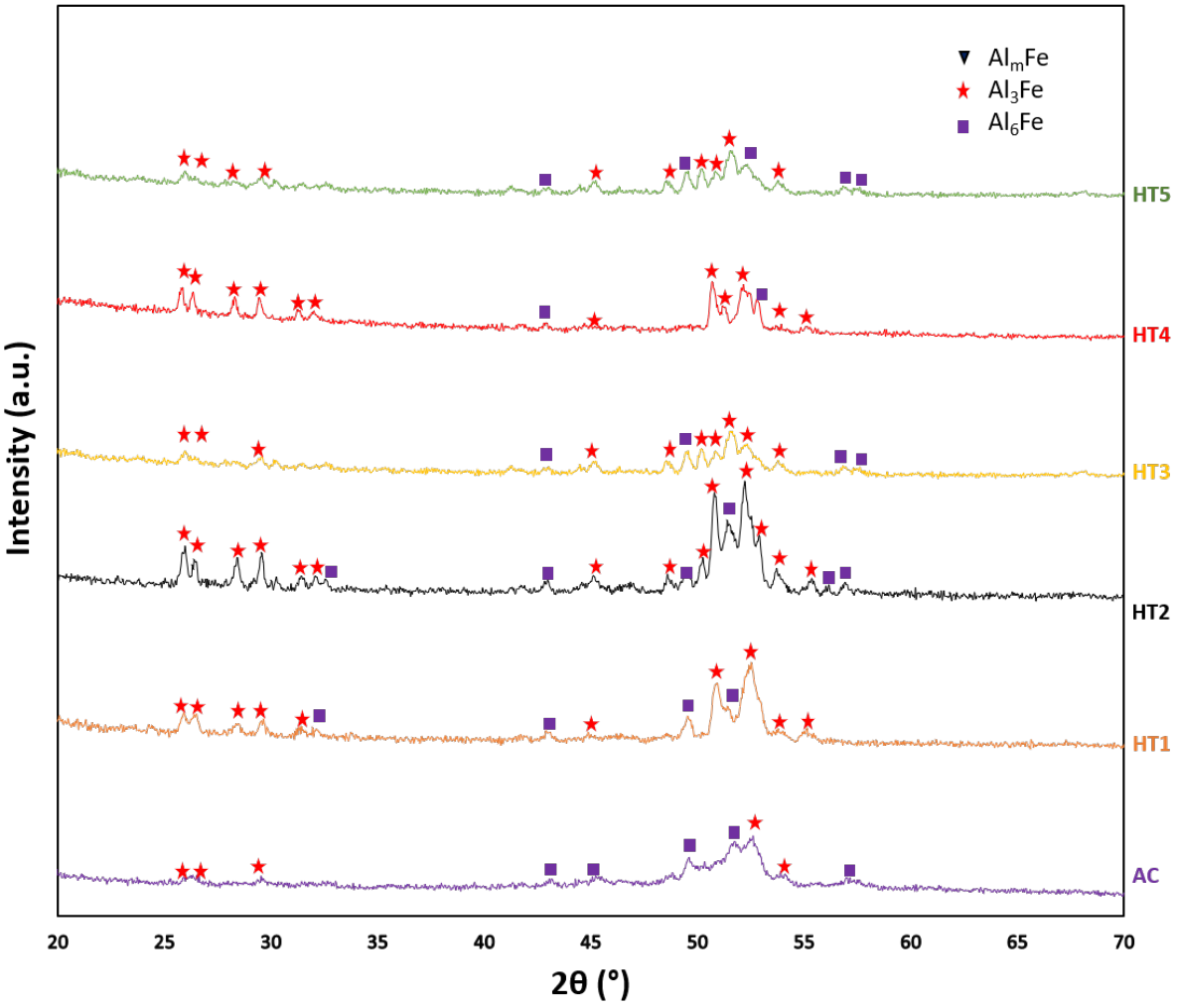

Figure 7.15: XRD Spectra of AA8079 centre Sample with Peak Assignments

Appendix D

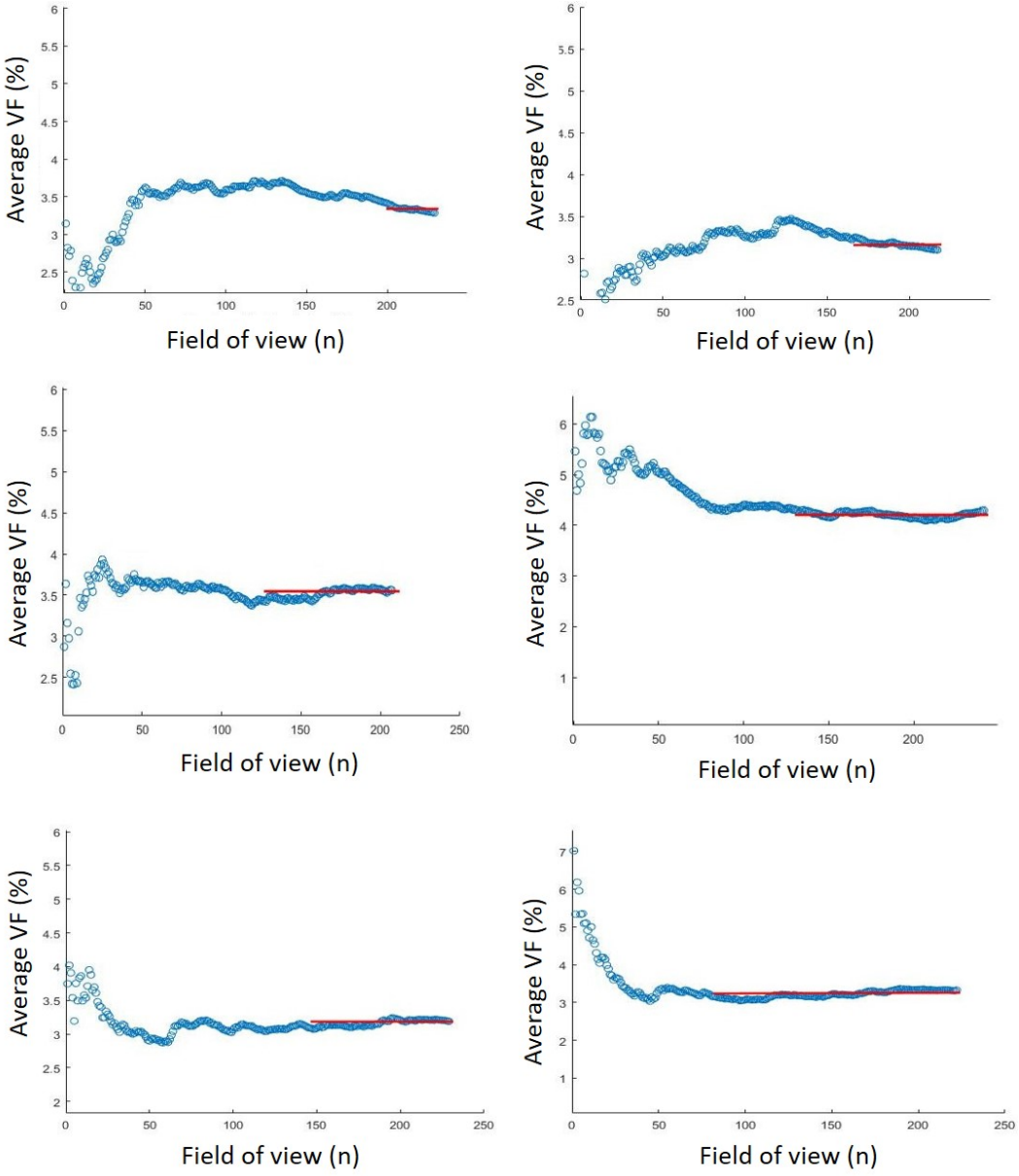

Figure 7.16: Minimum number of fields of view required to obtain a statistically meaningful volume fraction in AA8021 surface sample under different processing conditions

.

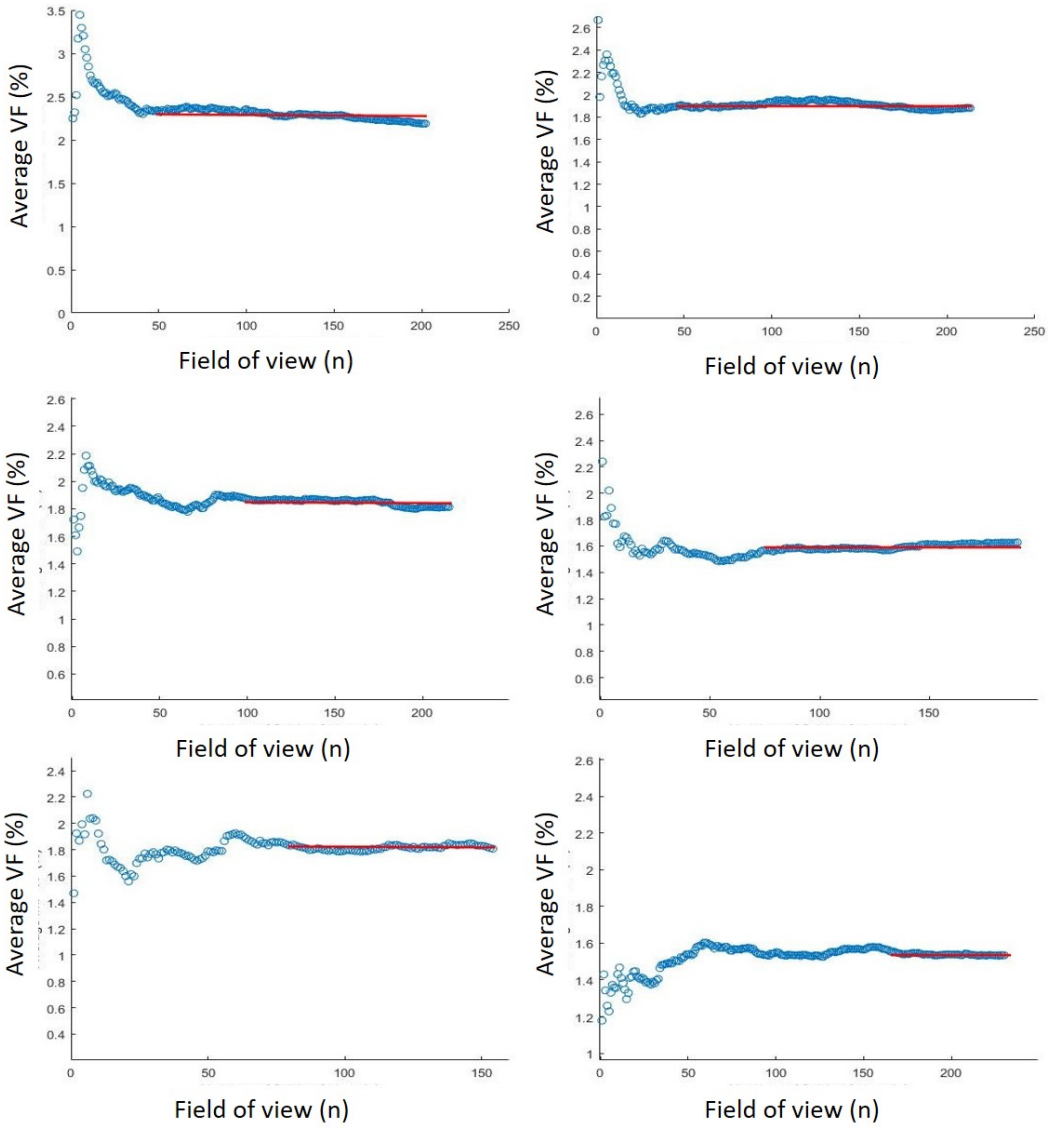

Figure 7.17: Minimum number of fields of view required to obtain a statistically meaningful volume fraction in AA8021 surface sample under different processing conditions

.

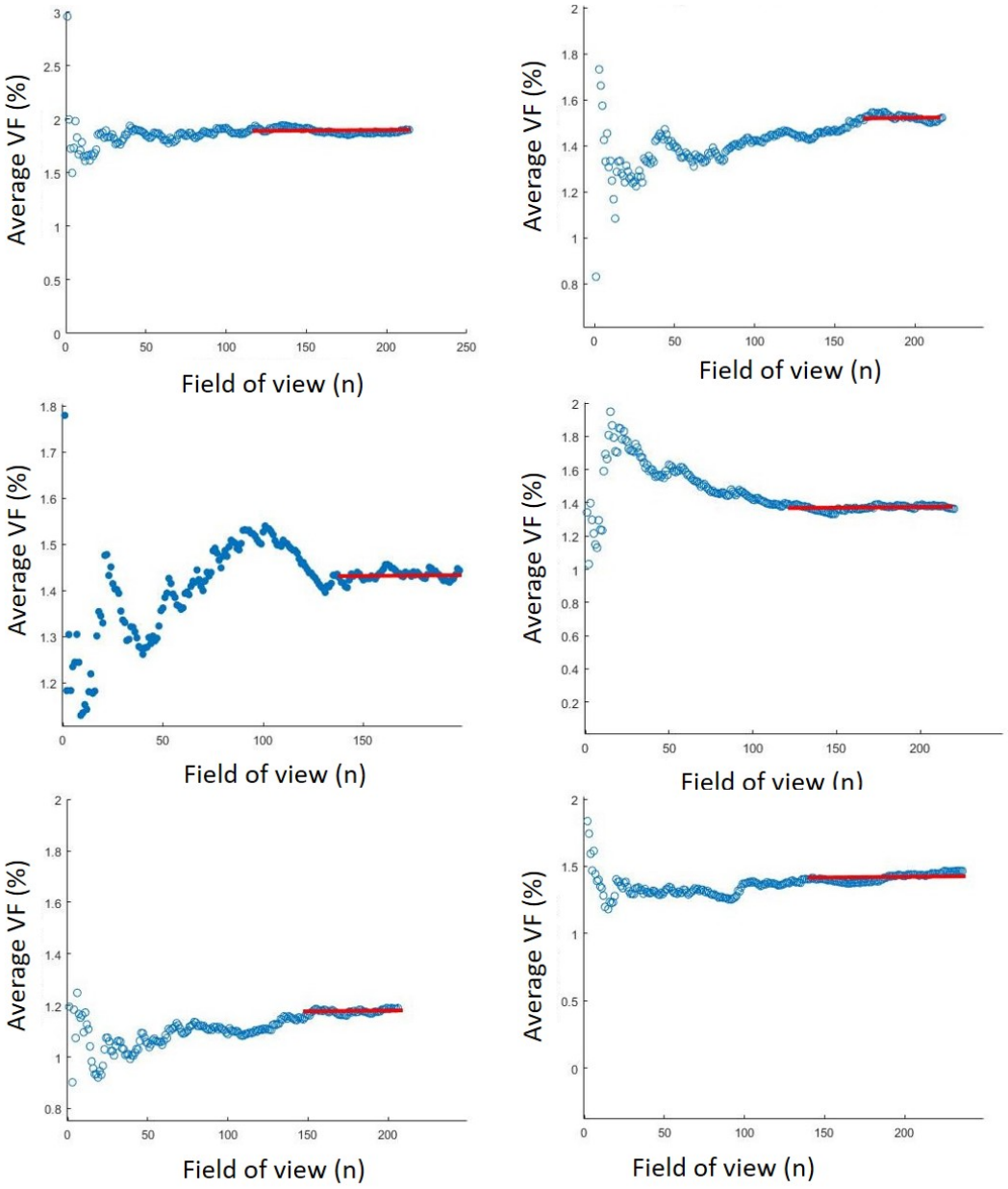

Figure 7.18: Minimum number of fields of view required to obtain a statistically meaningful volume fraction in AA8021 surface sample under different processing conditions

.

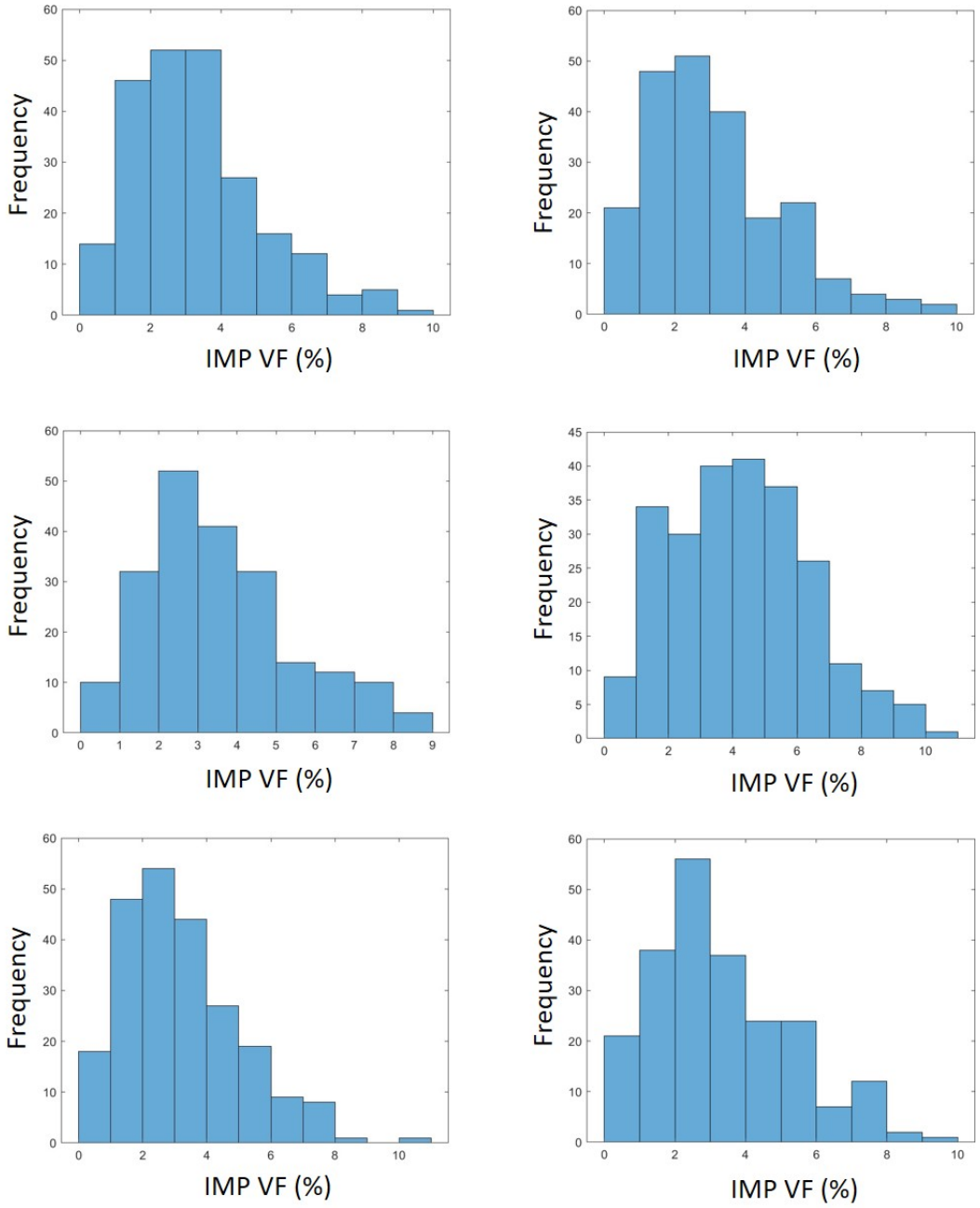

Figure 7.19: Distribution of volume fractions from approximately 200 fields of view in AA8021 surface under different processing conditions.

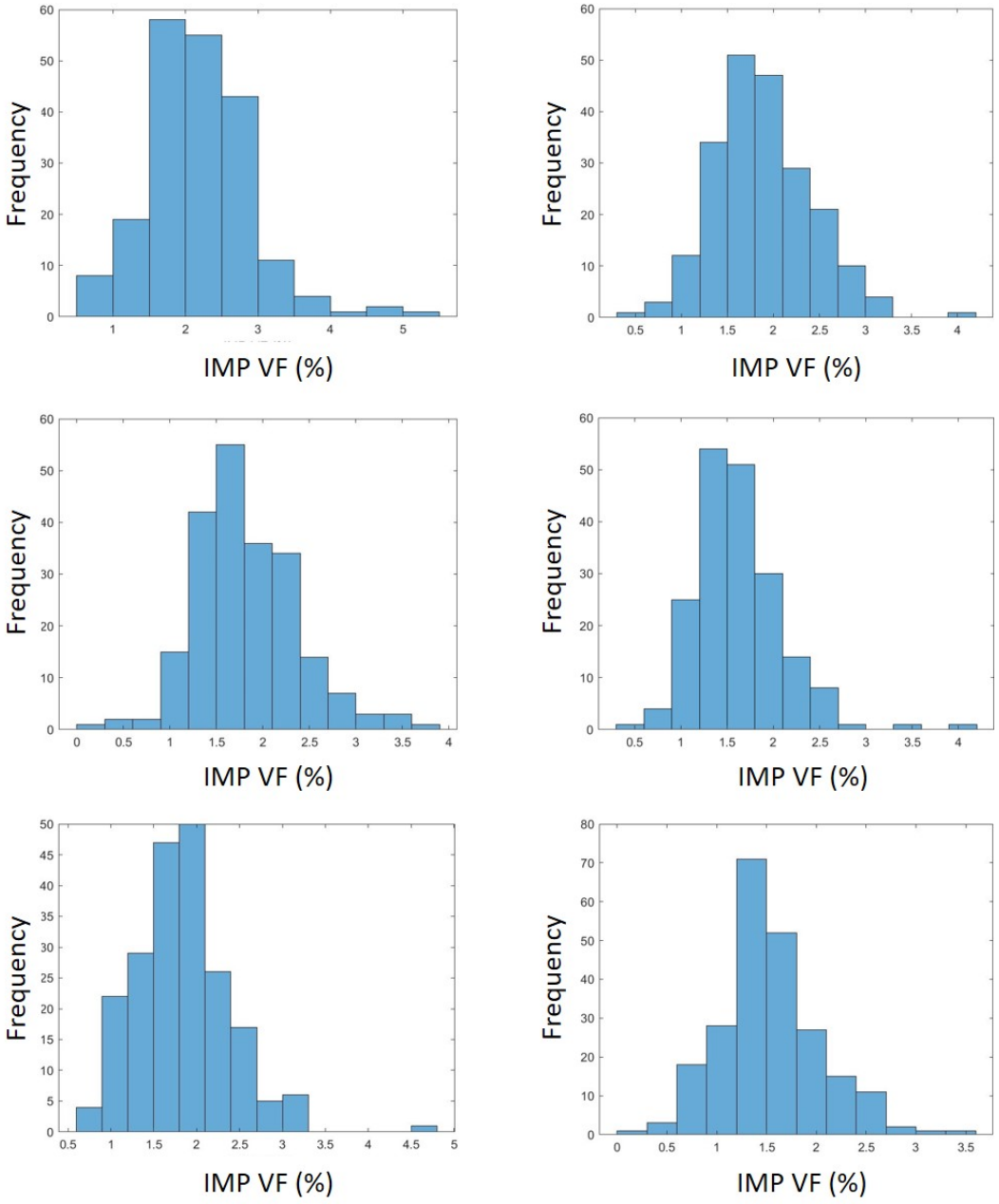

Figure 7.20: Distribution of volume fractions from approximately 200 fields of view in AA8021 surface under different processing conditions.

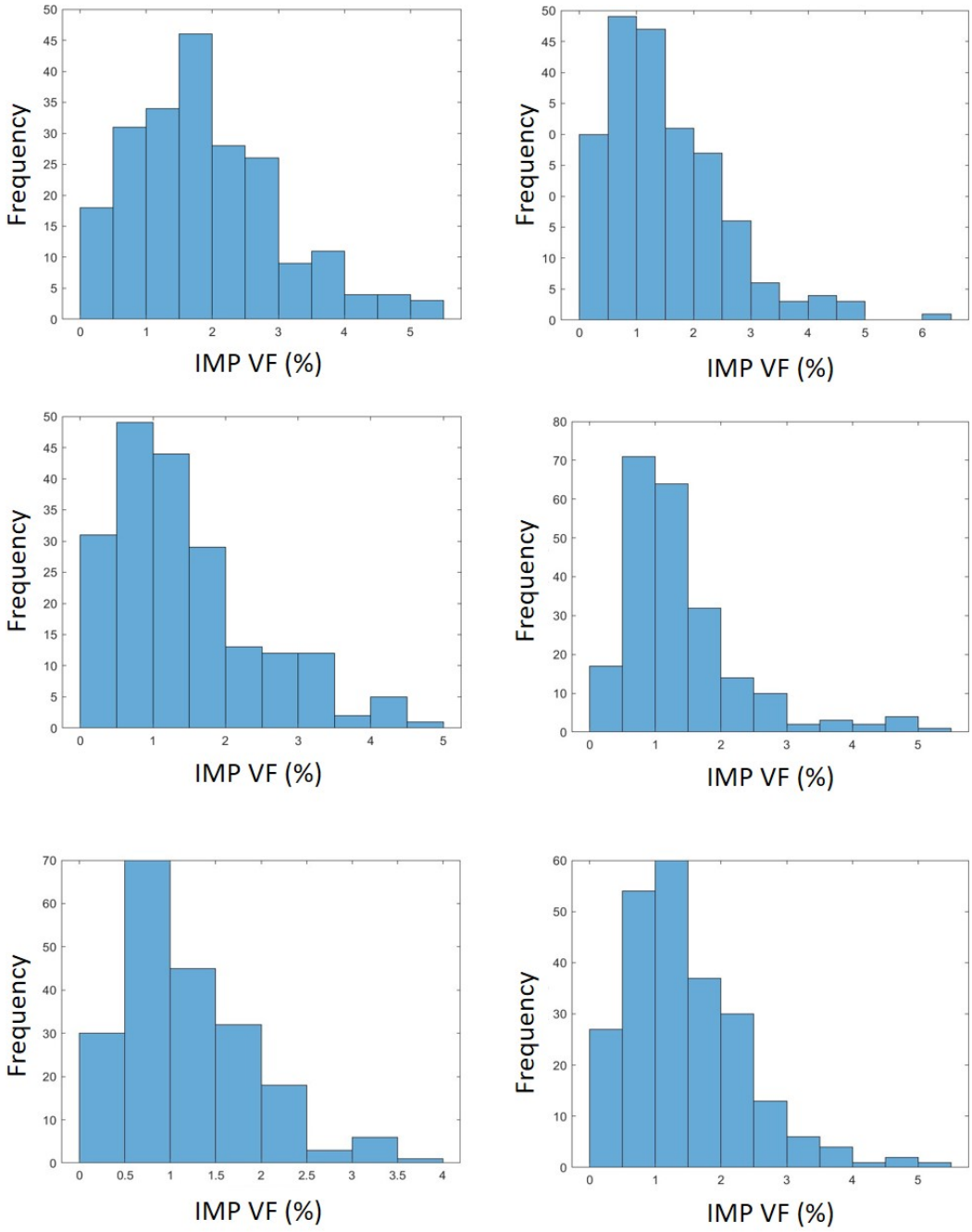

Figure 7.21: Distribution of volume fractions from approximately 200 fields of view in AA8021 surface under different processing conditions.

Appendix E

Table 7.1: Average volume fractions of IMPs in AA8021 ingot before and after homogenization treatments, with relative accuracy (RA) Values (95% Confidence Level)

Alloy	Region	condition	Fields of view (n)	Average IMP VF (%)	sd	95% CI (+/-)	%RA
AA8021	Surface	AC	200	4.81	1.65	0.23	4.76
		HT1	200	3.84	2.16	0.30	7.79
		HT2	200	4.21	2.11	0.29	6.94
		HT3	200	3.61	1.96	0.27	7.53
		HT4	200	3.83	2.13	0.30	7.71
		HT5	200	4.18	1.91	0.26	6.32
	Intermediate	AC	200	3.62	1.86	0.26	7.13
		HT1	200	4.15	1.91	0.26	6.38
		HT2	200	4.08	1.84	0.26	6.26
		HT3	200	3.62	2.08	0.29	7.94
		HT4	200	4.01	1.85	0.26	6.40
		HT5	200	3.83	2.01	0.28	7.27
	Centre	AC	200	3.41	1.30	0.18	5.29
		HT1	200	3.32	1.25	0.17	5.21
		HT2	200	3.64	0.86	0.12	3.26
		HT3	200	4.11	0.73	0.10	2.47
		HT4	200	3.69	1.14	0.16	4.28
		HT5	200	3.40	0.84	0.12	3.44

Table 7.2: Average volume fractions of IMPs in AA8079 ingot before and after homogenization treatments, with relative accuracy (RA) Values (95% Confidence Level).

Alloy	Region	condition	Fields of view (n)	Average IMP VF (%)	sd	95% CI (+/-)	%RA
AA8079	Surface	AC	200	2.30	1.19	0.16	7.17
		HT1	200	1.78	0.80	0.11	6.25
		HT2	200	1.76	0.81	0.11	6.34
		HT3	200	1.64	0.86	0.12	7.29
		HT4	200	1.89	0.98	0.14	7.21
		HT5	200	1.52	0.96	0.13	8.79
	Intermediate	AC	200	2.25	1.06	0.15	6.56
		HT1	200	1.86	1.10	0.15	8.22
		HT2	200	1.90	1.00	0.14	7.28
		HT3	200	1.79	0.94	0.13	7.29
		HT4	200	1.75	0.74	0.10	5.87
		HT5	200	1.59	0.88	0.12	7.71
	Centre	AC	200	1.85	0.53	0.07	4.01
		HT1	200	1.45	0.53	0.07	5.07
		HT2	200	1.40	0.57	0.08	5.68
		HT3	200	1.38	0.47	0.07	4.75
		HT4	200	1.19	0.71	0.10	8.28
		HT5	200	1.40	0.49	0.07	4.88

Table 7.3: Percentage relative accuracies of AA8021 samples in the as-cast and homogenized conditions, calculated at a 95% confidence interval

		Fields of view (n)			
	Condition	50	100	150	200
Surface	AC	15.43	13.46	8.47	4.76
	HT1	19.51	16.86	5.45	7.79
	HT2	15.53	13.59	9.02	6.94
	HT3	15.65	11.84	9.33	7.53
	HT4	18.11	15.73	10.92	7.71
	HT5	15.91	13.11	9.33	6.32
Centre	AC	16.01	10.5	8.64	5.29
	HT1	15.83	10.98	9.75	5.21
	HT2	15.26	9.79	8.41	3.26
	HT3	13.81	10.38	8.3	2.47
	HT4	16.32	11.11	8.73	4.28
	HT5	19.71	13.08	9.78	3.44

Table 7.4: Percentage relative accuracies of AA8079 samples in the as-cast and homogenized conditions, calculated at a 95% confidence interval

		Fields of view (n)			
	Condition	50	100	150	200
Surface	AC	11.45	8.39	7.73	7.17
	HT1	16.68	14.65	9.44	6.25
	HT2	16.99	16.3	10.79	6.34
	HT3	18.76	15.81	12.73	7.29
	HT4	18.9	16.25	10.2	7.21
	HT5	19.46	16.6	11.15	8.79
Centre	AC	14.5	11.47	9.26	4.01
	HT1	14.29	9	6.68	5.07
	HT2	14.47	10.8	8.48	5.68
	HT3	13.16	10.5	9.2	4.75
	HT4	16.38	11.41	8.67	8.28
	HT5	16.51	12.56	10.21	4.88